DEVELOPMENT AND CHARACTERIZATION OF BIOPOLYMER/BIOCERAMIC COMPOSITE MATERIALS FOR BONE IMPLANT APPLICATIONS

ジョン, ジェームズ, ダックワース

DEVELOPMENT AND CHARACTERIZATION OF BIOPOLYMER/ BIOCERAMIC COMPOSITE MATERIALS FOR BONE IMPLANT APPLICATIONS

PhD Thesis

Submitted as partial fulfillment of the requirements for the degree

Doctorate of Philosophy

by

JOHN JAMES DUCKWORTH

3ES17117N

Department of Molecular and Material Sciences

Interdisciplinary Graduate School of Engineering Sciences

Kyushu University

Japan

2020

ACKNOWLEDGEMENTS

After three years of effort, it is a great relief to finally complete this dissertation, though the time spent studying and researching for it has been an immensely enjoyable challenge. My most sincere gratitude must go to Associate Professor Dr. Mitsugu Todo, for allowing me to join his excellent lab and work on fascinating projects for the past five years. The knowledge and skills he has helped me develop through his guidance are invaluable, and I will never forget his endless patience and support. My thanks also go to Assistant Professor Dr. Takaaki Arahira of Fukuoka Dental College and Professor Dr. Ryan Roeder of the University of Notre Dame, for allowing me to work with them in their laboratories and being so free and open with their time and knowledge.

I would also like to thank the senior students of my laboratory for taking care of me when I first arrived in Japan, and answering my endless questions; Dr. Yusuke Nakamuta, Dr. Azizah Intan Pangesty and all the others. My thanks also go to the current lab members, who continue to do fantastic work and will go from success to success in the future; Mr. Wu Shun, Mr. Hishyam, Mr. Bou and everyone else.

Without the Advanced Graduate Program in Global Strategy for Green Asia, I would never have been able to come to Japan and begin this research, and my life here. The GA staff work tirelessly to help all us students, so an enormous thank you to Ms. Hayashi, Ms. Kano and all the others.

I must mention also the staff and student members of the Kyushu University IGSES International Students Association, who have played an enormous role in my life

since arriving in Japan. Without their support and friendship, this dissertation may never have been complete. Thank you to Associate Professor Dr. Dong Wang, Ms. Kojima, Ms. Murga, Ms. Bannaron and everyone else who freely gave their time and energy for me.

Finally, a special thank you to my family far away, who have visited, called, sent gifts and generally supported me beyond anything I could have hoped for. And also to my family close by, Ms. Hongjoo Park, who made Fukuoka a home for me these last 5 years.

ABSTRACT

Biomaterials have been investigated in recent years with regards to many kinds of implant surgeries. Especially on surgeries involving bone repair, traditional materials such as stainless steel, titanium and polyethylene have proven extremely useful, and have served remarkably well over the last century. However, these materials do have many shortcomings, such as low bioactivity, poor osseointegration, internal loosing and displacement, stress shielding, and no bioresorbability. There are many reasons to believe that biomaterials, specifically composites of biopolymers and bioceramics, are well suited to overcome these limitations. These problems and the biomaterials which show promise for overcoming them are fully explained in Chapter 1.

In Chapter 2, a series of biomaterial composites were successfully fabricated using calcium phosphate microbeads and three kinds of biopolymer as the matrix; PLLA, PCL and a 50:50 blend of the two. The methods for fabricating calcium phosphate beads were optimized and the beads characterized using XRD and SEM imaging. Investigations into the material properties of the novel biomaterials showed that microbead inclusion caused a slight increase in stiffness for PLLA and PCL, but instead a sharp decrease in stiffness for the blend. Fracture toughness as measured by K_{IC} and G_{in} slightly decreased for the PLLA and blended polymer with microbead inclusion, however for PCL the value of K_{IC} barely changed at all.

The mechanism of fracture for each material was also investigated, revealing that each biocomposite fractured under different conditions. Once microbeads were added, PLLA fractured by a two phase mechanism caused by intrusion of the polymer into the

microbead. In PCL and the blended polymer, microbeads pulled out during fracture as the polymer did not intrude upon them, and both showed ductile fracture characteristics. The reduced fracture toughness of the blended polymer was hypothesized to be caused by the distinct boundary layer which was seen to form at the bead interface in only this material. This layer was absent from the bead interfaces with PCL. This system was also investigated using FE analysis to help establish the fracture mechanism, and fracture locations and SED supported the theory. Overall, this research shows that inclusion of microbeads into biopolymers is a promising avenue for research. By understanding the difference in mechanisms of fracture caused in different materials, we can understand which might be used to improve in the future.

In Chapter 3, a different application of biopolymer/bioceramic composites was investigated. PLCL fibres of four different average lengths were produced, and successfully incorporated into a dicalcium phosphate dihydrate matrix to be investigated as a potential novel biomaterial for kyphoplasty surgery. Fibres were characterized by length using SEM imaging, and the effect of fibre length on compressive strength and compressive elastic modulus of the biocomposite was investigated. . It was shown that by including PLCL fibres of average length 400μm into the bioceramic, the compressive strength of the material doubled. The fibres also had the effect of reducing the compressive elastic modulus drastically, making the material as flexible as cancellous bone. This is another excellent result, as the high stiffness of materials used for kyphoplasty has previously been blamed for many complications after surgery. Secondarily, the packing of the fibres within the material was investigated. A parameter, ρ, was established to represent fibre packing within the material. Micro-CT scans and FE

modelling were used to successfully correlate ρ with fibre length, and suggest a mechanism for why the compressive elastic modulus of the composite material dropped so significantly.

TABLE OF CONTENTS

LIST OF TABLES

LIST OF FIGURES

CHAPTER 1: INTRODUCTION

1.1 Applications of bone implants

1.1.1 Bone plates, screws and rods

Implants which hold together broken bones during natural healing are the oldest and most widely used type of bone implant in the world. Once internal surgery under anaesthetic became routine practice in the first half of the 20th century, it was natural for surgeons to attempt to replace long-established external braces and supports with internal braces and supports, when dealing with broken bones [1]. The advantages of supporting healing bone with internally implanted braces are many. Bones can be held together far more closely and firmly with internal rods, plates and screws, allowing for faster recovery from injury and fewer complications from misalignment and movement during healing. Small plates and screws have also long been the key to carefully repairing comminuted fractures; where many pieces of shattered bone need to be fixed back together securely to retain full use of the body part in question, and to prevent disfiguration [2, 3].

Typically, implants of this kind are either removed by secondary surgery after the bone has fully healed, or left in the patient indefinitely if further surgery is determined to be too risky. Often the decision to leave the implant inside the patient is arrived at with elderly patients, as any kind of anaesthetic surgery can be dangerous for people with pre-existing conditions and slower rates of healing [4, 5]. This is not ideal of course, as over time implants can slip and dislocate from their intended place, can cause inflammatory or

immunological responses, can be the starting points for secondary infections, and can also be a nuisance for the patient when travelling. It is desirable then, for a material to be used which will be strong and flexible during use, bond well with bone to prevent dislocation, have no immunological response, and be absorbed into the body naturally after use.

1.1.2 Kyphoplasty

Vertebral compression fractures are very common in patients suffering from osteoporosis and occur when the central mass of bone in a vertebra gives way due to an external force and internal weakening. In 2011 for example, around 700,000 vertebral compression fractures were diagnosed in the United States alone [6]. Around 50% of bone fractures that occur in osteoporotic patients are vertebral fractures like these, and the overall risk of contracting a vertebral compression fracture for anyone over the age of 65 is 27% in the U.S.A [7, 8]. Vertebral compression fractures are themselves painful, deforming and often debilitating, but also have been linked co-morbidly to many other diseases by way of causing psychiatric problems, sleep disorders, reduced mobility and pulmonary complications [9, 10].

For a long time, the only treatments for vertebral compression fractures available to clinicians were courses of bed rest, back braces, and pain medication [11]. These methods continue to be the recommended treatments for all but the most severe cases of vertebral compression fracture in most countries. However, in some cases clinicians will recommend kyphoplasty as a more proactive treatment. Kyphoplasty is a relatively modern type of minimally invasive surgery used to treat vertebral compression fractures.

The outline of a modern balloon kyphoplasty surgery is shown in Figure 1.1, and the radiographs from a real life successful surgery are shown in Figure 1.2. A balloon tamp is inserted percutaneously into the compressed vertebra and expanded to reform the shape and alignment of the spine [12]. It is then deflated and removed, and the resulting cavity is filled with a viscous bone cement, usually poly(methyl methacrylate) (PMMA). This procedure somewhat restores the height, strength and shape of the vertebra, reducing pain for the patient as well as improving the quality of life [13, 14]. The surgery can be completed in under an hour under local anesthetic, and patients are usually able to leave the hospital the same day or the next day, making it a very quick and affordable treatment. This simplicity along with its reported benefits has meant the number of kyphoplasty procedures undertaken each year has grown rapidly. Since the first surgery in 1998, the rate of kyphoplasty procedures increased to over 25,000 procedures per year in the United States in 2003, and to around 70,000 per year in 2011 [15].

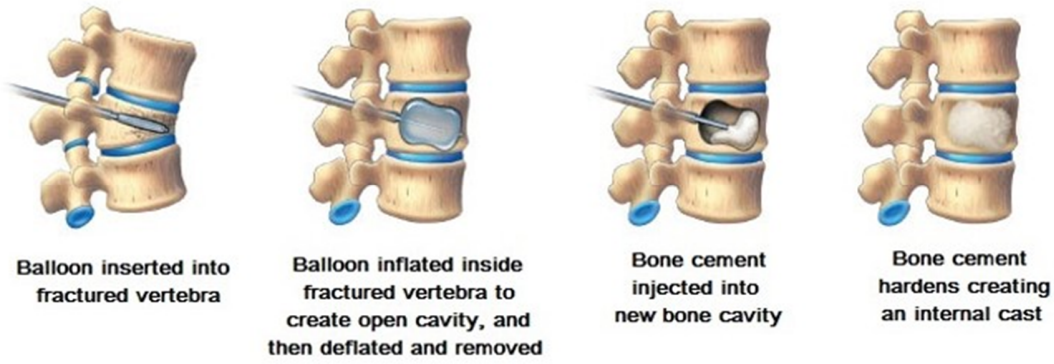

Figure 1.1 Diagram of a balloon kyphoplasty procedure on a vertebra which has undergone a compression fracture.

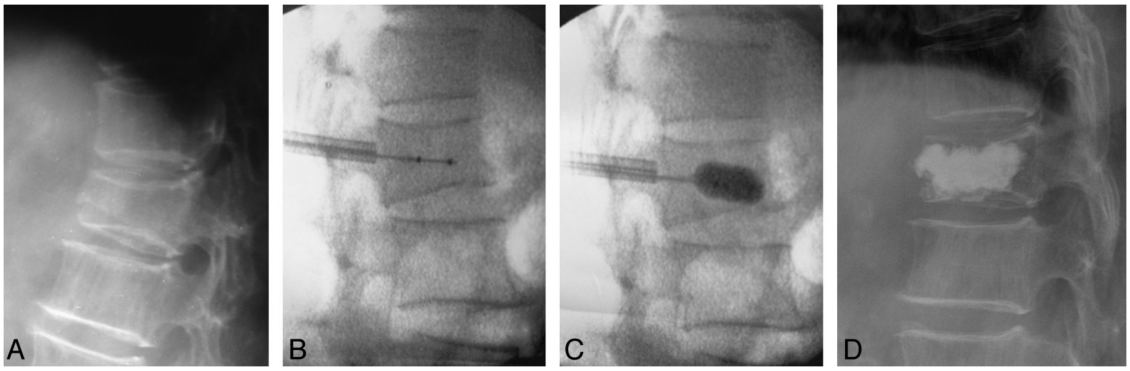

Figure 1.2 Stages of performing a kyphoplasty surgery to treat a vertebral compression fracture, from literature. A) a vertebral compression fracture, B) percutaneous insertion of a needle, C) inflation of a balloon tamp, D) removal of tamp and injection of filler [14].

Many studies have shown the efficacy of this treatment; however it is not without its drawbacks. It has been shown that the kyphoplasty treatment can cause a three to five times increase in the number of secondary fractures occurring in osteoporotic patients; that is, fractures occurring elsewhere in the spine after the surgery [16]. Factors considered highly likely to explain this phenomenon are bone cement leakage into the intervertebral disc, loss in bone density around the implant, and a lack of systematic orthopaedic treatment post-surgery, though it is believed the mechanical properties of the implant may also play a role [17, 18]. Studies have suggested that different cements affect the overall performance of the kyphoplasty procedure dramatically, specifically that the stiffness (Young's Modulus) of the material may be inversely proportional to secondary fracture rate [19, 20].

1.2 Organic and inorganic biomaterials

1.2.1 Overview

Biopolymers are widely used in all kinds of surgeries, and even in applications outside of the medical field. They are environmentally renewable, physically moldable, and their shapes are customizable at low temperatures. They are extremely versatile in their chemical and physical properties, meaning stiff, hard, flexible or soft materials can all be fabricated and implanted. Importantly, they can be made to degrade within the body at precisely controlled rates, allowing naturally healed tissue to slowly replace the artificial implant. Their surface properties can also be controlled in order to promote or deter integration into the host tissue over time [21].

Biopolymers of interest in orthopaedics are synthetic biopolymers based on naturally occurring monomers, specifically caprolactides and lactides. These materials can hydrolyze in the body to degrade over time if desired, unlike most oil-based polymers. When these materials do hydrolyze in the body, they form secondary products that are easy for the body to process and dispose of, again unlike most oil-based polymers [22]. Co-polymers formed from combinations of monomers, such as poly(*L*-lactic-co-ε-caprolactone) (PLCL) are also commonly used to give greater control over the glass transition temperature, stiffness, hardness and durability of a given material [23, 24]. On top of this variability, the chain lengths, crystallinity and branching of these polymers can be controlled too if desired, making this class of polymers extremely diverse and applicable in many areas.

Table 1.1 shows the physical properties of the three most commonly used biopolymers for implants, PLLA, PLCL (50:50) and PCL. All these three materials will be used in this study. Note that even the physical properties of these linear homopolymers have to be given as ranges, to account for variation due to average molecular weight, chain length distribution and crystallinity.

Table 1.1 Basic chemical properties of three biopolymers used in orthopaedics [25-32]

Abbr.	**Chemical Name**	**T_g / °C** [25]	**T_m / °C** [25]	**Tensile Strength /MPa** [26,27,29]	**Tensile Modulus /GPa** [26,28,29]
PLLA	poly(L-lactic acid)	60-65	173-178	390-2300	0.5-16
PLCL	poly(L-lactic acid -co-caprolactone) (50:50)	16-35	130-160	3-20	~0.05
PCL	poly(ε-caprolactone)	~ -60	60-65	10-17	0.01-1.2

Many biopolymer implants made from these materials, specifically of PLLA, currently exist on the market, and have been used successfully in non-load bearing situations before, often in maxillofacial and dental applications. Figures 1.3a and b show a selection of those available devices, and in Figure 1.3c the implantation of such a device *in vivo* as part of a maxillofacial surgery can be seen. The implanted PLLA bone plate can be seen to be bending, one of the many advantages of using such biopolymer materials in this context.

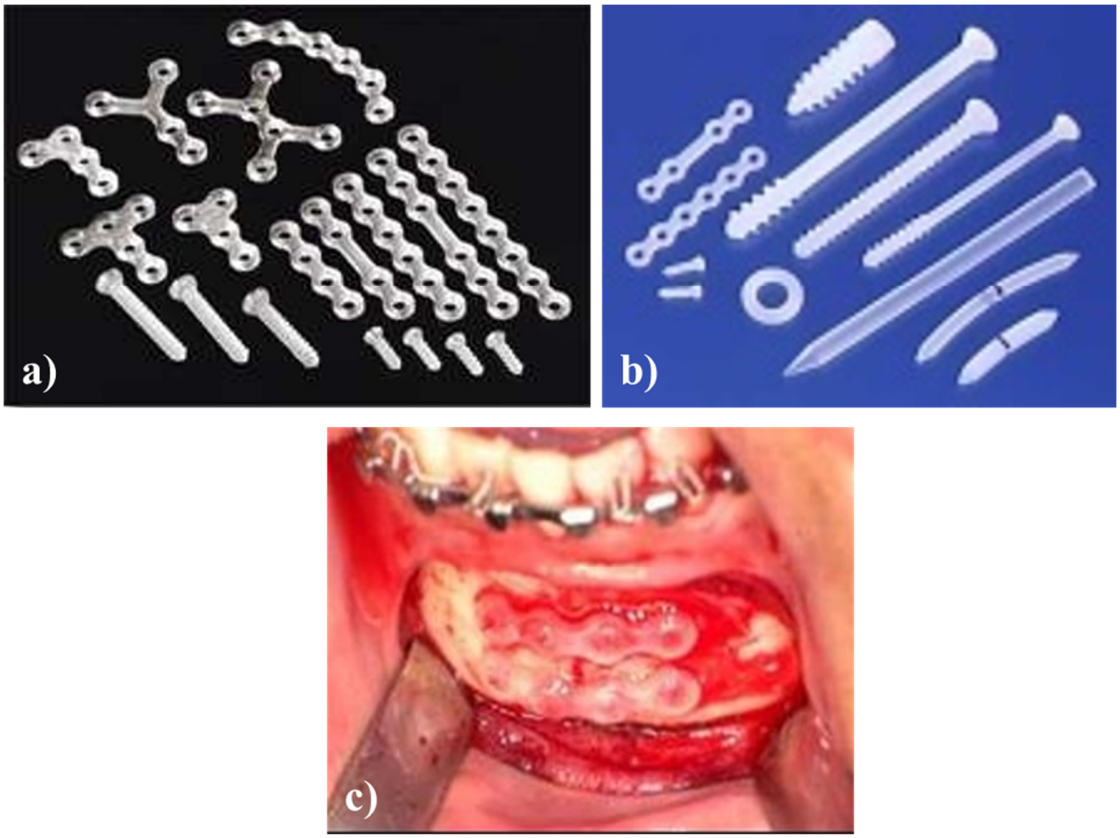

Figure 1.3 a), b) Existing PLLA bone plates and fixation devices and c) an *in vivo* example of a PLLA bone plate in use during maxillofacial surgery.

1.2.2 Calcium phosphate ceramics

Calcium phosphate based ceramics are of particular interest in the field of orthopaedics for several reasons. They can provide greater hardness and stiffness than polymers, which is useful in certain applications, and they can be used when greater load-bearing capabilities are required [33]. Chemically, calcium phosphate based ceramics are very similar in composition to the naturally occurring inorganic components of bone and therefore are much more easily integrated into existing tissue; in other words they are

good at osseointegration [34-36]. Hydroxyapatite, with the chemical formula $Ca_5(PO_4)_3(OH)$, is the most commonly used calcium phosphate based cement [37, 38]. It has a compressive strength similar to that of natural bone, and can easily be integrated into the surrounding bone tissue.

A second calcium phosphate based ceramic that has received attention as a biomaterial is dicalcium phosphate dihydrate, chemical formula $CaHPO_4 \cdot 2H_2O$ [39]. This material is formed itself from two calcium phosphate precursors, tricalcium phosphate, chemical formula $Ca_3(PO_4)_2$, and monocalcium phosphate monohydrate, chemical formula $Ca(H_2PO_4)_2 \cdot H_2O$, via the reaction shown in Equation 1.1. Dicalcium phosphate dihydrate is a promising material for use as a bioresorbable, injectable bone cement in a wide range of orthopedic surgeries, as an anhydrous mix of these precursor reactants in glycerol can be stored indefinitely in liquid form, then solidify into ceramic when exposed to aqueous, physiological conditions, as upon injection [40]. Whilst bone-like in mineral content, the mechanical properties of DCPD cements have yet to be made rugged enough to allow for loadbearing medical application. DCPD has a compressive strength of 10-20 MPa depending on powder/ liquid ratios and other environmental effects [41, 42]. This is at the low end of known cancellous bone strengths and far below cortical bone strengths [43, 44]. Importantly, the compressive elastic modulus of DCPD cement, at around 1-10 GPa, is far higher than that of either cortical or cancellous bone at around 100 MPa and 50 MPa respectively [41, 45].

$$Ca_3(PO_4)_2 + Ca(H_2PO_4)_2 \cdot H_2O + 7H_2O \rightarrow 4CaHPO_4 \cdot 2H_2O \qquad 1.1$$

Tricalcium phosphate comes in two stable crystalline forms, α and β. Both are available commercially and are used in a wide range of orthopaedic and dental applications, with the α-form being more readily soluble in aqueous solution, and therefore much more easily degraded in the body [46, 47]. For the formation of dicalcium phosphate dihydrate, β-TCP is most commonly used [48].

Under high temperatures, β-TCP also reaches a thermal equilibrium in which it forms hydroxyapatite under the following conditions [49].

$$10Ca_3(PO_4)_2 + 6H_2O \leftrightarrow 3Ca_{10}(PO_4)_6(OH)_2 + 2H_3PO_4 \qquad 1.2$$

If fired under atmospheric conditions, it is possible to convert large portions of the β-TCP crystal in an object to hydroxyapatite, as the phosphoric acid byproduct is evaporated away driving the equilibrium toward the right.

Table 1.2 below summarizes the material and biological properties of the various calcium phosphates which will be used in this study, as well as the equivalent material properties of human bone for comparison. When designing and testing composites later in this study, the values given below for cancellous and cortical bone will be vital, as these will be the criteria for success; we will try to create a composite which can match or exceed the compressive strength of bone, or match the elastic modulus, *E*.

Table 1.2 Material properties of calcium phosphate ceramics and bone [41, 50-56].

Material	**Composition**	**Compressive strength/ MPa**	***E* / GPa**	**Solubility / mg L^{-1}**
Hydroxyapatite	$Ca_5(PO_4)_3(OH)$	75[41]	13[41]	6.6[53]
α-tricalcium phosphate	$Ca_3(PO_4)_2$	20-150[50]	0.3-0.5[50]	200[54]
β-tricalcium phosphate	$Ca_3(PO_4)_2$	20-150[50]	0.3-0.5[50]	8.0[54]
Monocalcium phosphate monohydrate	$Ca(H_2PO_4)_2•H_2O$	-	-	93,900[55]
Dicalcium phosphate dihydrate	$CaHPO_4•2H_2O$	10[41]	1-10[41]	153[56]
Cortical bone	-	130-200[51]	11-17[51]	-
Cancellous bone	-	1-16[52]	0.1-1[52]	-

1.2.3 Poly(L-lactic acid)

The biomaterial poly(*L*-lactic acid) is a polyester most commonly formed in one of two reactions; from the direct polycondensation of lactic acid, or through the ring-opening polymerization of lactide. Both of these monomers are easily obtainable in industrial quantities from common feedstocks such as corn starch, rice, potatoes and other cereal crops [57, 58]. As these are both condensation reactions, hydrolysis of these bonds to reform the biomolecule monomers happens naturally *in vivo*. The two reactions to form poly(*L*-lactic acid) are shown in Figure 1.4. Note the stereochemistry on the methyl group present in PLA. Biological synthesis of lactic acid usually generates the *L* enantiomer, and so this is used in industry. Whilst this is the most common form present in the human body, the *D* enantiomer is not toxic.

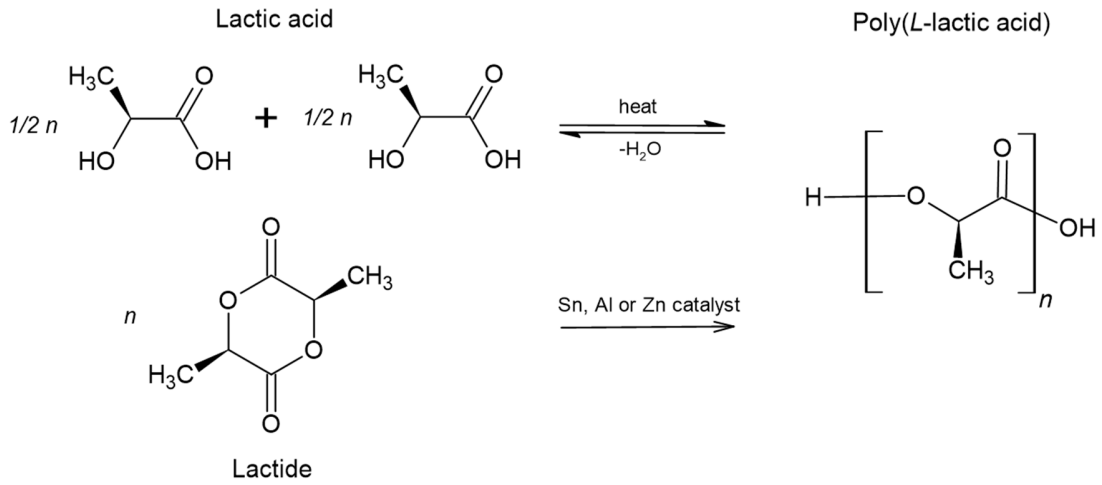

Figure 1.4 The two industrial chemical pathways for forming poly(*L*-lactic acid).

PLLA has been used for many years as a bone fixation device in orthopaedic, maxillofacial and oral surgeries, due to its relative strength, biocompatibility and bioabsorbability [59-61]. Very recently, PLLA has also been shown to be a suitable medium for the incorporation of hydrophobic drugs in order to increase the chance of osseointegration and reduce the chance of bacterial infections [62-64]. However, though the material is widely used in bone implant surgeries worldwide, there are many cases of devices becoming dislocated, fracturing, or in other ways becoming separated in whole or in part from their intended locations, proving that an adaption from the blank PLLA is necessary [65-67].

1.2.4 Poly(ε-caprolactone)

Poly(ε-caprolactone) is also a polyester, formed via the ring opening polymerization of a ε-caprolactone monomer. The reaction can be catalysed either by an organometallic catalyst such as tin (II) 2-ethylhexanoate, an enzyme such as lipase, or an organic molecule such as a cyclopentadienide ion, as shown in Figure 1.5.

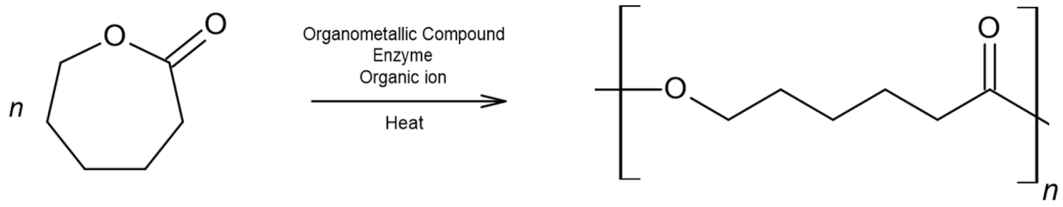

Figure 1.5 Viable chemical pathways for forming poly (ε-caprolactone).

The most common medical application for PCL currently is in the form of bioresorbable sutures used to close wounds and surgical incisions. The most widely distributed PCL suture of this type is manufactured by Medtronic Plc under various brand names [68]. PCL is effective as a suturing material firstly because by altering fibre thickness and molecular weight, it is possible to vary the time taken for bioresorption, and secondly because it is extremely flexible for its relative strength.

PCL has also been studied as a coating for more conventional materials, in the hopes of gaining some of the advantageous biological properties without sacrificing material strength [69, 70]. It was seen that these materials did indeed have improved biological activity, however due to the biodegradable nature of PCL these effects of a thin coating were short lived.

Better results were seen by creating fibre mats of PCL from electrospun or melt-spun fibres. Gomes et al. showed that PCL fibre mats produced by electrospinning were highly effective both *in vitro* and *in vivo* as a cell scaffold in the skin, showing especially that such PCL mats were very effective at allowing cell migration through the porous material [71]. A study by Pangesty et al. showed the same excellent cell migration behaviour from PCL fibre mats when applied to vascular engineering [72]. However, for the purposes of bone plates, it is considered a better option to use PCL as in a solid, bulk form. Due to its low strength, few studies have actually been performed using bulk PCL as a bone plate material, aside from studies in smaller animals where generally loads are less strong [73]. Most modern research focuses on using PCL as a component in composite materials.

1.2.5 Existing biopolymer and calcium phosphate ceramic composites

Many improvements to the osseointegrating ability of biopolymers have been made in recent years by the inclusion of calcium phosphates. Lin et al showed that the inclusion of the calcium phosphate hydroxyapatite (HA) powder as filler in PLLA increased its bending and compressive strengths, and that cell proliferation on the material increased [74]. HA powder has seen increased interest recently due to its ability to be incorporated into the PLLA feedstock of 3D printers, allowing complex shapes to be formed [75-77]. However, though the HA powder filler makes the materials stronger in compression, it also makes them more stiff, less tough, and only mildly improves the osseointegrating properties.

In order to provide a better environment for hydroxyapatite anchors to form during osseointegration, and also in order to prevent the increased stiffness and reduced toughness fillers cause, many researchers look to morphologies other than powder when adding HA to their biopolymer. The inclusion of hydroxyapatite whiskers into biopolymers was investigated by Kane et al, finding that inclusion into collagen scaffolds increased the compressive elastic modulus of the material by an order of magnitude, and improve the fatigue properties of the material above that of blank collagen [78]. None of these studies investigated the fracture toughness of the material however, which is of key importance. Previous work by Todo et al has shown that the fracture toughness of HA containing PLLA does vary greatly depending on the geometry of the HA included [79]. Plate and sphere shaped microparticles of HA were incorporated into a PLLA matrix and their fracture toughness tested. It was seen that there was a slight difference in absorbed energy during fracture between different shaped particles. Importantly, it was also seen that the mechanism of fracture depended greatly on the shape of the particles, with plate shaped particles causing local ductile deformation, whilst spherical particles were causing smooth brittle fracture of the PLLA matrix.

Calcium phosphate powders have also been incorporated into a PCL matrix in previous studies. This option is very popular for use with 3D printers, as the low melting point of PCL allows for easy, low cost fused deposition modelling. Such printed composite scaffold materials have been shown to drastically increase the biological activity over blank PCL both *in vitro* and *in vivo* [80-82]. PCL has never been studied as a fibre filler in a calcium phosphate ceramic matrix however, which this study will investigate.

1.3 Mechanical characterization of biomaterials

An integral part of this study was to identify the fracture mechanism taking place in the biomaterial composite, and this was achieved using fracture surface analysis. By examining microstructures on fracture surfaces, one can understand the mechanisms of fracture which occurred [83, 84]. Firstly, three point bending tests are used on the materials expected to undergo large amounts of bending during use; the biopolymer bone plates with calcium phosphate microbead filler. Once fracture has occurred, the surface can be investigated under microscopy to identify features which tell how each fracture occurred. This will tell us whether the presence of microbeads changed the way the material fractures, and in doing so will explain why the fracture toughness might have changed.

The main distinction is whether the material fractured in a ductile or brittle fashion. Ductile fractures are slow moving, deforming fractures which leave behind distinctive markers on a fracture surface such as fibrils, voids and crazing [85]. These features are caused by the deformation and necking of small regions of material shortly before fracture. Brittle fractures on the other hand, are fast, clean breaks. The material undergoing brittle fracture does not have time to deform, or is too strongly bound. Visible features of a brittle fracture on a fracture surface are large, smooth areas where the material has shorn away along a grain boundary, or other such fault line. Brittle fracture surfaces are also more likely to show secondary cracks perpendicular to the fracture surface, as the high energy density in the material during fracture can cause other weak points to fracture too. In general, a far greater strain energy density is required within the material before a brittle fracture will occur, compared with a ductile one.

The fracture mechanisms of several specific biomaterials have been investigated, however almost all studies which look at the mechanical properties of calcium phosphate/polymer composites focus on particulate ceramic filler being blended with different kinds of polymer. Very few look at other geometries of bioceramic filler, or at using the polymer fibres as filler, as this study will do. For example, the integration of hydroxyapatite and β-tricalcium phosphate powder into various biopolymers and non-biopolymers has been investigated under compressive and tensile stress.

Wang *et al.* showed that hydroxyapatite powder in a matrix of the biopolymer polysulfone resulted in marked increases in the stiffness of the material with higher volume percentage, and corresponding reduced fracture toughness [86]. Fracture surface analysis of these specimens showed the reduced fracture toughness to be caused by debonding between the ceramic particles and the polymer, a fracture mechanism common to densely filled polymers, which should be considered in this study [87]. Other studies have shown this same response of increasing stiffness and reduced fracture toughness under tensile stress when incorporating hydroxyapatite powder into other biopolymers, and into the non-biopolymers polypropylene, polyether ether ketone (PEEK) and polyethylene [83, 87-89]. Ma *et al.* showed through fracture surface analysis, that hydroxyapatite powder caused PEEK to change from a ductile fracture mechanism to a brittle one, thus explaining the reduced strain to break and toughness [89]. However, Bonfield *et al.* used fracture surface analysis to show that in polyethylene, hydroxyapatite powders caused fracture by the same debonding mechanism as seen in polysulfone [83]. Liu *et al.* showed through similar analysis that hydroxyapatite in polypropylene also fractured by this debonding method [87]. The mechanism of fracture of hydroxyapatite

particles in chitosan was not determined, however further finite element simulations of this system have shown that the stress distribution within the material is much higher around the ceramic particles than in the polymer matrix, and that the geometry of the particle is important in determining the levels of stress present [90].

Abadi *et al.* and Fan *et al.* investigated another calcium phosphate material, *β*-tricalcium phosphate as a powder filler in polyethylene and the biopolymer poly(lactic-co-glycolic acid) (PLGA) respectively [84, 91]. Abadi *et al.* saw exactly the same increase in stiffness and reduction in toughness seen in polymers filled with hydroxyapatite, however Fan *et al.* determined that a single mechanism was not solely responsible for the change in fracture toughness of the PLGA. They showed that material stiffness actually decreased and fracture toughness increased with up to 10% β-tricalcium phosphate powder content. Correspondingly, the fracture surfaces showed increasingly ductile characteristics, switching from shear, smooth fracture surfaces of blank PLGA, to fibrillated, rough fracture surfaces for specimens containing the calcium phosphate. Above 10% powder content however, the material began to undergo the debonding fracture mechanism referenced above, and fracture toughness began to fall once more.

Out of all the studies referenced above however, it must be noted that almost all used only tensile testing to determine the mechanical properties and fracture mechanisms of the composite materials. Fan *et al.* alone used three point bending tests, and saw different behaviour than the others. In general, in the literature three point bending tests are not widely used, but for bone plate applications it is necessary as the main mode of fracture expected, and as has been shown, the mechanism of fracture is dependent on the mode of testing used.

The prevalence of the debonding fracture mechanism in biocomposites containing calcium phosphate powders shows the importance of filler geometry on the fracture mechanism. No existing studies have investigated calcium phosphate beads of the microscale investigated in this study, though similar beads have been fabricated and mechanically tested under compression individually. Perumal *et al.* fabricated hydroxyapatite beads with a small amount of magnesium additive for bone regeneration purposes, and found them to have a compressive strength of 52-80 MPa, though no further research was made using these beads [92].

The other geometry of filler which has been most widely investigated is hydroxyapatite whiskers, thin shards of hydroxyapatite crystals of nanometre scale. The importance of filler geometry is shown by Converse *et al.* [93]. They added an equal weight of hydroxyapatite whiskers and hydroxyapatite powder to a PEEK polymer matrix and compared how they changed the mechanical properties under tension. They showed that the whiskers caused the PEEK to change fracture mechanism similar to the powder, from a ductile fracture to a brittle one. However, the tensile strength of the composite actually increased once whiskers were incorporated, though no explanatory fracture mechanism is proposed to explain this. Wu *et al.* modified the surface properties of hydroxyapatite whiskers in order to investigate whether the polymer/ceramic interface was the key variable in explaining the unusual mechanical properties of hydroxyapatite whiskers, though they used the biopolymer PLGA for their study [94]. They saw that modifying the hydroxyapatite whisker surface to encourage wetting of the polymer matrix greatly increased the elongation to break and tensile strength of the composite, compared with ordinary hydroxyapatite whiskers.

Overall then, it can be seen that the mechanical characterization of biomaterials is generally underreported, and that the specific materials, geometries and testing regimes used to analyse composite materials greatly affects not only the reported figures for strength, toughness and stiffness, but more importantly the fracture mechanisms causing failure.

1.4 Problem statements

Current biopolymer and bioceramic implants are homogenous, and used only for non-load bearing and cosmetic applications [95, 96]. In order to move to the next generation of biomaterial implants, the material and biological properties need to be improved by investigating and fabricating composites. Biopolymer bone plates and screws are easily fractured, and prone to dislocation from the bone, which can cause secondary fracture, infection and immunological response. In order to combat this, researchers have tried including calcium phosphate fillers into biopolymers, with mixed results [80, 81]. Material properties seem to depend strongly on the geometry of the ceramic filler incorporated, but the geometry of bioceramic microbeads in a biopolymer matrix has never been examined [74, 78, 79]. It is critical that the fracture mechanism of this composite is understood if it is to be improved and iterated upon, and this is also currently unknown.

Modern materials used to treat vertebral compression fractures are likewise flawed. Using PMMA as the material in kyphoplasty has been shown to cause a three to five times increase in the number of secondary fractures which occur [16]. The exothermic setting of PMMA also leads to cell necrosis in the surrounding bone, and the mismatch in

stiffness of the polymer with bone leads to stress shielding and increased loads on other vertebrae [17, 18]. Research suggests that the relationship between stiffness and secondary fractures is in fact inversely proportional, and so finding a bioabsorbable material which can match the stiffness of bone whilst being strong enough to withstand strong compressive forces is of vital importance [19, 20].

By incorporating biopolymers and bioceramics into composites, these two problems can be addressed. Previous work on dental implants shows that the bioceramic microbeads in a biopolymer matrix will provide anchor points for osteocytes to grow, and initiate osseointegration of the implant much faster and more securely [97]. The fracture mechanics of this kind of material need to be investigated though, to understand how the parts of the composite interact and in order to optimize mechanical properties through iteration.

Regarding kyphoplasty, using a bioceramic matrix with a biopolymer fibre filler as the injectable material is very promising. Usually, biopolymer fibres are woven as meshes or used as yarns for stitching. However, by incorporating the fibres into a bioceramic matrix, the material can be strengthened and made more flexible, preventing the secondary fractures caused so commonly by the current standard materials, whilst maintaining the excellent osseointegrating ability and injectability of the ceramic.

1.5 Goal of study

The goal of this study is to fabricate and mechanically test two new composite biomaterials for two applications. Both materials will use calcium phosphate ceramics as one component, and a naturally derived biopolymer as the second. The first composite will consist of microbeads calcium phosphates in a biopolymer matrix. Three biopolymers will be investigated; PLLA, PCL and a 50:50 blend of the two. These composites will be for use as bone plates, and so must be tested for elasticity and fracture toughness in the bending mode, and their mechanisms of fracture must be determined.

The second composite will be of PLCL fibres as filler in a calcium phosphate ceramic matrix, for use as an injectable material in kyphoplasty surgery. The composite needs to be formed from an anhydrous slurry exposed to physiological conditions in order to show that the material is suitable in kyphoplasty surgery. In compression, this material needs to be as strong as cancellous bone and have a comparable flexibility. The reason for any changes in these material properties caused by the inclusion of PLCL fibres needs to be understood.

CHAPTER 2: MICROBEAD / BIOPOLYMER COMPOSITES

2.1 Overview

The process of creating calcium phosphate microbeads was based on the entrapping of calcium phosphate powder via the ionotropic gelation cross-linking of calcium alginate and subsequent sintering. The four-step process begins by creating a slurry of calcium phosphate powder in sodium alginate solution. Both hydroxyapatite powder and α-tricalcium phosphate powder were tested as the initial form of calcium phosphate, as well as various powder-to-liquid ratios. The slurry is then dripped into chilled calcium chloride solution through a needle in order to cross-link the alginate and constrain the calcium phosphate powder into spheres by a process called ionotropic gelation. The spheres of calcium phosphate powder bound in calcium alginate are then dried at room temperature under specific conditions, before being fired at high temperatures to remove the organic alginate and sinter the calcium phosphate. The effects of this process were then analyzed too, using scanning electron microscopy and X-ray diffraction spectroscopy.

2.2 Materials and fabrication methods

2.2.1 Formation of calcium phosphate/alginate beads

In order to fabricate microbeads of calcium phosphates, an ionotropic gelation method of cross-linking alginate was employed. This method allows the entrapment of solid particles in a robust alginate gel. The method has previously been employed in other research to entrap drugs for drug delivery applications. [98-100]

Sodium alginate is the reagent, existing as a soluble, single chained polymer with stoichiometrically two +1 charge sodium ions per monomer, bonded to two -1 charge COO^- carboxylate groups. Upon the introduction of calcium chloride in excess, every two sodium ions is replaced by a +2 charge calcium ion. This causes the bonding of disparate polymer chains via the calcium ions, as shown in Figure 2.1. These calcium ions act as cross-links, connecting disparate parts of the polymer chain and other polymer chains, and precipitating gelation, trapping solid particles within the gel matrix. Sodium chloride salt byproduct is washed away during the production process. Calcium chloride acts as a polymerizing agent in this way by ionotropic gelation cross-linking.

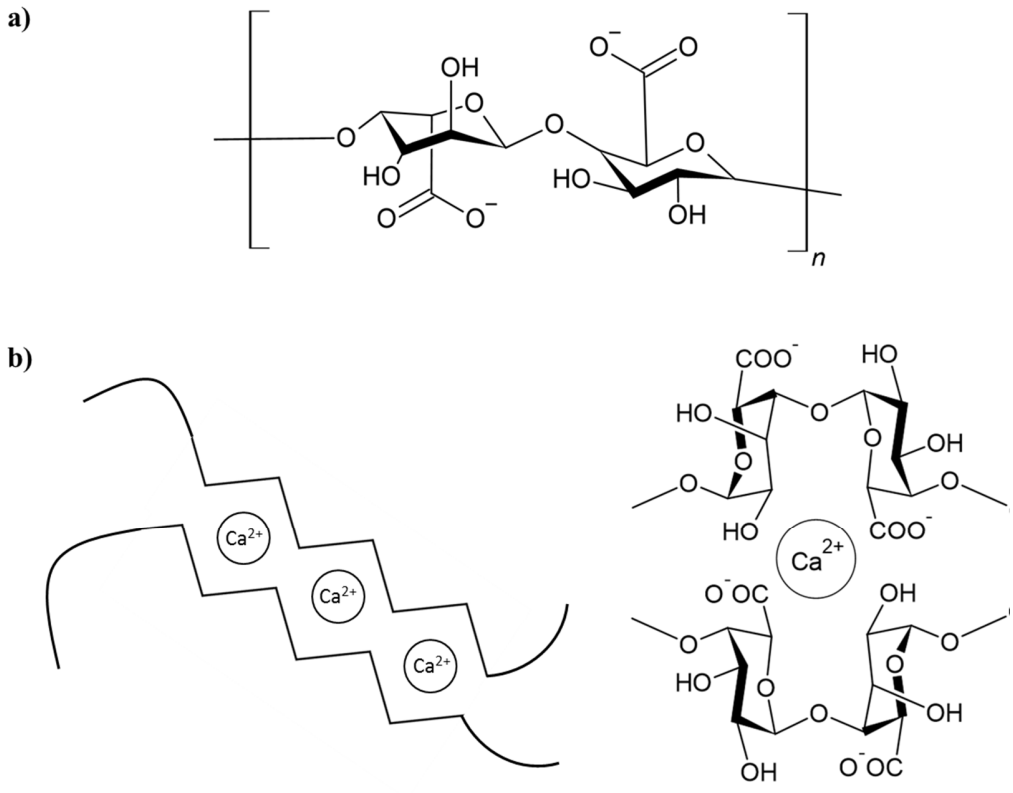

Figure 2.1 a) structure of alginate, b) two alginate polymer chains interacting with Ca^{2+} ions to cause ionotropic gelation

Practically, a two-step process was used to produce this effect. Firstly, a calcium phosphate powder and 1% sodium alginate aqueous solution were blended and subjected to ultrasonic dispersion to create five slurries of P/L ratios from 1:5 to 1:20. Two calcium phosphates were used; α-TCP powder and hydroxyapatite powder at each of these ratios. The slurries were then dripped into a 4°C 1% calcium chloride aqueous solution through needles of varying diameter to produce beads of differing radii, as shown in Figure 2.2. The differences in bead size, roundness, and ease of production with regards to each of these variables is analyzed. Finally, the calcium phosphate/ alginate beads were washed and dried sequentially in ethanol at 70/90/95/100% concentrations, then at room temperature in air for 24 hours. During all drying stages, the beads were uniformly agitated using a rotating plate to ensure the round shape was not deformed.

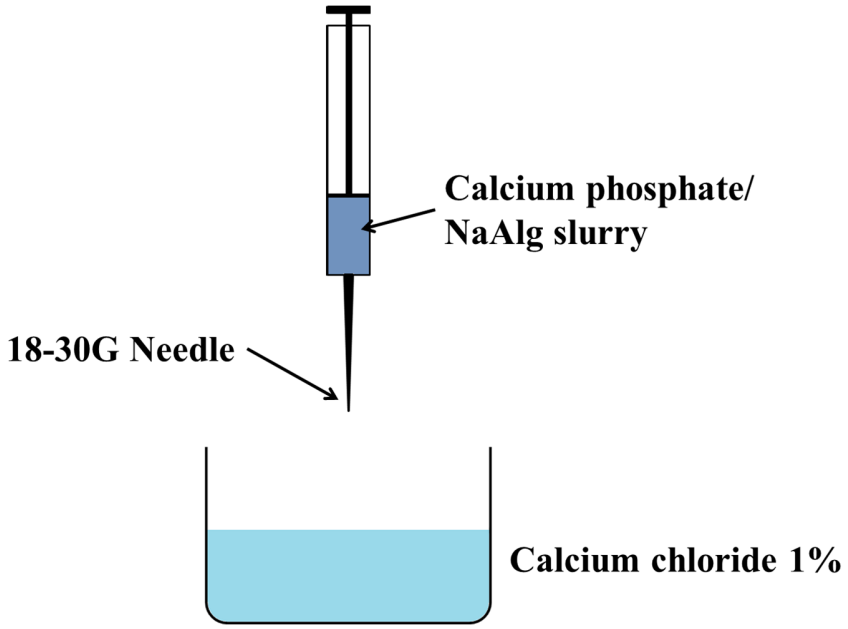

Figure 2.2 Experimental setup for creating calcium phosphate/alginate microbeads.

2.2.2 Sintering of microbeads

Dried microbeads were then sintered at 1100°C to remove organic components and produce the final calcium phosphate material. The sintering process used an electric furnace to sinter microbeads at the temperature of 1100°C for 4 hours, before passively cooling to room temperature. By comparing the density of beads before and after sintering, an estimate of the alginate mass percentage was also made. Only beads made from α-TCP powder were sintered, as hydroxyapatite powder was found to not form uniform, round beads suitable for further use.

2.2.3 Fabrication of composite materials

Composite materials of the microbeads and PLLA, PCL and a 50:50 blend of PLLA and PCL biopolymer were fabricated using a mechanical hot press as it is a method easily scalable for industry, and generates consistent, repeatable samples in a cost effective way.

The PLLA/PCL blend was fabricated by using the crashing-out method. Equal weight of each biopolymer was dissolved in an excess of dichloromethane at 60°C under reflux. Once fully dissolved, the solution was quickly dumped into a bath of distilled water at 4°C, of at least ten times greater volume. This immediately caused solid, blended PLLA/PCL to precipitate out of the solution, which was then filtered out, dried under atmospheric conditions for 24 hours, and used in further processes. The blended polymer was investigated using SEM and DSC to determine its phase structure and thermal properties.

The blended polymer powder, PLLA pellets, or PCL pellets of medical grade were placed in a 100mm x 100mm x 5mm brass mould. This size was chosen to allow bars to be cut from the plate of the correct proportions for standardized mechanical testing, outlined in Figure 2.3. The thermal properties of each component biomaterial are shown in Table 2.1.

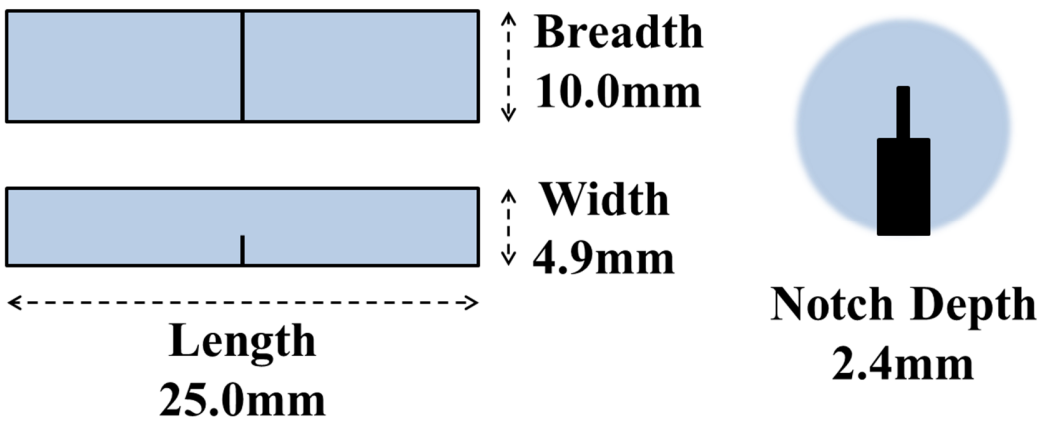

Figure 2.3 Geometry of samples for three point bending tests showing location of notch for those samples which required notching.

Table 2.1 Relevant material and thermal properties for hot pressing of biopolymers.

Material	**Manufacturer**	**M_n / gmol^{-1}**	**T_g / °C**	**T_m / °C**
Poly(*L*-lactic acid)	Shimadzu Co. Ltd.	200,000	60	178
Poly(ε-caprolactone)	Shimadzu Co. Ltd.	80,000	-60	62

After filling the moulds to three quarters full with biopolymer, the microbeads were then distributed evenly across the surface using square grids. Various amounts of beads were used to produce different average microbead volume fractions within the material, ranging from 0% to 11% of total material volume. Table 2.2 outlines the required masses of biopolymer and microbeads required to produce a 100mm x 100mm x 5m plate of each sample group. The moulds were then topped up with biopolymer and placed in the hot press. Each was heated to 185˚C, under a pressure of 10MPa for 2 hours, and then allowed to cool to room temperature whilst still under pressure overnight. After hot pressing, the composite plates were cut into smaller bars using a band saw, to be mechanically tested. Specimens which were to be tested for fracture toughness were then notched at their centre to a depth of half their width, *W/2*, as per the geometry shown in Figure 2.3.

Table 2.2 Relative abundance of biopolymer and microbeads in each sample group, for a 100mm x 100mm x 5mm plate fabricated in a hot press.

Microbead vol fraction / vol%	**Biopolymer mass / g**	**Microbead mass / g**	**Total mass / g**
0	62.0	0.0	62.0
2	60.8	3.2	64.0
5	59.0	7.9	66.9
9	56.4	14.2	70.6
11	55.2	17.4	72.6

2.3 Characterization

2.3.1 XRD & SEM

A Rigaku MiniFlex II Tabletop X-ray diffractometer was used to determine the presence of hydroxyapatite in the sintered beads, by comparing the spectrographic peaks of powdered, sintered microbeads with those of pure α-TCP and pure HA. Samples were manually ground and packed onto steel plates. XRD was performed using filtered CuK-α band X-rays generated at 30kV and with 15mA.

Beads were further characterized by careful examination under a scanning electron microscope to determine roundness and diameter. Approximately one out of every fifty beads made was removed from the group and analyzed in this manner. SEM was also used to determine any phase separation of PLLA and PCL in the blended mixture.

2.3.2 Three point bend testing

Three point notched bending methods measure the Mode 1 fracture toughness of a material, meaning its ability to resist a tensile stress normal to the plane of the crack. The three types of fracture which can occur in a material are; Mode 1, opening; Mode 2, in-plane shear; and Mode 3, out of plane shear. As these materials are intended for use as thin, flat bone plates, bending stresses are the most likely to cause fracture, and as such only the Mode 1 fracture is likely to occur and cause failure.

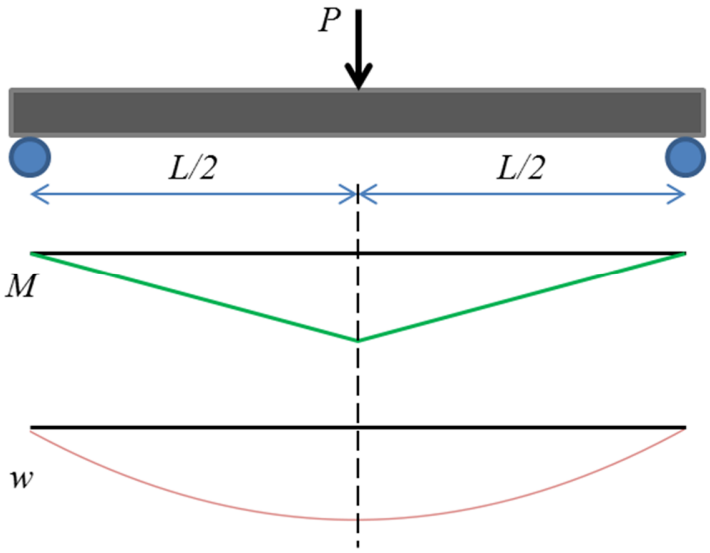

Figure 2.4 Loading arrangement for a three point bending test, as well as moment of bending, *M*, and deflection, ω, across the beam.

In order to perform a three point bending test, a beam of known geometry is supported at both ends by rollers, a distance *L* apart, and the concentrated load, *P*, is applied at the centre, as shown in Figure 2.4. The loading head at the centre point can be moved downward at a constant speed, giving constant strain, whilst measuring the load. This gives a measure of the material's properties. Mathematically, the moment of bending and the deflection of the material during loading are known empirically, and are also shown in Figure 2.4. It can be seen that the material experiences tensile stress along the convex side of the beam, while experiencing compressive stress along the concave side of the beam. This is what causes the mode 1 opening fracture to occur. The forces are highest at the beam's centre, as that is where the largest bending moment occurs, as shown in Figure 2.4. The deflection of the beam at this central point can be expressed by the following equation.

$$\omega_{centre} = \frac{PL^3}{4Eb^3W} \qquad 2.1$$

Where ω_{centre} is the deflection on the beam at the beam's centre, underneath the load head, E is the Young's elastic modulus of the material, b is the beam breadth and W is the beam width, as shown in Figure 2.3.

2.3.2.1 Young's elastic modulus

In order to calculate the Young's elastic modulus from a three point bending test, the above Equation 2.1 can be rearranged as follows.

$$E = \frac{P}{\omega}\frac{L^3}{4b^3W} \qquad 2.2$$

The Young's elastic modulus can therefore be seen to be proportional to the rate of change of load with respect to displacement, as the second term relates only to the beam's geometry and is constant. By finding the slope of a graph of load against displacement, at constant strain, the Young's elastic modulus of a material can thus be calculated. An example load displacement curve from this type of measurement is given in Figure 2.5.

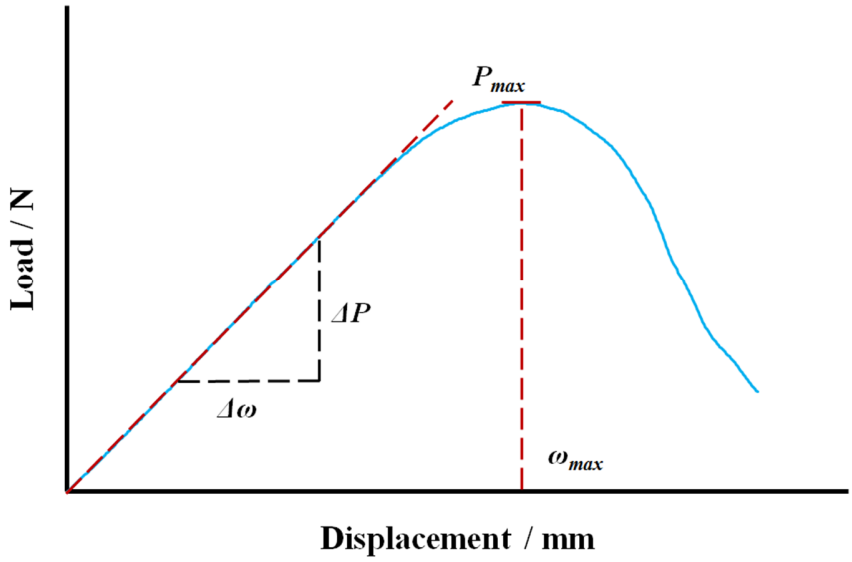

Figure 2.5 Example load displacement curve showing tangent line for calculation of *E*

2.3.2.2 Critical stress intensity factor, K_{IC}

The critical stress intensity factor of a material can be considered a constant measure of toughness for an isometric material in a plane strain condition. Materials were fabricated for these tests to be of suitable thickness as to avoid a plane stress condition, which would produce an artificially high toughness, as outlined in ASTM E399 [101]. As fractures almost always initiate from a defect or crack in a material, fracture toughness testing on notched specimens is performed. The critical stress intensity factor of a material is a measure of the strength of the material once a crack has already formed. By controlling the position, depth and width of the crack, a model can be built around it to give repeatable and accurate measurements. Figure 2.6 shows a notched specimen ready for fracture toughness testing in this manner. The notch depth, *a*, is approximately one half of the total breadth of the sample; it has a *a/b* ratio of 0.5. Notches were cut using a 1 mm width diamond wire saw and then the sharp crack tip was cut using a razor blade

with 0.8 µm diamond slurry. The crack had to be situated as close to the centre of the cut notch as possible and angled parallel to the notch. In order to confirm that the notch was situated and angled correctly, images of each side of the notch were taken using an optical microscope and crack angles measured using image analysis software. Any cracks which deviated from the parallel by more than 5° were discarded.

Once the material sample is notched, three point bending tests are performed and load-displacement curves of each sample are measured. The important variable to isolate from the load-displacement curves of these samples in order to calculate the critical stress intensity factor is P_Q, the peak load required to propagate a crack. It is shown in ASTM E399 that this value is equal to the intersection of the 5% secant of the load displacement curve and the curve itself. In situations where the intersection P_Q is beyond the peak of the load displacement curve, P_{max}, the value P_{max} is taken to be equal to P_Q. Figure 2.7 shows the construction used to determine P_Q.

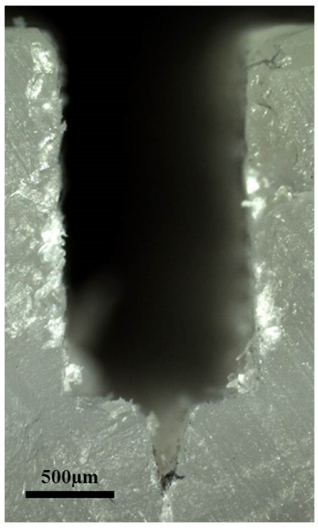

Figure 2.6 Notched PLLA sample under optical microscope, angle < 1° from normal.

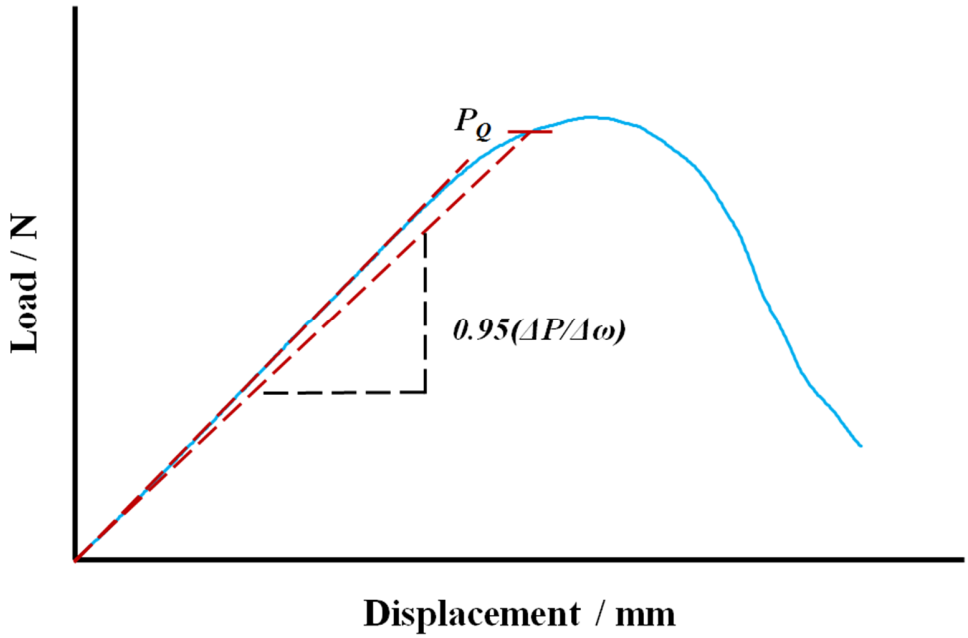

Figure 2.7 Example load displacement curve showing secant line for calculation of K_{IC}

2.3.2.3 Critical strain energy release rate, G_{in}

A three point notched bending test can also be performed in order to determine the critical strain energy release rate, G_{in}. Once the load-displacement curves of samples are determined, the area under the load-displacement line up until the point of crack initiation, P_Q, as shown in Figure 2.8. This method provides another measure of fracture toughness, measuring the amount of energy needed by the material in order to initiate a mode 1 fracture. The equation used to determine the critical strain energy release rate, G_{in}, from the value of the area beneath the curve, U_{in}, and the sample beam geometry is as follows., where the width and breadth of the sample beam are W and b respectively, and φ is a geometric correction factor given as a function of x, which is the ratio of the notch depth to the width of the sample, a/W.

$$G_{in} = \frac{U_{in}}{Wb\varphi} \qquad 2.3$$

$$\varphi = \frac{\emptyset(x) + 18.64}{d\emptyset(x)/dx}$$

$$\emptyset(x) = \frac{16x^2}{(1-x)^2}(8.9 - 33.717x + 79.616x^2 - 112.952x^3 + 84.815x^4 - 25.672x^5$$

$$\frac{d\emptyset(x)}{dx} = \frac{16x^2}{(1-x)^2}(-33.717 + 159.232x - 338.856x^2 + 339.26x^3 - 128.36x^4)$$

$$+ 16(8.9 - 33.717x + 79.616x^2 - 112.952x^3 + 84.815x^4$$

$$- 25.672x^5)\left(\frac{2x(1-x) + 2x^2}{(1-x)^3}\right)$$

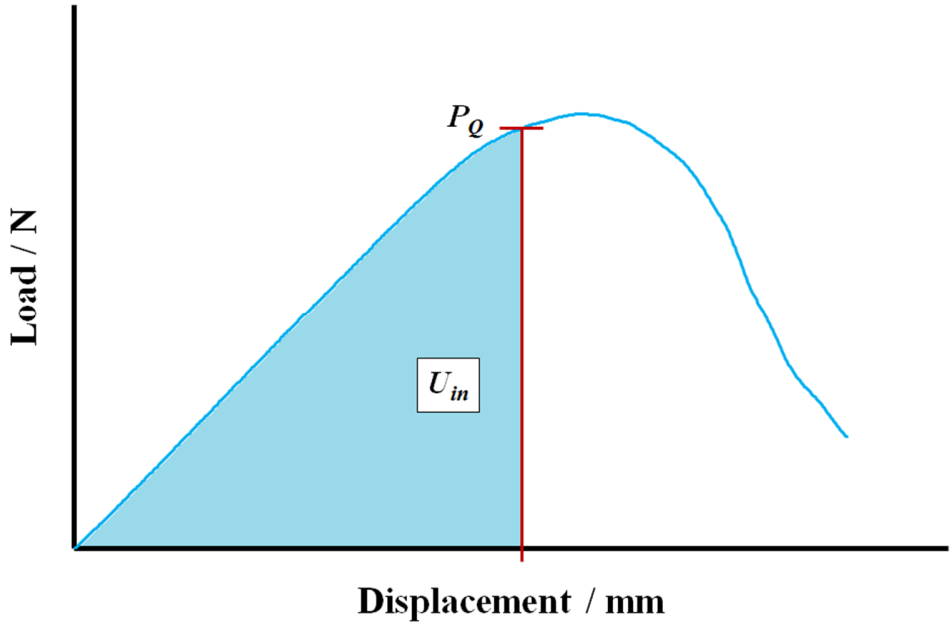

Figure 2.8 Example load displacement curve showing U_{in}, the area under the curve until P_Q for calculation of G_{in}.

2.3.3 Fracture surface analysis

Fracture surfaces of each group from notched bending tests were analyzed under optical microscopy and scanning electron microscopy in order to see if the macroscopic and microscopic features could be correlated with any fracture modes. These analyses were then in turn correlated with fracture testing data to form a hypothetical fracture mechanism.

The electron probe microanalysis (EPMA) was also used to measure the calcium elemental concentrations across the fracture surface using x-ray spectrometry, focusing on the areas around the microbeads. This was done in order to determine if any calcium leakage into the surrounding polymer matrix had occurred, or contrarily, if any intrusion by the polymer into the microbead had occurred. This is useful, as the fracture mechanism will depend on the interaction between the polymer and ceramic surface.

2.3.4 Finite element analysis

Finite element analysis software, Mechanical Finder v10.0EE was used to simulate the stress-concentration effects of notched bend testing on the PLLA specimens under different concentrations of microbead filler [102]. This was done in order to view the transient properties of the material as it underwent loading, most importantly the strain energy density (SED) of the material surrounding the microbead near to the fracture initiation site, and of the region between beads in the two bead tests, in order to better understand the fracture mechanic responsible. Figure 2.9 shows the simplified models used; created using the 3D design software SketchUp Pro [103].

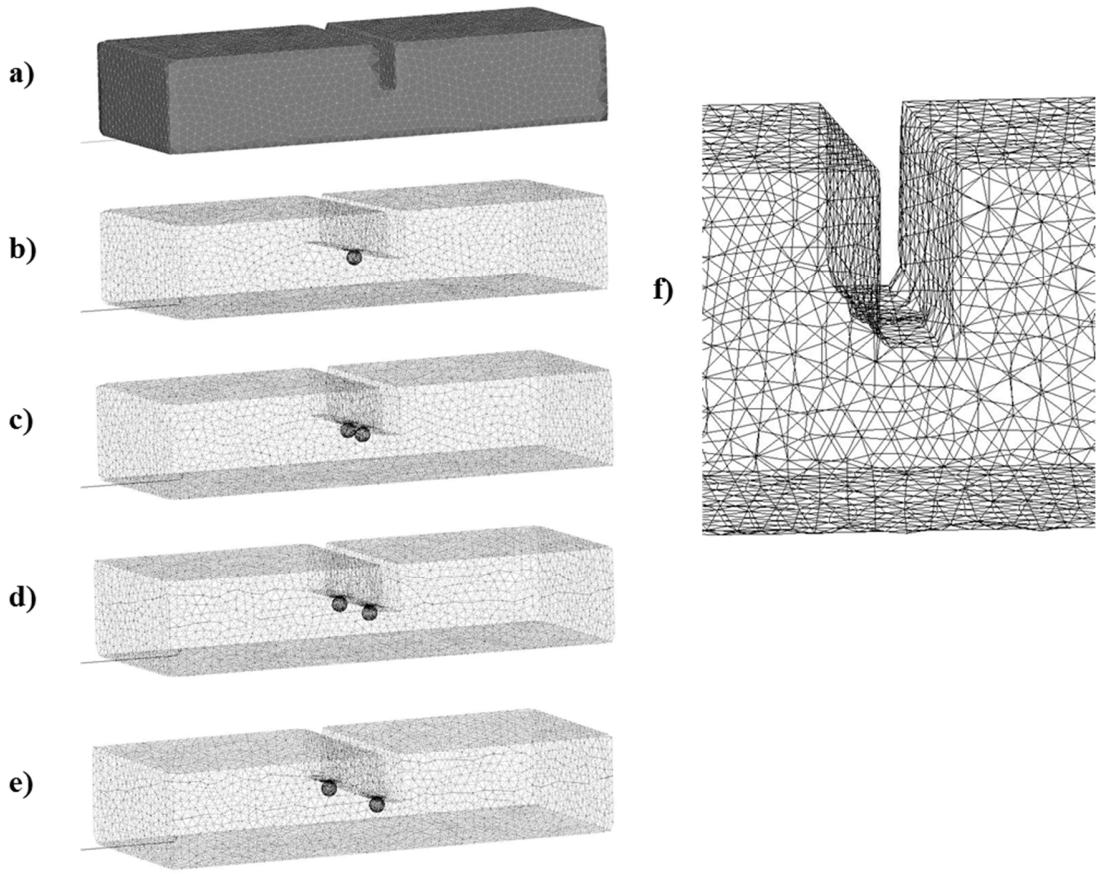

Figure 2.9 Finite element models for analysis of three point bending tests of PLLA containing a) no microbeads, b) a single microbead, and c), d) and e) two microbeads at 2mm, 4mm and 6mm separation respectively, f) along the crack initiation line.

The variation in inter-bead distances in the two bead models covers the range of inter-bead distances seen in the physical specimens of all bead volume concentrations, 2-6mm. Young's modulus E and Poisson's ratio ν of the calcium phosphate ceramic (E=15.0 GPa, ν=0.45) and PLLA (E=2.63 GPa, ν=0.25) were obtained from literature [104-107]. The data is extracted from the elements within the crack tip region, shown in Figure 2.9 f). Each specimen was restrained as in a notched three point bending test; with a forced displacement applied in the central loading position and two restraints applied 2.5mm from each specimen edge, as shown in Figure 2.10. The load was applied in 10 steps of 0.04mm displacement for a total displacement of 0.4mm in order to determine strain energy density (SED) values within the material before significant fracture occurs.

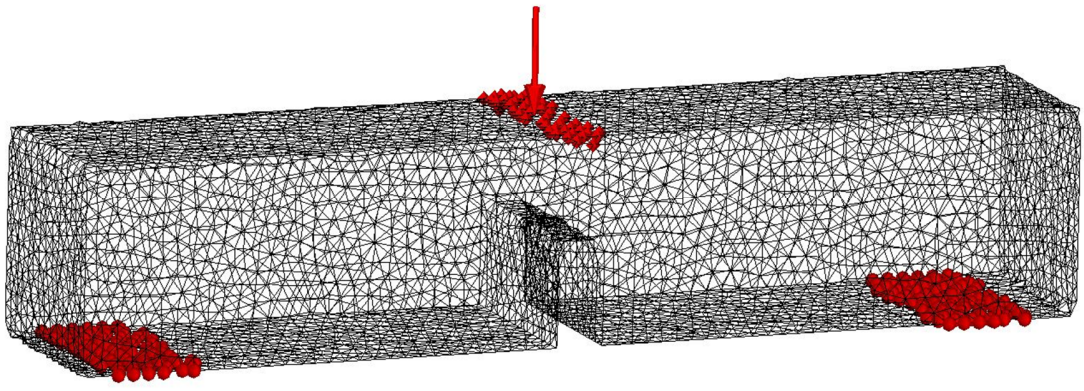

Figure 2.10 Boundary conditions showing two restraints and one central loading position (arrow) in red; used for FE analysis of all models.

A fracture analysis of the models was also performed in order to see when and where the fracture occurs, to determine if this is in agreement with the physically observed results. The analysis is focused on the notched area of the sample, where the crack initiation will occur under tension during the three point bending test. As such, the failure criterion for each element was defined as the principle stress in tension with a critical value of 50MPa. These analyses used a larger displacement to ensure fracture; 5 steps of 0.2mm, for a total displacement of 1.0mm. When investigating fracture rates the stiffness of the microbeads was also varied between 5-50GPa, to investigate whether this had a significant effect. The calculations were all performed was using a linear elastic model and the number of elements and nodes of each FE model is given in Table 2.3.

Table 2.3 Elements and nodes used in FE models.

Model	**Elements**	**Nodes**
Blank	137487	25046
Single microbead	148634	27002
Double microbead 2mm	159389	28894
Double microbead 4mm	205257	37636
Double microbead 6mm	205208	37644

2.4 Results and Discussion

2.4.1 Microbeads

It was found that following the procedure for ionotropic gelation outlined in Figure 2.2 resulted in 5 different outcomes, depending on needle gauge and *P/L* ratio. By testing each combination of needle gauge and *P/L* ratio, an optimized setup was established. The five outcomes which occurred were as follows:

1. Blocked - complete blockage of the needle, resulting in no bead formation.
2. Beads – Smooth flow of slurry, resulting in round microbeads.
3. Pancake – Smooth flow of slurry, but too much volume or too dilute, leading to deformation of bead shape upon impact with the calcium chloride solution.
4. Irregular – slurry flowed but did not dissociate into distinct droplets, resulting in irregular shaped pieces of entrapped calcium phosphates.
5. Flow – Slurry flowed too freely, resulting in “strings” of entrapped calcium phosphate rather than distinct microbeads.

Table 2.4 shows which combinations of needle gauge and *P/L* ratio produced which result. It can clearly be seen that the 23G and 25G needles performed best, whilst the *P/L* ratios of 1:5 and 1:8 also performed best. It was seen that for ease of operation and quantity of microbeads produced, the set up with a 25G needle and *P/L* ratio of 1:8 was optimal. For all further experiments, microbeads mentioned were fabricated using this optimized setup.

Table 2.4 Results of microbead fabrication with varying needle gauge and *P/L* ratio.

	1:3	**1:5**	**1:8**	**1:10**	**1:20**
18G	Blocked	Blocked	Blocked	Blocked	Irregular
20G	Blocked	Blocked	Beads	Pancake	Irregular
23G	Blocked	Beads	Beads	Pancake	Irregular
25G	Blocked	Beads	Beads	Pancake	Flow
27G	Pancake	Beads	Irregular	Pancake	Flow
30G	Pancake	Flow	Flow	Flow	Flow

The mass difference before and after sintering was found to be 8.0±0.2 % across all beads made in the optimum method. A small amount of this mass is lost as phosphoric acid during the reaction of the calcium phosphate, however most of it is lost due to the alginate polymer burning. It can be estimated then, that microbeads were around 8% alginate before sintering. For the beads formed from HA powder, no change in the calcium phosphate occurred, and mass difference was found to be 10±1 %, meaning even more alginate was present in these microbeads before sintering.

The XRD taken to determine whether α-TCP had indeed converted in HA during sintering is shown in Figure 2.11. Full peak lists are given in Appendix A.1. The peaks appearing on the XRD spectrograph of the sintered calcium phosphate ceramic beads all correspond to those of either HA or α-TCP, suggesting that the expected reaction did convert α-TCP into HA during the sintering process. SEM micrographs of bioceramic beads are also shown in Figure 2.12. It is seen that the ceramic microbeads have successfully formed a biphasic calcium phosphate of α-TCP and HA, with an average bead radius of 850±50 μm.

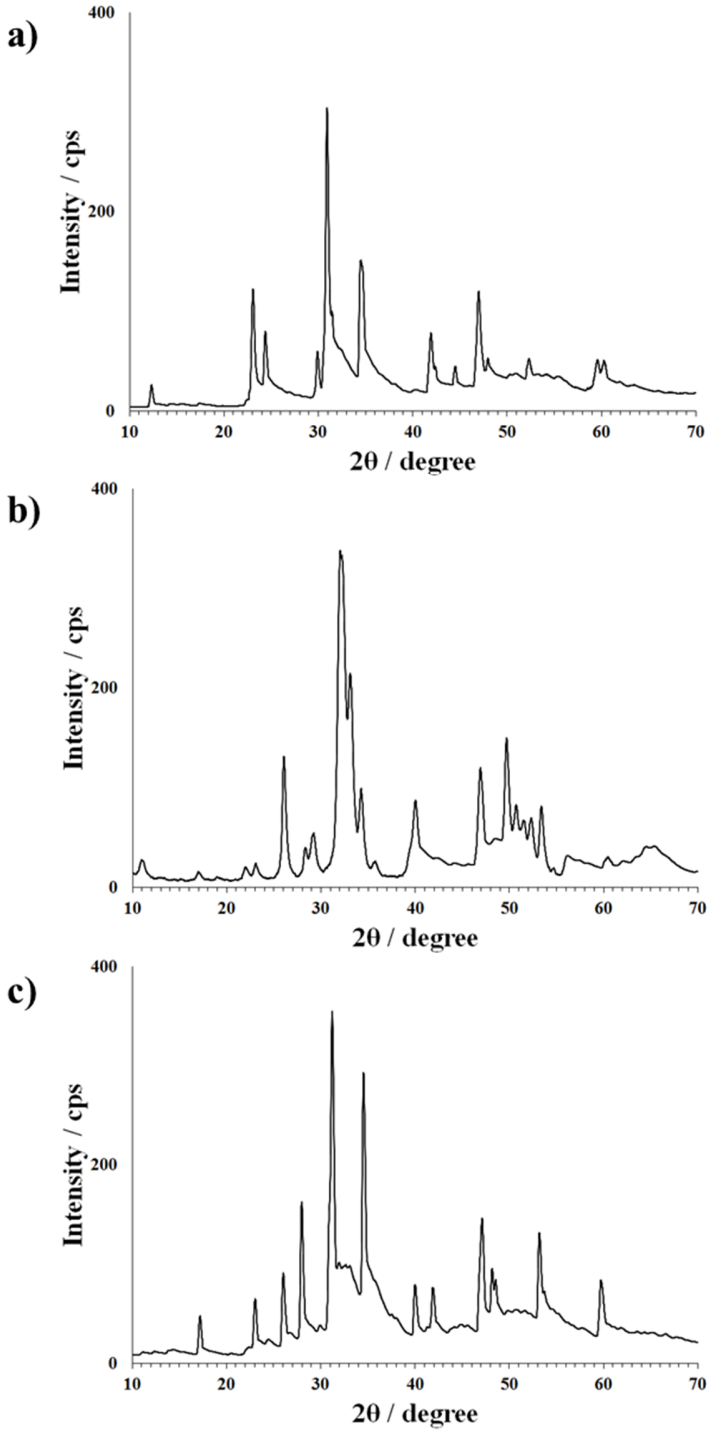

Figure 2.11 XRD spectrometry of a) α-TCP, b) HA and c) sintered bioceramic microbeads. The peaks in the bioceramic microbead spectrum correspond to those of either HA or α-TCP.

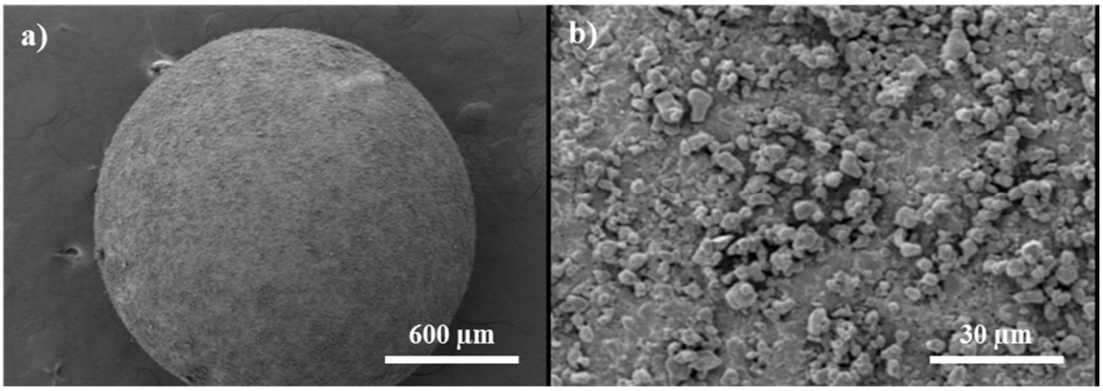

Figure 2.12 SEM micrograph of microbead a) to measure diameter, b) to confirm presence of HA crystals.

The beads composed of HA powder encapsulated by the ionotropic gelation method were discarded, as they failed to form microbeads of regular shape or size. Figure 2.13 shows a micrograph of such beads compared to α-TCP beads. As the sintering process successfully converted the α-TCP into a biphasic calcium phosphate containing HA, it was determined the pure HA beads were unnecessary to investigate further.

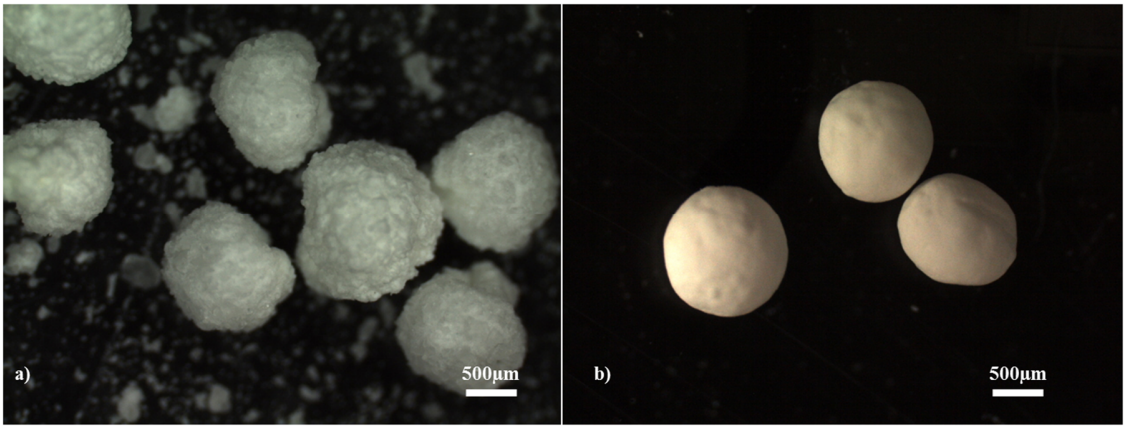

Figure 2.13: Optical micrograph of a) HA and b) α-TCP microbeads after gelation.

2.4.2 Microbead/ PLLA composite

2.4.2.1 Chemical and micro-structure

Inclusion of bioceramic microbeads into the PLLA matrix was successful, as shown in Figure 2.14, with even distributions of beads at consistent volume concentrations being found. The average distance between beads for each sample group was determined by observation, and was found to follow the expected distribution. The sample groups produced, and average distance between beads of each group is given in Table 2.4. The distance between beads reported were determined by averaging distances between 10 beads in each sample, for 10 samples per group, therefore *n=100* for the average of each group.

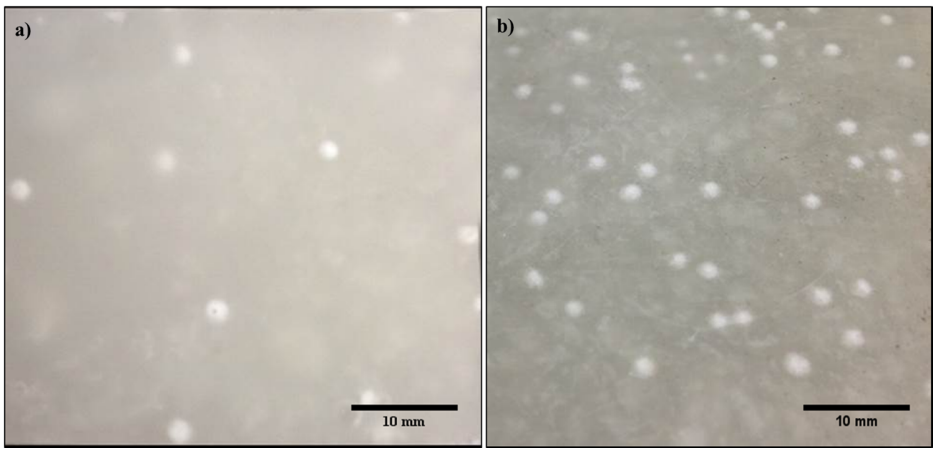

Figure 2.14 Optical micrographs of PLLA composite with a) 2%w/w and b) 11%w/w calcium phosphate microbeads.

Table 2.5 The volume fraction of microbeads in each sample group, along with the measured average distance between beads in each group.

Microbead vol. fraction / vol%	**Av. distance between microbeads / mm**	**Standard deviation / mm**
2	6	1
5	4.5	0.6
9	3.6	0.2
11	3.3	0.2

2.4.2.2 Mechanical properties

Young's modulus, *E*, did not significantly vary across all groups, as shown in Figure 2.15. This graph shows how the initial inclusion of microbeads into the material caused only a slight increase in *E*, from 0.55 GPa to 0.76 GPa, equivalent to within error and in agreement with recognized values for PLLA [26]. The slight increase in *E* seen with increasing microbead volume concentrations is also ambiguous within error.

The load-displacement curves measured during K_{IC} fracture tests of the specimens are shown in Figure 2.16. Any inclusion of microbeads in the PLLA matrix caused a sudden decrease in displacement to fracture, a sharp decrease in peak load, and a small increase in initial stiffness, i.e., the initial slope of the curves. Microbeads also caused a sharper fracture profile, indicating a brittle fracture mechanism was responsible. Increasing concentrations of microbeads however, did not cause more brittle fracture behaviour, but instead simply reduced the displacement and peak load required for the same type of fracture to occur.

The average calculated critical stress intensity factor, K_{IC}, for each group of specimens is shown in Figure 2.17. K_{IC} decreased by at least 47% with microbead inclusion, from 34 Pa.m$^{-1/2}$ for bulk PLLA, to 18 Pa.m$^{-1/2}$ for the strongest bead containing group, 2 vol% microbead fraction. At increasing bead volume fractions however, K_{IC} fell off more gently, decreasing only to 8.4 Pa.m$^{-1/2}$ by 11 vol% microbead fraction. This decrease was clearly linear in nature, and again indicates that all microbead containing specimens are fracturing under the same mechanism, one which is different from that of bulk PLLA.

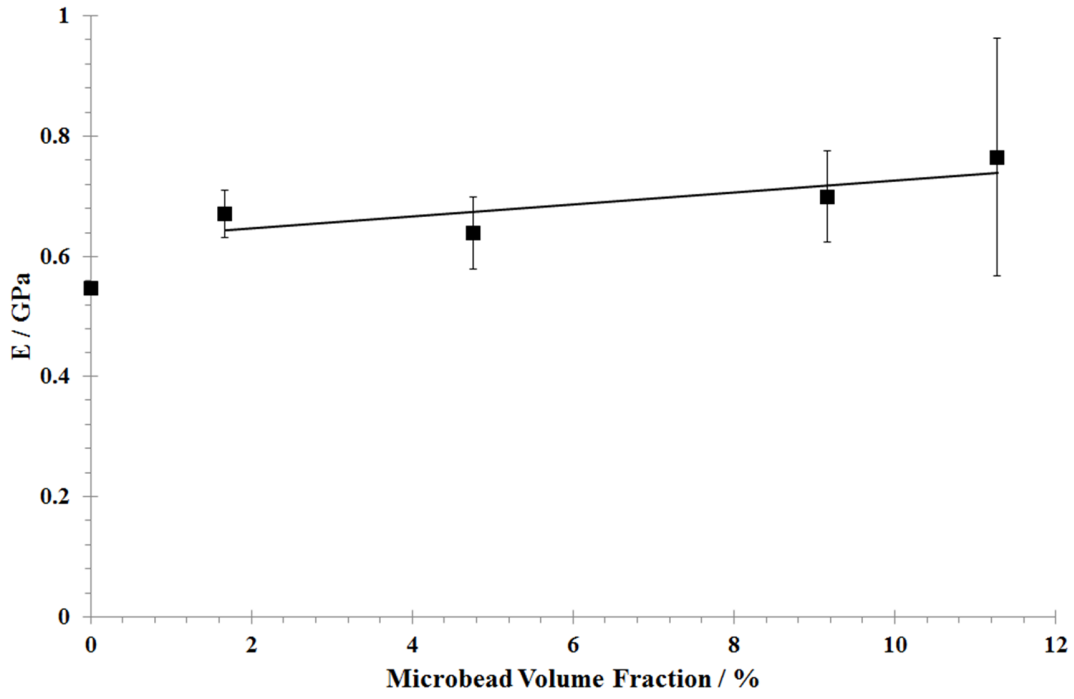

Figure 2.15 Young's modulus of PLLA/microbead composite materials with respect to microbead concentration.

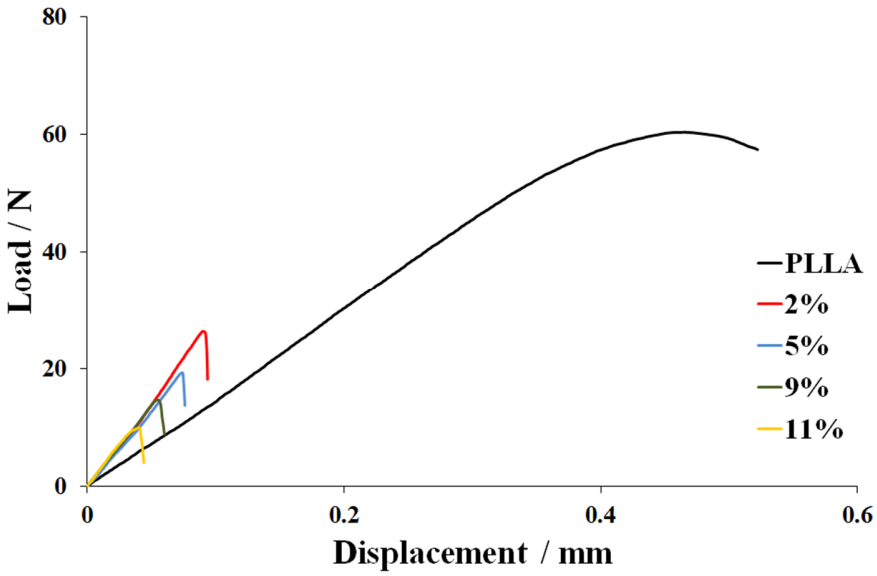

Figure 2.16 Load displacement curves obtained from three point bending tests, comparing mechanical behaviour of PLLA with and without microbeads at all concentrations.

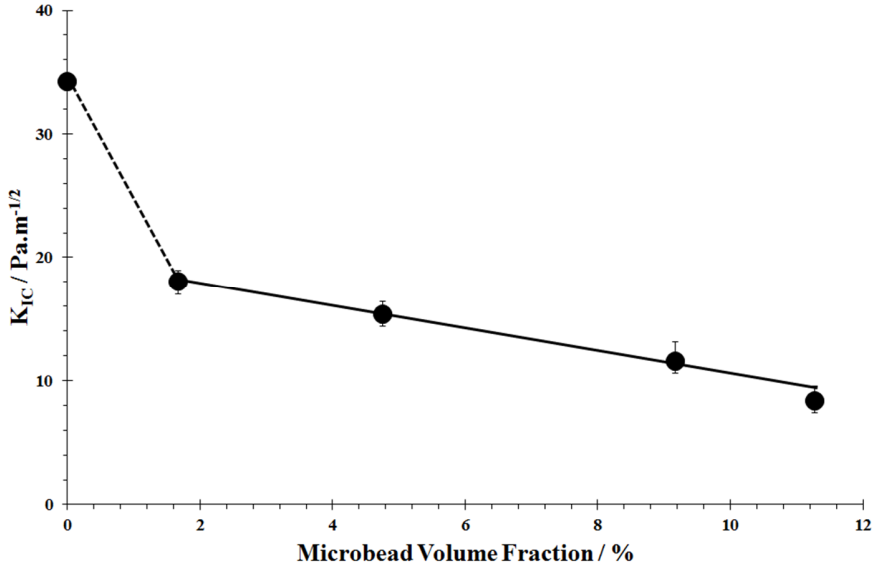

Figure 2.17 K_{IC} as a measure of fracture toughness of PLLA/microbead composite materials with respect to microbead concentration.

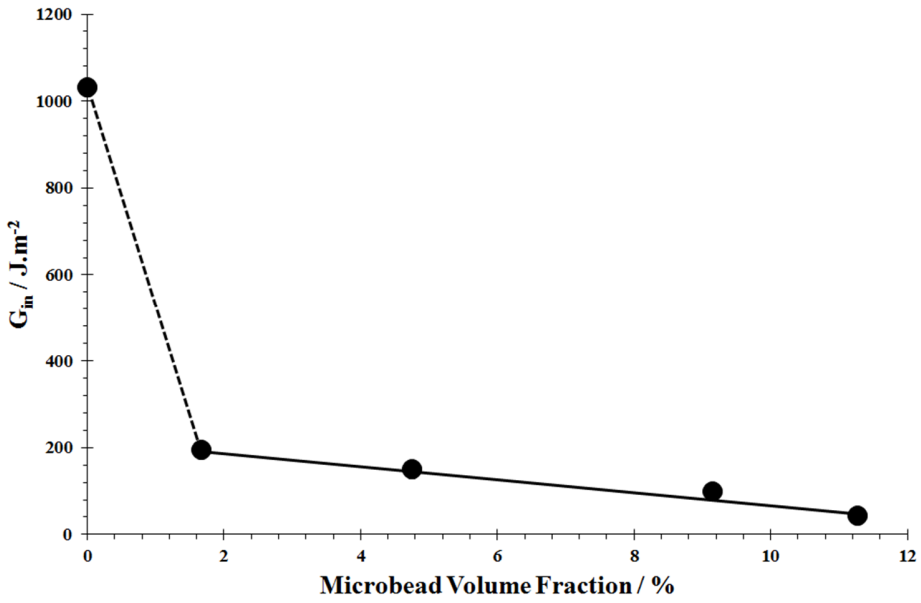

Figure 2.18 G_{in} as a measure of fracture toughness of PLLA/microbead composite materials with respect to microbead concentration.

Calculated values of the critical strain energy release rate, G_{in}, of each material showed a very similar pattern, as can be seen in Figure 2.18. Any inclusion of microbeads in the material reduced calculated G_{in} by at least 81%, from 1030 Jm^{-2} for blank PLLA to 200 Jm^{-2} for the best performing microbead containing group, again the 2 vol% group. Increasing the microbead volume fraction lead to a gentle, linear decrease in G_{in}, similar to that seen in K_{IC} calculations, with the 11 vol% group having a G_{in} of 43 Jm^{-2}.

2.4.2.3 Fracture surface analysis

Optical microscope imaging of the fracture surfaces showed clear differences between the composite and the bulk PLLA, as was expected from the mechanical testing data. Figure 2.19 shows the fracture surface of bulk PLLA under optical magnification. Clearly visible are hackle patterns and areas of fibril formation caused by a slow, ductile fracture. SEM micrographs of the same surface, shown in Figures 2.19b, c & d confirm this analysis, with both hackle patterns, fibril formation and void formation visible at all scales from the macroscopic to microscopic.

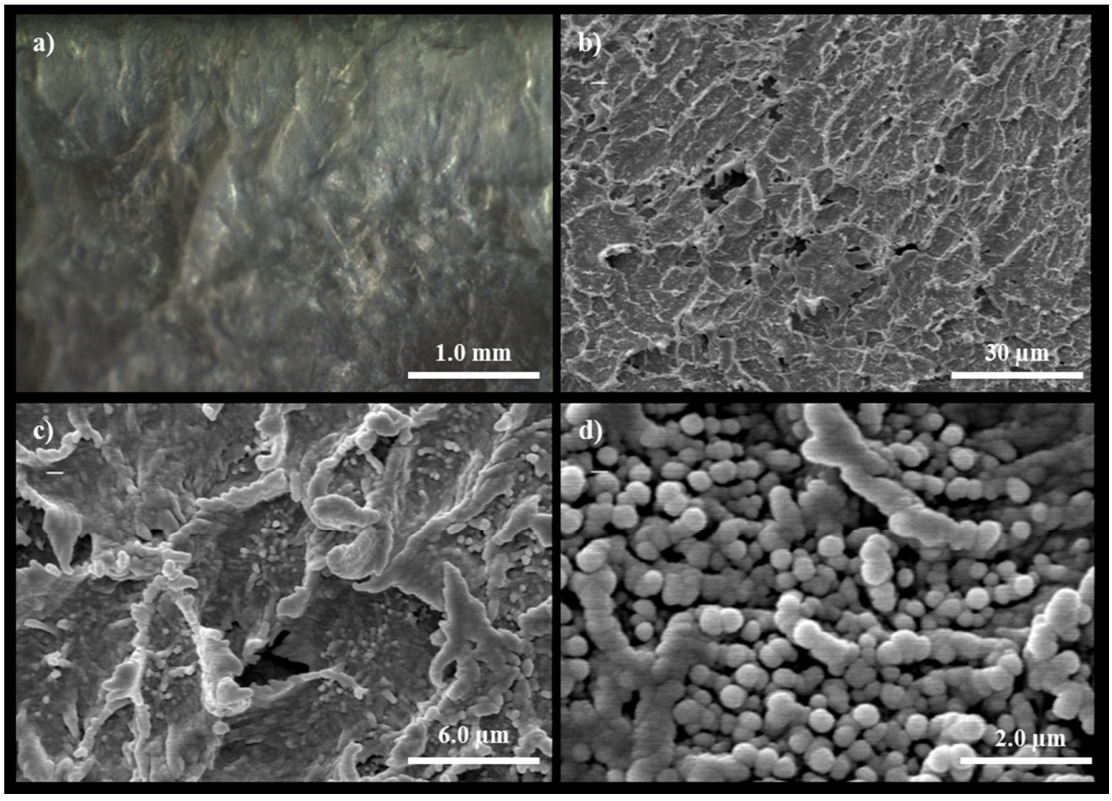

Figure 2.19 Micrographs of blank PLLA fracture surfaces after three point bending tests a) optical micrograph, b), c) and d) SEM micrographs, showing ductile deformation.

Figure 2.20 shows an optical micrograph of the fracture surface of each of the four bead containing groups, at each volume fraction. It must first be noted that the microbeads didn't once pull out of the PLLA matrix, instead shearing along the fracture plane. This indicates that the PLLA-microbead interface is stronger than the internal tensile strength of the microbeads themselves. It can be seen that the fracture patterns surrounding microbeads at the fracture plane did not show even and continuous signs of ductile deformation. Instead, two distinct regions of the fracture surface were observed.

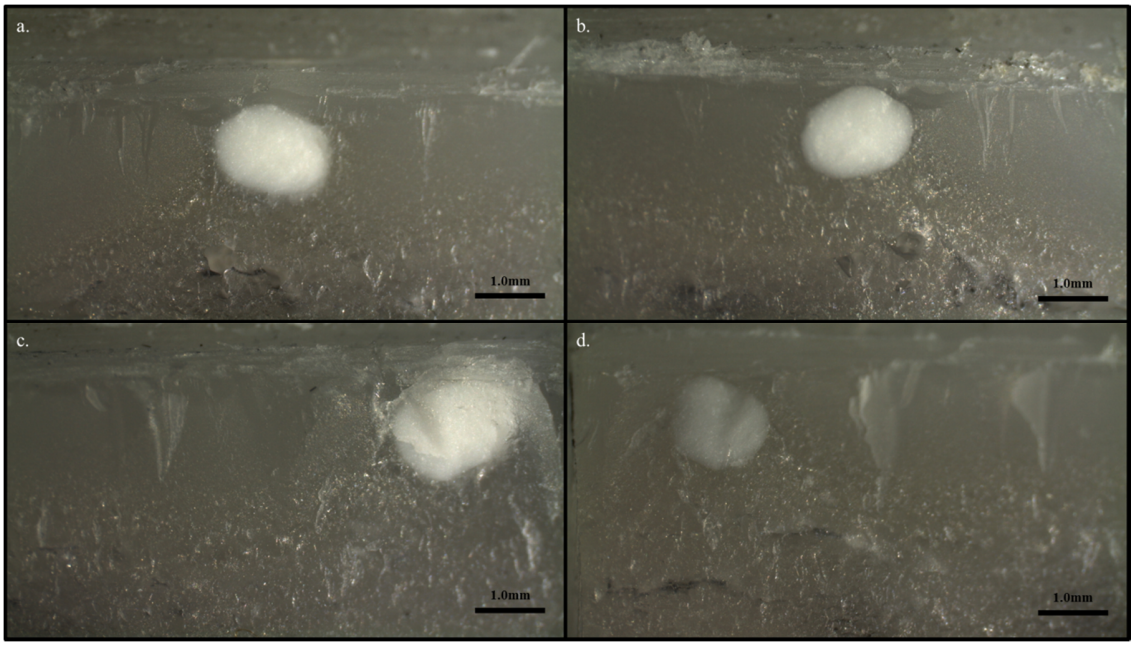

Figure 2.20 Optical micrographs of microbead containing PLLA fracture surfaces after three point bending tests of a) 2%, b) 5%, c) 9% and d) 11% microbead volume fraction specimens.

Firstly, the regions closest to the crack initiation site show no hackle formation, little crazing, and clean, smooth fracture surfaces. These indicate fast, brittle fractures occurring, with little material deformation. Figure 2.21 shows SEM micrographs of this region for a typical beaded specimen, in this case one of 2 %w/w microbead fraction. Light crazing was seen in Figures 2.21b and c. Furthermore, at the smallest scale shown in Figure 2.21d, fracture seems to have occurred through shearing along the plane of crack propagation, indicating a more brittle fracture.

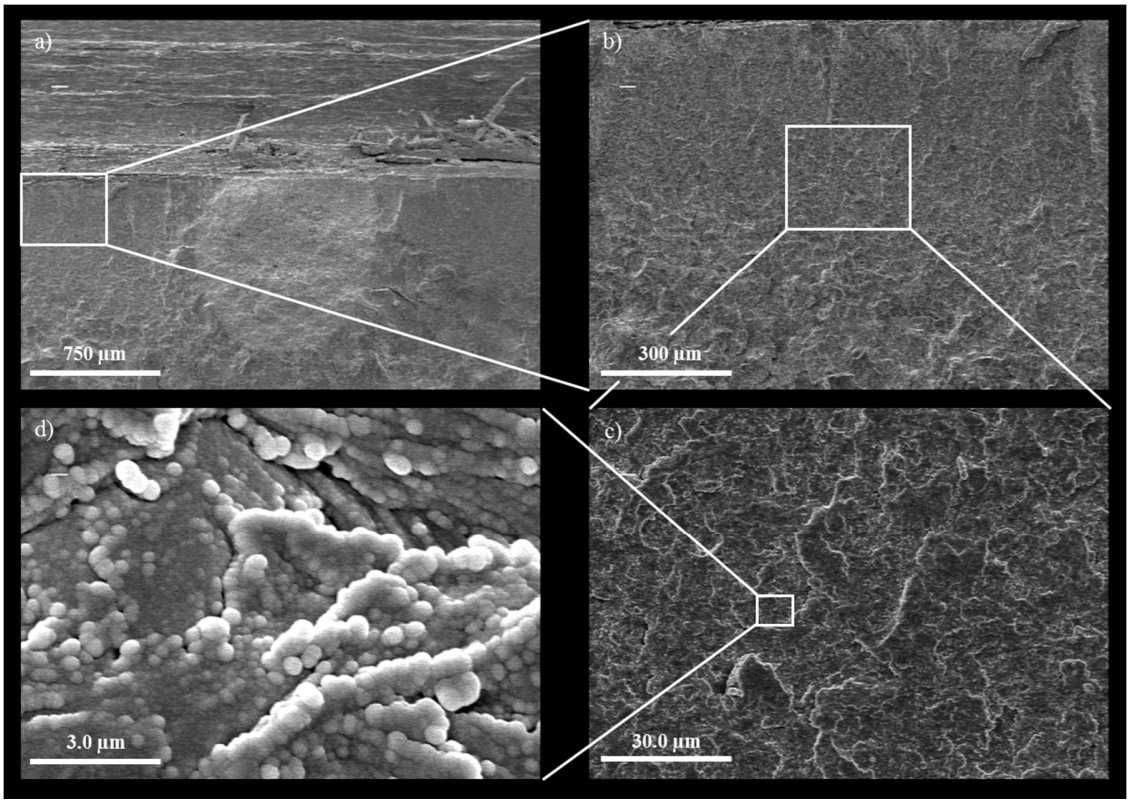

Figure 2.21 SEM micrographs focusing on the upper region of the fracture surface of a PLLA specimen containing 2%w/w microbeads.

The second region is the region furthest from the crack initiation site, below the bead, and showed crazing and a less smooth, more ductile fracture surface. Figure 2.22 shows SEM micrographs of this region of the same specimen over the same range of magnifications. In contrast to the upper region, it can be seen that strong hackle patterns formed as shown in Figure 2.22b, and Figure 2.22d shows that the PLLA material was deformed into short fibrils during fracture at the smallest scale. This fibrillation and patterning indicates strongly that a slower, more ductile fracture occurred here.

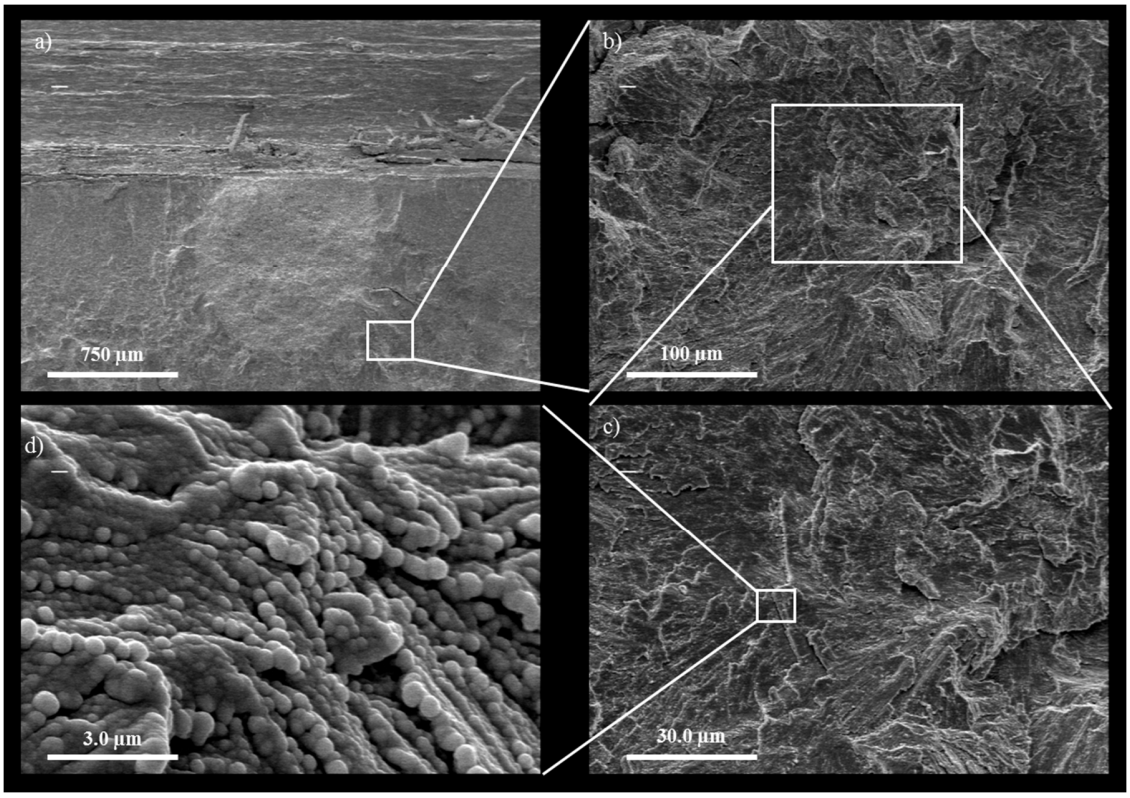

Figure 2.22 SEM micrographs focusing on the lower region of the fracture surface of a PLLA specimen containing 2%w/w microbeads.

The PLLA-microbead interface was also examined by SEM to determine whether poor cohesion may be the reason for the reduced fracture toughness of the material. Figure 2.23 shows the PLLA-microbead interface for a typical bead at the fracture surface, in this case a 5 vol% microbead fraction specimen. It can be seen that no voids or cracks are visible at the interface at all, and that in fact the materials seem very well bonded. The PLLA matrix has fully wetted the outer surface of the bead, and there are indications of polymer penetration into the bead's interior. This may be due to the pressure applied to the polymer bead mix during hot pressing, forcing the polymer to intrude upon the porous microbead.

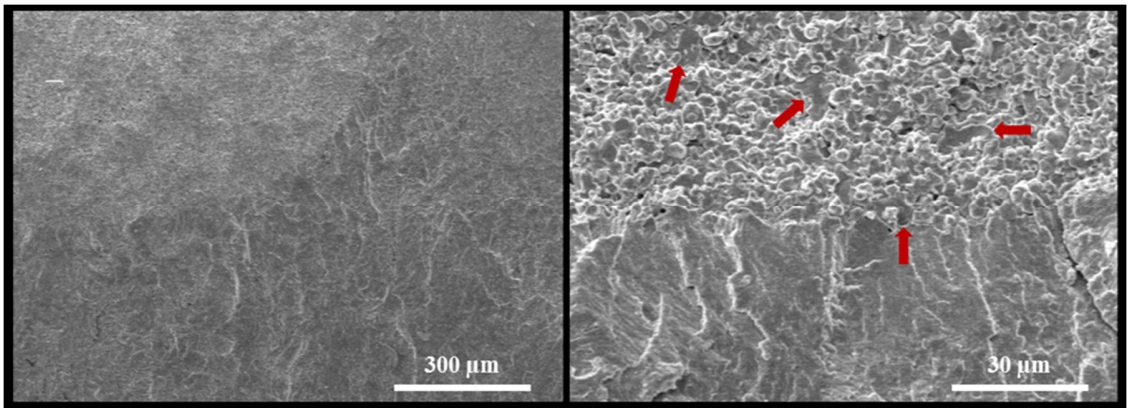

Figure 2.23 The PLLA/microbead interface on the fracture surface of a 5%w/w microbead containing specimen showing wetting and polymer intrusion.

To support this theory, EPMA was performed upon the same specimen. Figure 2.24 shows the same fracture surface under EPMA, with calcium concentrations measured in units of x-ray intensity. It can be seen that the Ca concentration in the microbead is highest at the centre, decreasing towards the edge. This indicates that the matrix may be intruding into the bead, due to its porosity and the application of pressure during the hot press fabrication process. All other embedded microbeads measured this way showed similar behaviour. This explains why the microbeads did not pull out of the matrix, instead shearing along the fracture plane. It also removes void formations at the polymer-bead interface as one mechanism to explain fracture.

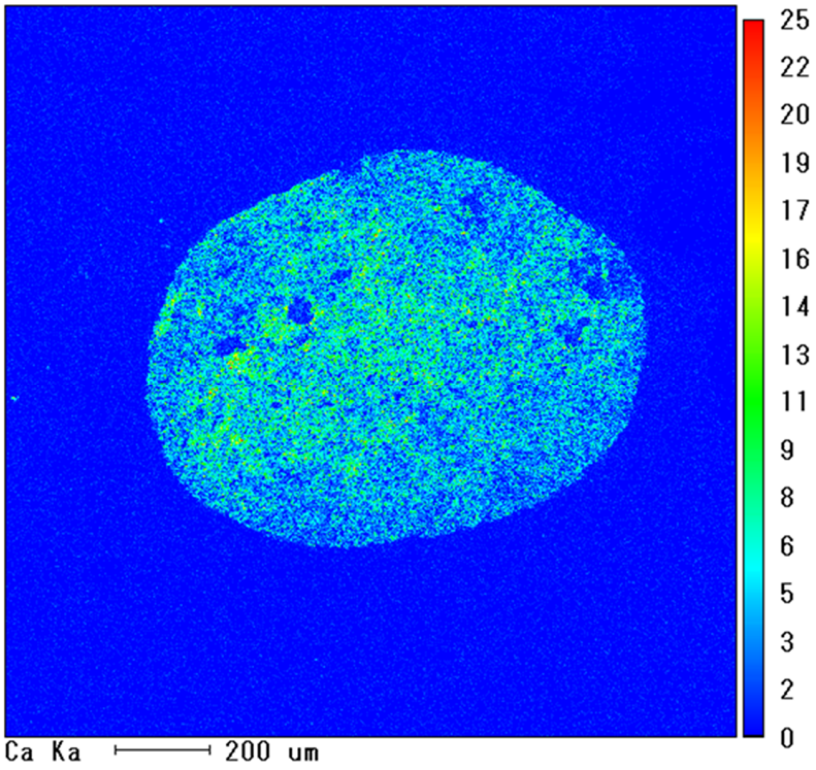

Figure 2.24 EPMA analysis of a 5%w/w microbead containing specimen of PLLA showing calcium elemental concentration.

2.4.2.4 Finite element analysis

Figure 2.25 shows the distribution of strain energy density (SED) along the fracture surface of each specimen calculated under linear elastic conditions after 0.4mm simulated displacement. Note that this face corresponds to the fracture surfaces observed earlier. The SED is increased greatly by the presence of the microbead, especially in PLLA surrounding the bead, in the region between beads, and the regions parallel to the bead, close to the crack initiation site. These regions of higher SED correspond very closely to the regions of brittle fracture observed on the fracture surface of beaded samples. Figure 2.26 shows the strain energy density calculated along the crack initiation site. Note that the SED clearly peaks at the precise locations where beads are present. Not only that, but the SED is also increases in the PLLA between bead locations, increasing by an amount inversely proportional to their distance apart. These two independent features are important in understanding the fracture behaviour of these materials.

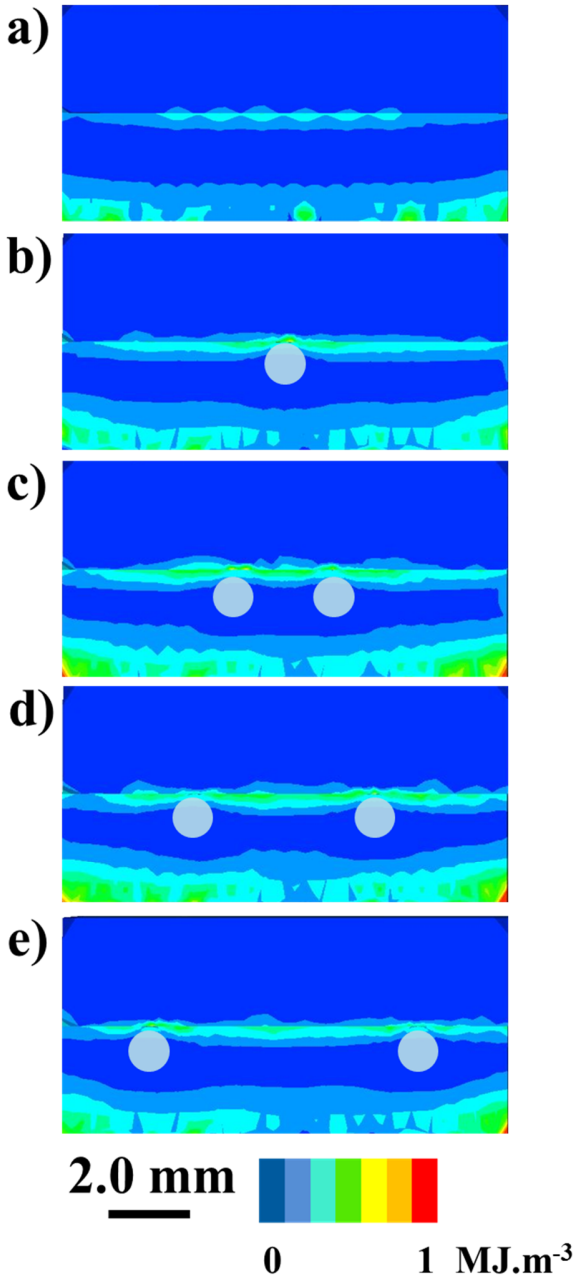

Figure 2.25 Strain energy density across fracture surfaces after simulated three point bending tests of a) blank PLLA, b) a single microbead containing specimen, c–e) two microbead containing specimens separated by a distance of 2 mm, 4 mm and 6 mm, respectively. Circles indicate bead locations. Calculated by finite element analysis.

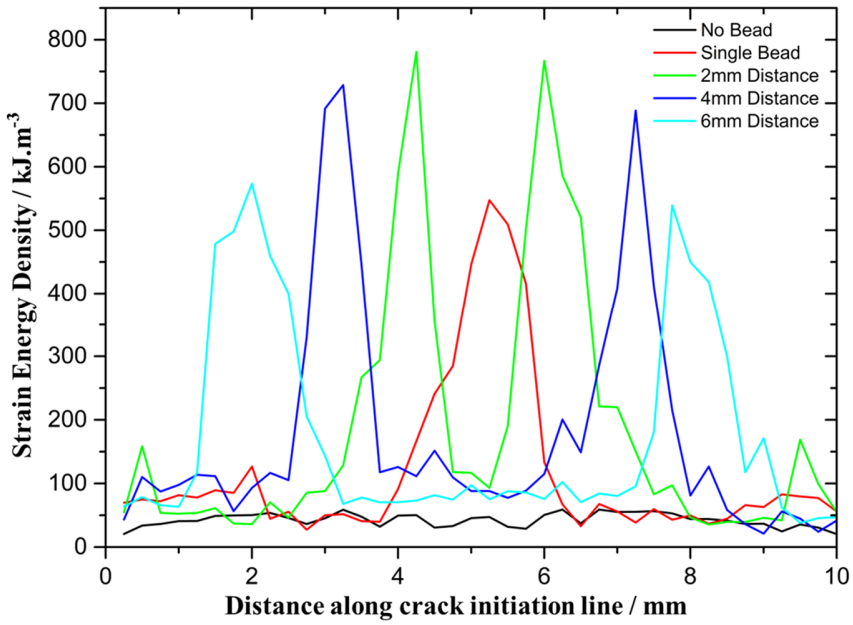

Figure 2.26 Strain energy density calculated by finite element analysis along the crack initiation site after simulated three point bending tests of each model.

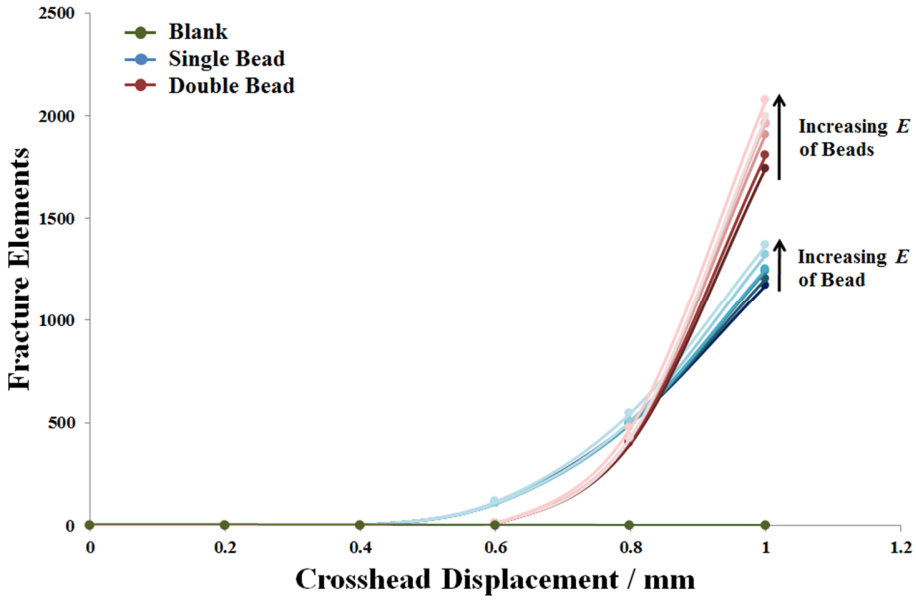

Figure 2.27 Fracture rates calculated by FE analysis. Comparison of blank PLLA, single, and double microbead containing PLLA, varying microbead stiffness of 5-50 GPa.

Analysis of the fracture rates of the PLLA model with and without microbeads was also enlightening. All of the basic models were compared; blank PLLA, PLLA containing a single microbead, and PLLA containing two microbeads at 6mm distance. Also, the stiffness of the microbeads in these simulations was varied between 5-50 GPa. The results are summarized in Figure 2.27, and full numerical results from this experiment can be found in Appendix A.2. Figure 2.28 shows the angle of view for Figures 2.29 and 2.30, which show the locations of tensile fracture elements in the bead containing models (50 GPa stiffness models pictured) as the load is applied.

Figures 2.27, 2.29 and 2.30 together offer several interesting insights. Firstly, Figure 2.27 shows that over a 1.0mm displacement, both the single and double beaded models underwent significant fracture, whereas the model without a microbead did not fracture at all. Secondly, it can be seen that for a given arrangement of microbeads, increased microbead stiffness leads to increased fracture rates.

Thirdly, the simulations showed that double beaded models fracture more easily than single beaded models. Figures 2.29a and b, and Figures 2.30a and b show that the first regions to fracture were along the interface between microbead and polymer matrix. This shows that the highest tensile stress concentrations were found here, indicating the reason for microbeads lowering overall fracture toughness of the material. Figures 2.29 and 2.30 also show that whilst the first elements which underwent tensile fracture were concentrated around the microbead/polymer interface, they were not limited only to these regions. Instead, although fracture was concentrated around the beads, microbead presence lead to fracture across the entire crack initiation line, focused on the region between the two beads when two beads were present. In Figure 2.29 this fracture region

expands in both directions, but in the double bead containing simulation of Figure 2.30, the crack expands preferentially into the region between beads, showing that the stress concentrations are not only increased along the microbead/ polymer interface, but also in the region of material between them.

These simulations therefore tell us that the increase in SED we saw in the earlier experiment shown in Figure 2.25 and 2.26 caused an increase in stress concentration at the microbead polymer interface, and did correlate with an increase in fracture rate. There was also a marked increase in fracture elements in the area between two microbeads, showing that the increase in stress concentrations under tension was not limited to only the microbead/polymer interface, but also the area of material between microbeads along the fracture initiation line. Our conjecture that this is the cause of the fracture seen in physical PLLA is thus further upheld.

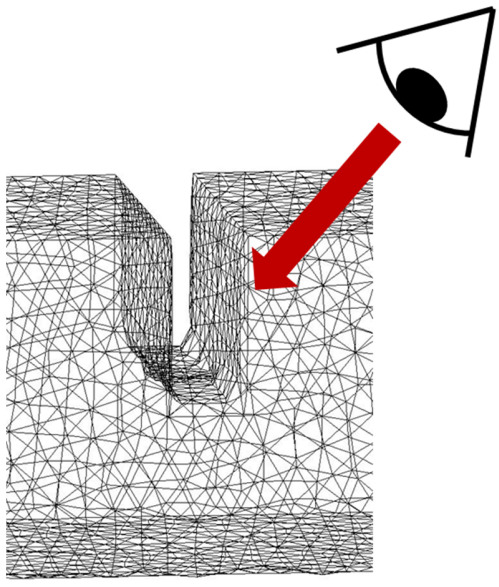

Figure 2.28 Angle of view for Figures 2.29 and 2.30, looking down at the notch tip region, from the front and slightly above.

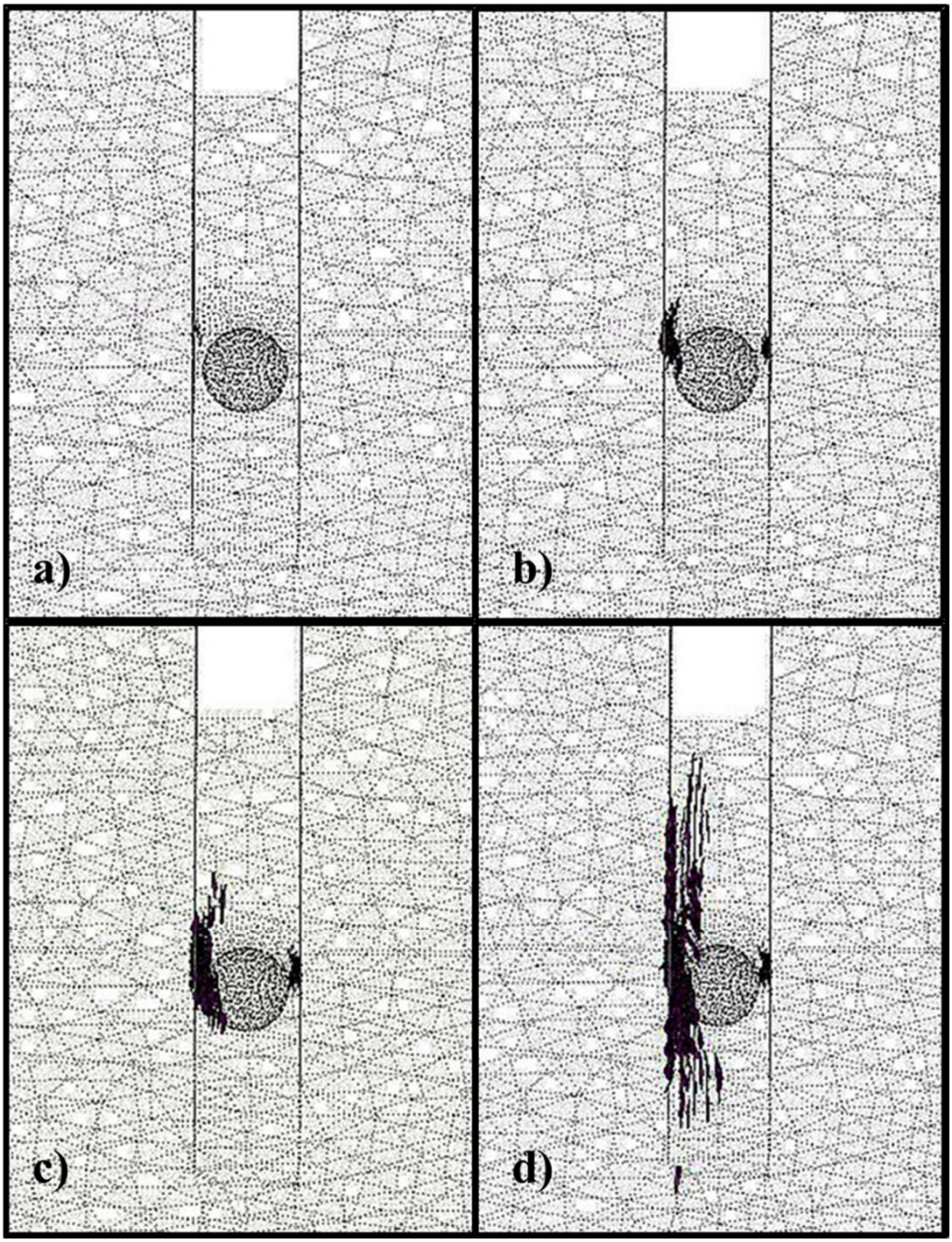

Figure 2.29 Location of fractured elements in single 50GPa stiffness beaded FE model after a) 0.4, b) 0.6, c) 0.8, and d) 1.0 mm simulated displacement. Black marks indicate tensile fractured elements.

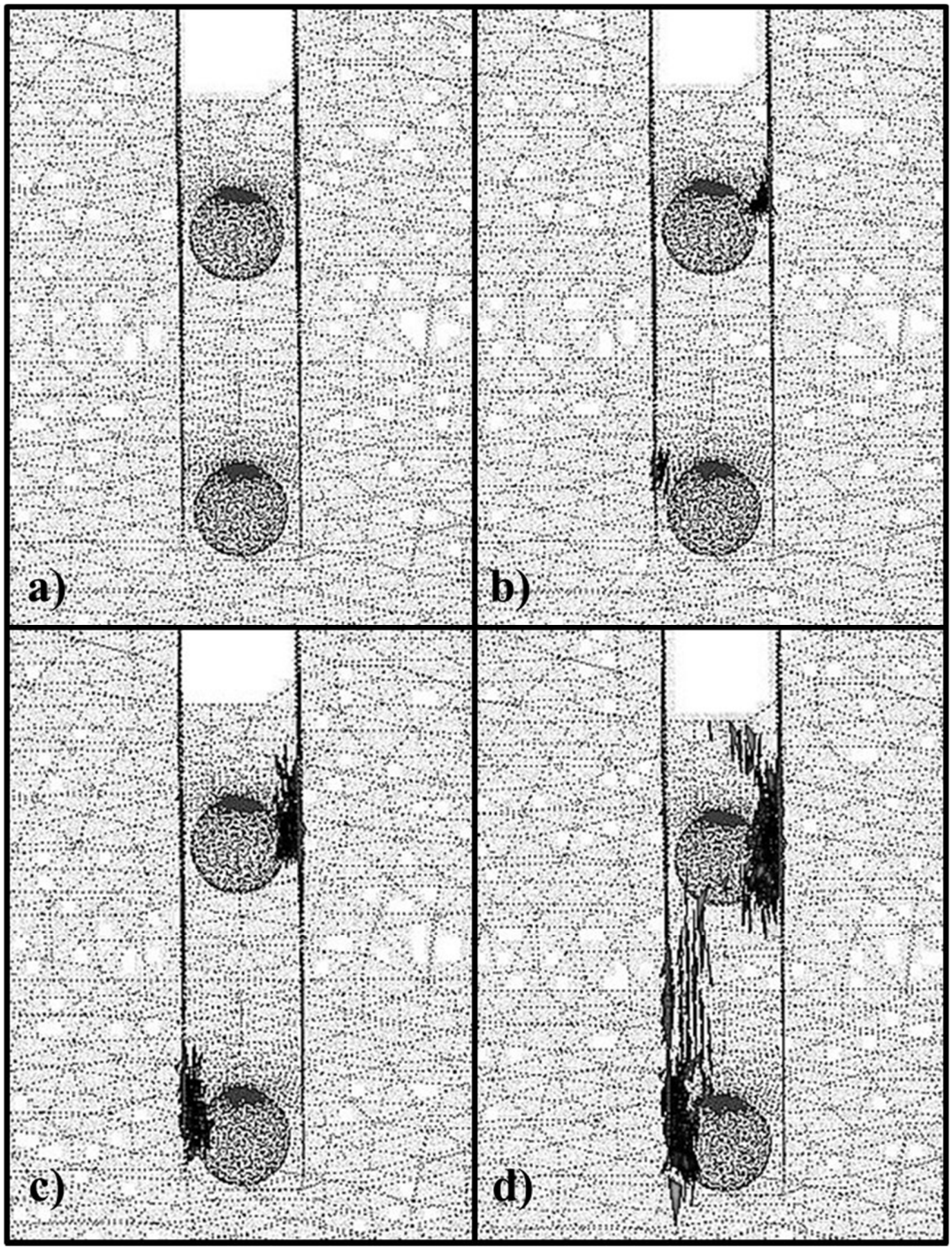

Figure 2.30 Location of fractured elements in double 50GPa stiffness, 6mm distant beaded FE model after a) 0.4, b) 0.6, c) 0.8, and d) 1.0 mm simulated displacement. Black marks indicate tensile fractured elements.

2.4.3 Microbead/ PCL composite

Calcium phosphate microbeads were successfully incorporated into PCL in concentrations matching the range outlined. Samples were prepared with 2, 5, 8 and 10% w/w concentrations, as well as blank PCL samples. Example load displacement curves obtained from three point bending tests for each group are shown in Figure 2.31. It can be seen that there was very little variation in the mechanical behaviour of each group, with similar initial gradients and P_{max} values across all PCL bead containing groups.

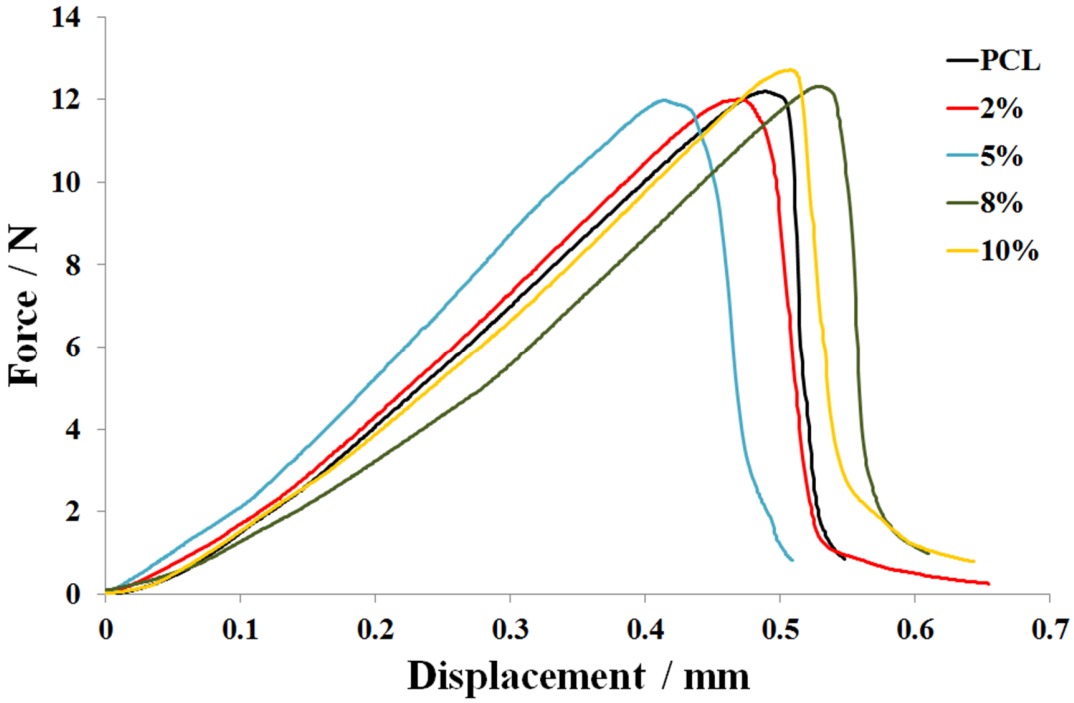

Figure 2.31 Load displacement curves obtained from three point bending tests, comparing mechanical behaviour of PCL with and without microbeads at all concentrations.

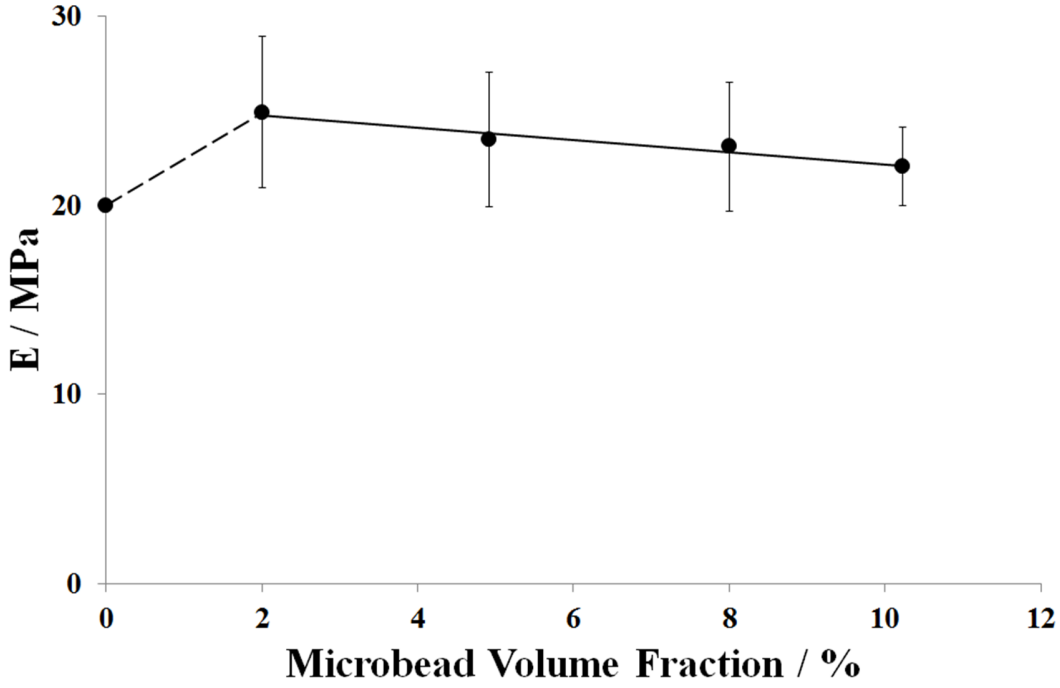

Figure 2.32 Young's modulus of PCL/microbead composite materials with respect to microbead concentration.

The Young's modulus, *E*, again did not vary across all concentrations, as shown in Figure 2.32. Any inclusion of microbeads caused only a slight increase in *E*, from 20 MPa to 24 MPa, which is within the expected range from literature [29]. This is promising, as a major benefit of PCL is its high flexibility, and the high stiffness of the calcium phosphate microbeads does not seem to have affected the material.

Calculations of K_{IC} and G_{in} were performed to determine whether microbead inclusion caused a change in fracture toughness of the material. As can be seen in Figures 2.33 and 2.34, the inclusion of microbeads into the polymer did not drastically alter the

fracture toughness of the materials at all. The average critical stress intensity factor was highest in the 10%w/w microbead concentration group, rising from 6.9 to 7.5 $Pa.m^{-1/2}$, though within error there is no noticeable change. The average critical strain energy release rate was within error unchanged despite any microbead inclusion, rising from an average of 2.55 Jm^{-2} for blank PCL to 2.63 Jm^{-2} for the 4%w/w group. This indicates strongly that the microbeads are not changing the fracture mechanism of the material at all.

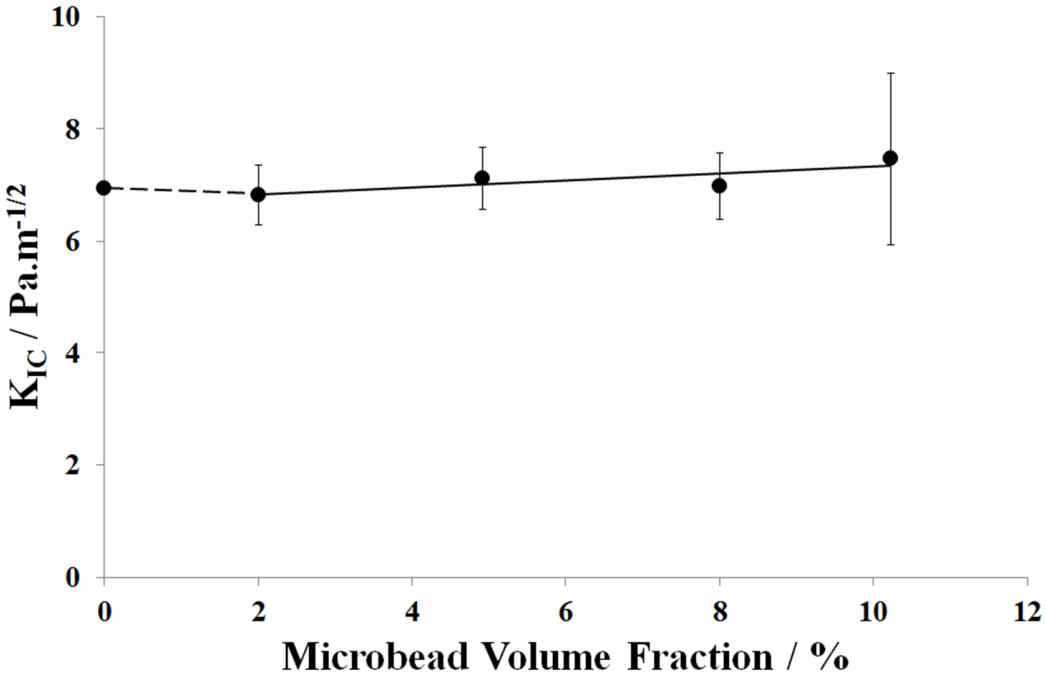

Figure 2.33 K_{IC} as a measure of fracture toughness of PCL/microbead composite materials with respect to microbead concentration.

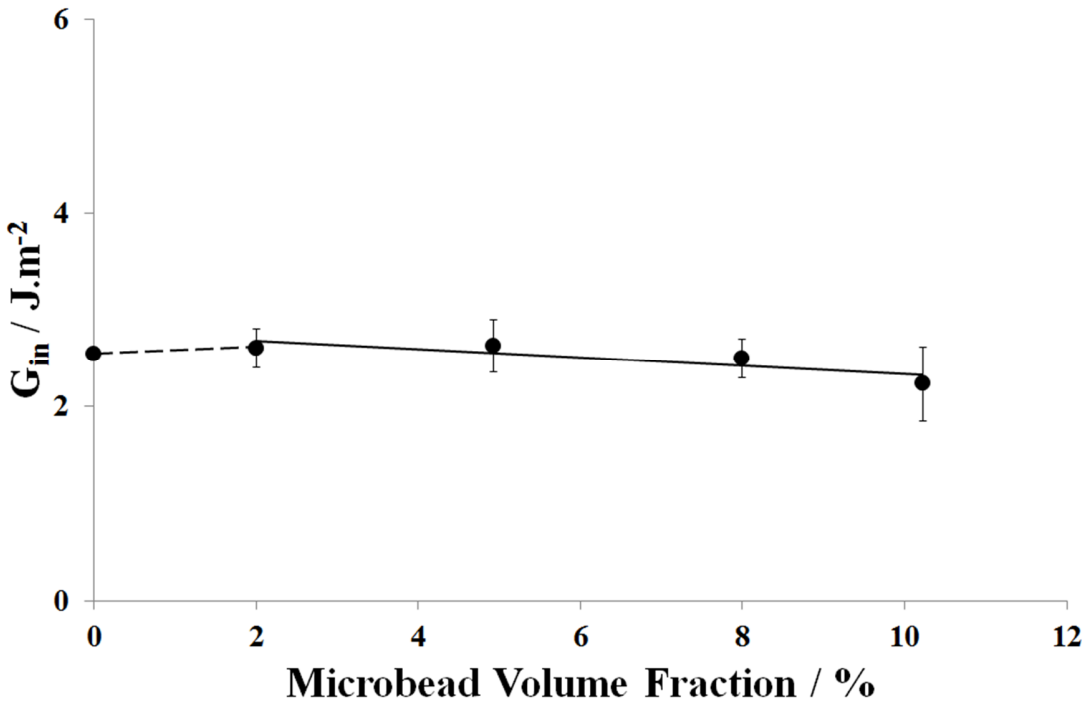

Figure 2.34 G_{in} as a measure of fracture toughness of PCL/microbead composite materials with respect to microbead concentration.

By looking at the fracture surfaces of PCL with and without microbead inclusion, we can confirm that indeed, there seems to be a consistent fracture mechanic occurring across all groups. Figure 2.35 shows the fracture surface of PCL with no microbead inclusion, and Figure 2.36 shows the fracture surface of the 2%w/w group. The hackle pattern is far more pronounced on the larger scales on the blank PCL, however they are present on all specimens. At smaller scales, the fracture surfaces begin to look more alike, with strong crazing visible with the SEM. At the smallest scales, all specimens show the same kind of deformation, as the polymer material was pulled parallel to the direction of travel of the crack front creating ridges and lines and some small fibrils. This pattern suggests that all specimens underwent ductile deformation, and that the crack

propagated through the material at a slow rate. The interface between bead and polymer can be seen in Figure 2.36. It is clear that no polymer has intruded into the microbead, however the PCL seems to have fully wetted the surface of the bead and no large voids or gaps can be seen.

Figure 2.37 shows an optical micrograph of the fracture surface of each of the four bead containing groups, at each volume fraction, to show the lack of variation across each group. Unlike with PLLA, the microbeads did seem to pull out of the polymer matrix instead of cleaving parallel to the crack front, indicating no polymer intrusion and no strong bonding between polymer and microbead surfaces. This is possibly why there was no perceived change in flexibility in the material, as all stress seems to be passing through the polymer matrix, not the beads.

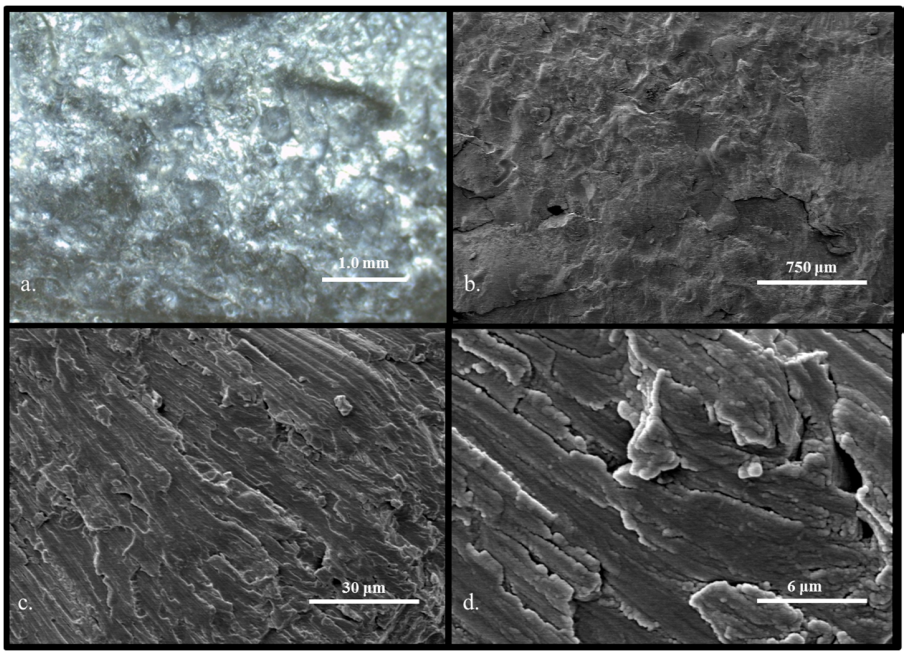

Figure 2.35 Micrographs of blank PCL fracture surfaces after three point bending tests a) optical micrograph, b), c) and d) SEM micrographs, showing ductile deformation.

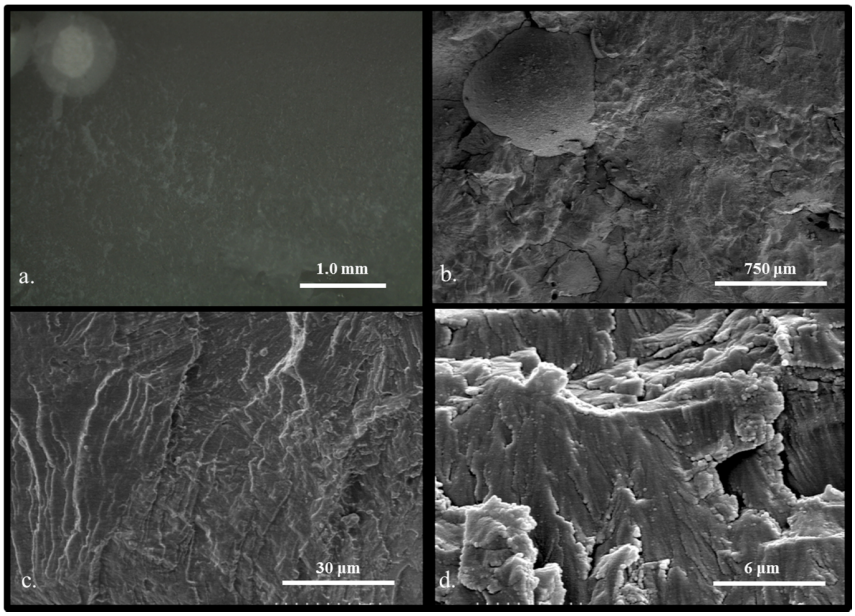

Figure 2.36 a) Optical and b, c, d) SEM micrographs of the fracture surface of a PCL specimen containing 2%w/w microbeads, showing ductile deformation.

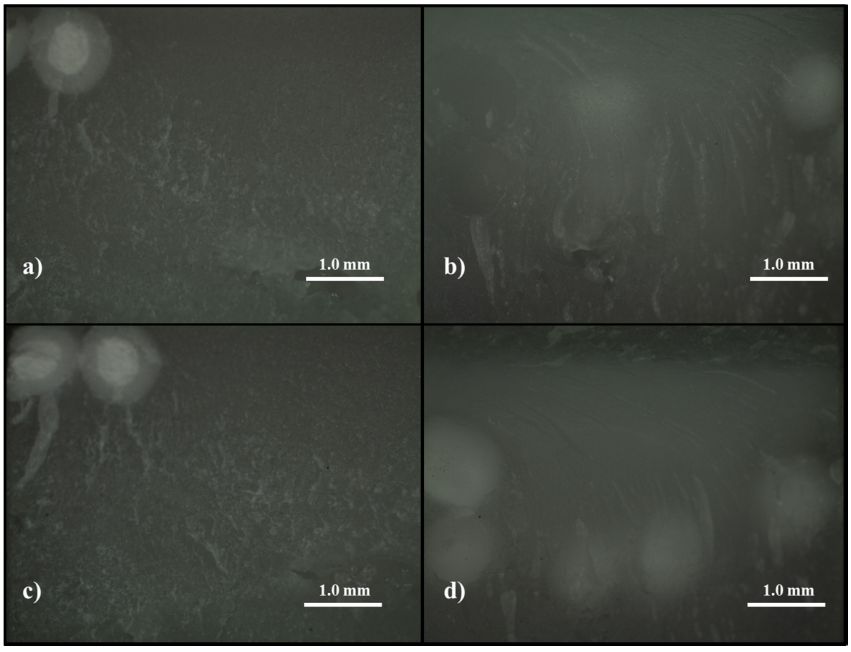

Figure 2.37 Optical micrographs of microbead containing PCL fracture surfaces after three point bending tests of a) 2%, b) 5%, c) 8% and d) 10% microbead volume fractions.

2.4.4 Microbead/ PLLA/ PCL composite

PLLA and PCL were successfully combined by precipitating dissolved polymer out of dichloromethane using distilled water. Figure 2.38 shows SEM micrographs of the blended material before further fabrication. The images show that no visible phase boundaries are present, and as such it can be concluded that the polymers were miscible and have blended fully. The only other visible features are small voids, formed most likely by the expulsion of dichloromethane during the precipitation process.

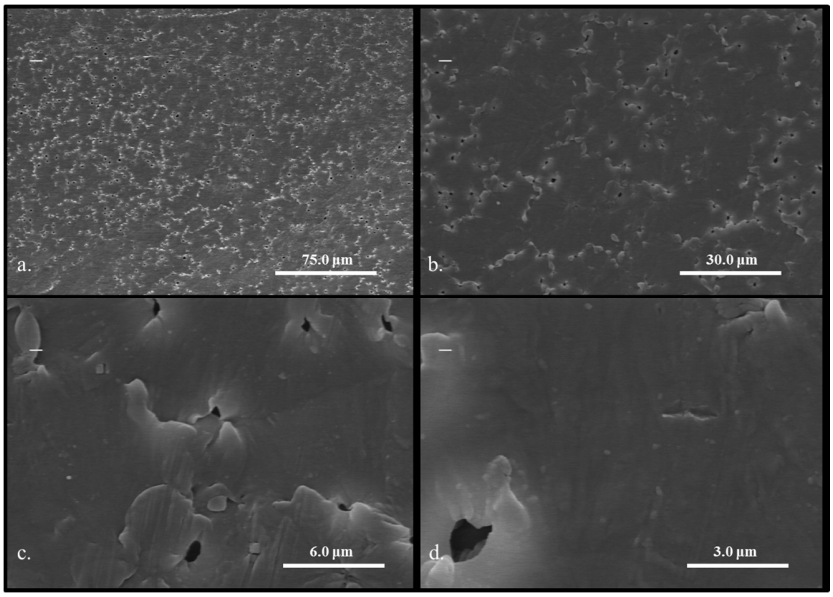

Figure 2.38 SEM micrographs of PLLA/PCL blended polymer showing no phase separation and small voids from dichloromethane outgassing.

Calcium phosphate microbeads were successfully incorporated into the PLLA/PCL mix, in concentrations matching the range outlined. Samples were prepared with 2, 5, 9 and 11% w/w concentrations, as well as blank samples. Example load

displacement curves obtained through three point bending tests are shown in Figure 2.39. Interestingly, all groups showed a similar ductile form of fracture in their curves, indicating a different fracture mechanic for bead containing specimens of the blended polymer from that of PLLA. Unlike in PCL however, increasing microbead concentration did seem to have a strong effect on the fracture toughness of the material, lowering P_{max} considerably as concentration increased.

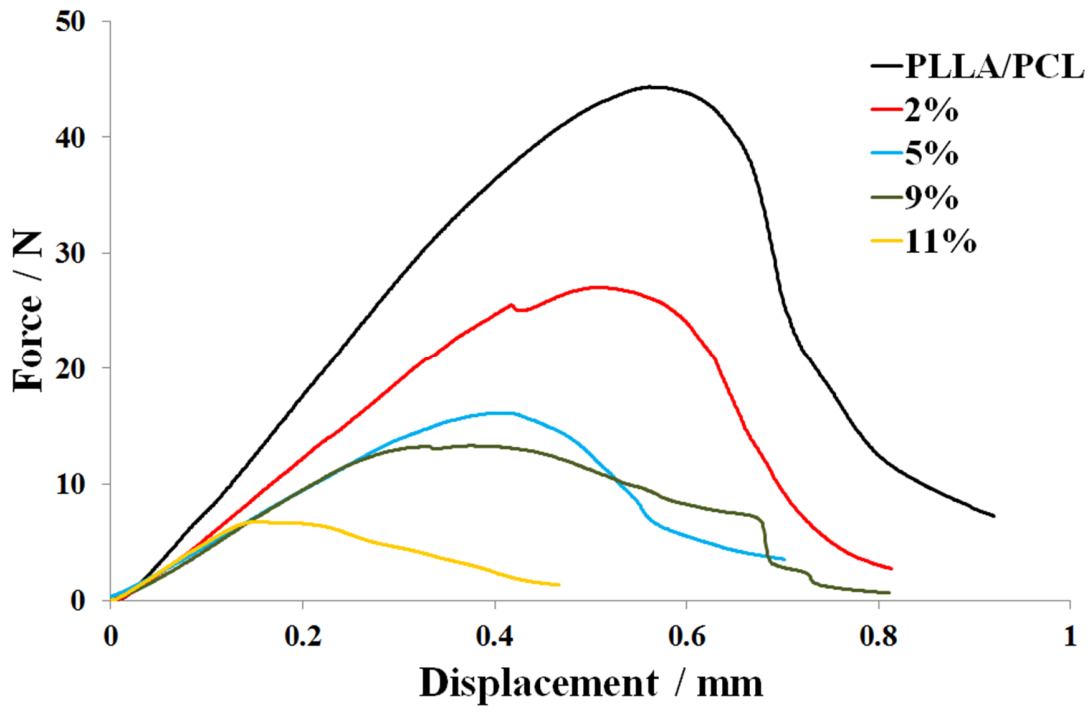

Figure 2.39 Load displacement curves obtained from three point bending tests, comparing mechanical behaviour of the PLLA/PCL polymer blend with and without microbeads at all concentrations.

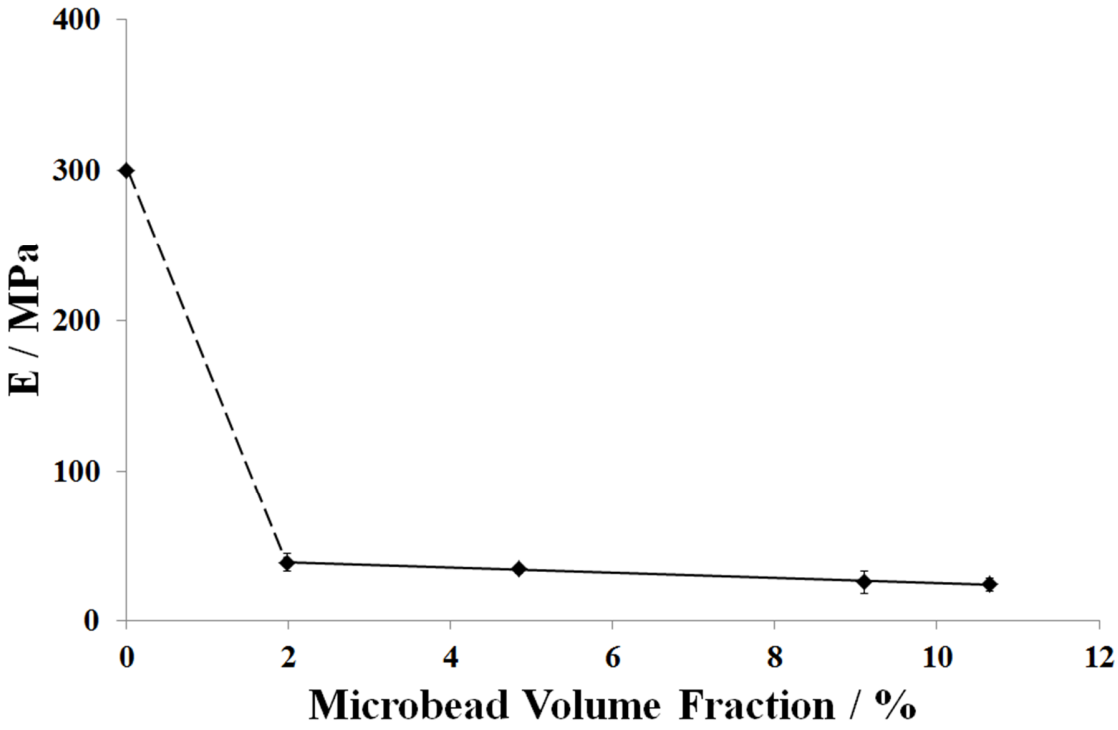

Figure 2.40 Young's modulus of blended polymer/microbead composite materials with respect to microbead concentration.

As can be seen in Figure 2.40, the Young's modulus, *E*, varied in a way unlike PLLA or PCL, as any inclusion of microbeads caused a sudden drop in stiffness. The blank blend had stiffness between that of PLLA and PCL, of 300 MPa, but an inclusion of 2%w/w microbeads caused a sudden decrease in modulus to 38 MPa. With increasing microbead inclusion, the stiffness dropped even further, until at 11%w/w microbead concentration the Young's modulus was measured to be 24 MPa.

K_{IC} and G_{in} were also calculated in order to determine whether microbead inclusion caused a change in fracture toughness of the material more similar to that of PLLA or PCL. As can be seen in Figures 2.41 and 2.42, the inclusion of microbeads into the polymer did indeed affect the fracture toughness of the blended material, in a manner similar to PLLA.

Blank blended polymer had a K_{IC} of 25 $Pa.m^{-1/2}$ and a G_{in} of 20.6 Jm^{-2}, comparable to the values of blank PLA. However, as with PLLA, even the smallest concentration of microbeads, 2%w/w, caused a sharp decrease in fracture toughness. The K_{IC} of 2%w/w microbead sample was 16.0 $Pa.m^{-1/2}$ and the G_{in} was 9.6 Jm^{-2}. With increasing concentration of microbeads, both K_{IC} and G_{in} continued to fall, decreasing linearly until at 11%w/w microbead concentration the values are 3.9 $Pa.m^{-1/2}$ and 1.5 Jm^{-2} respectively. This indicates that the microbeads are possibly causing a change in the fracture mechanism.

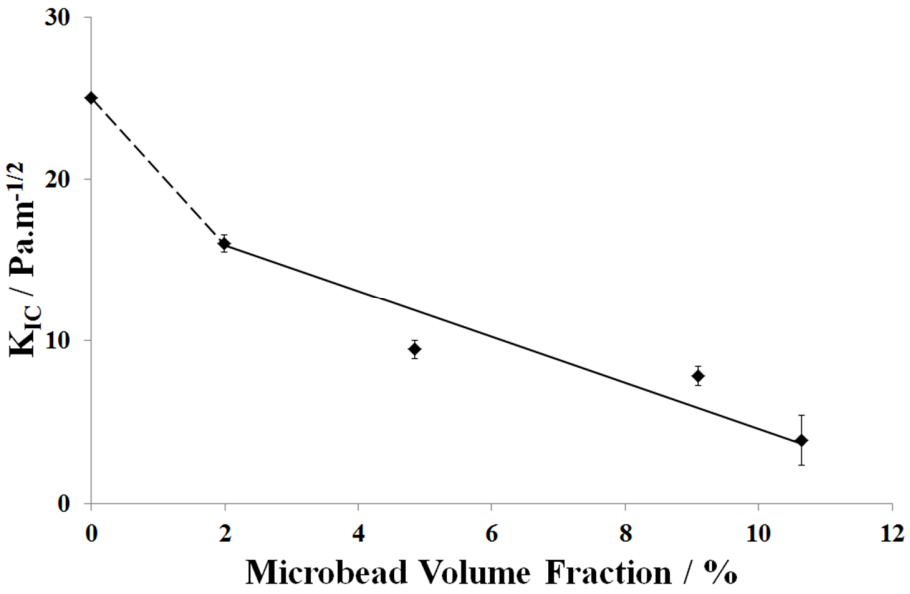

Figure 2.41 K_{IC} as a measure of fracture toughness of blended polymer/microbead composite materials with respect to microbead concentration.

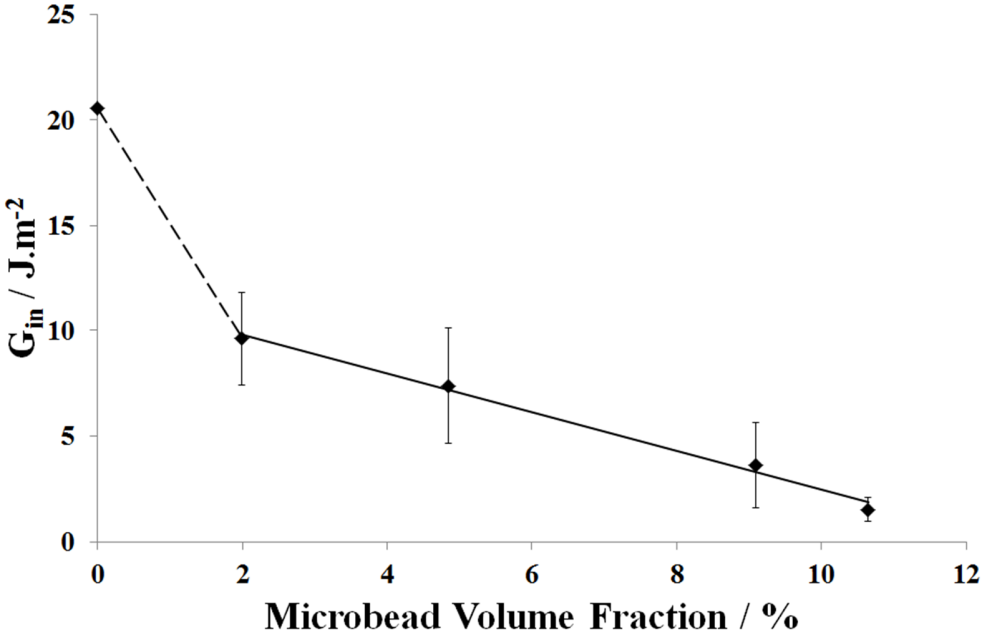

Figure 2.42 G_{in} as a measure of fracture toughness of blended polymer/microbead composite materials with respect to microbead concentration.

Again, we can look at the fracture surfaces of the blended biopolymer with and without microbead inclusion to investigate the fracture mechanic which was present in each group. Figures 2.43 and 2.44 show the fracture surfaces without microbeads and with 2%w/w microbead volume respectively. As can be seen, the fracture patterns do not seem very different between the two specimens. Both show strong crazing patterns at all scales, and both show ductile deformation of material at the smallest scales. This is in line with all groups undergoing a low energy, ductile fracture, creating microscopic features such as ridges aligned with the direction of crack propagation, fibrils and void formation.

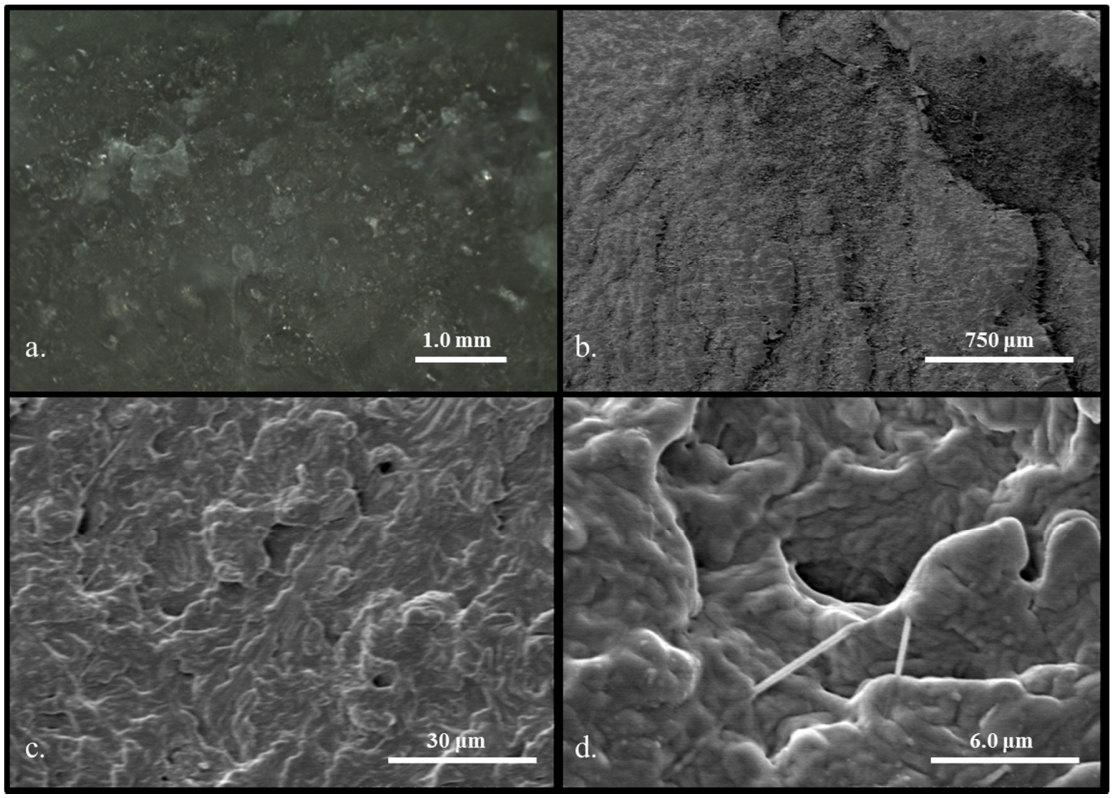

Figure 2.43 Micrographs of the fracture surface of blended polymer showing ductile deformation a) optical micrograph, b), c) and d) SEM micrographs.

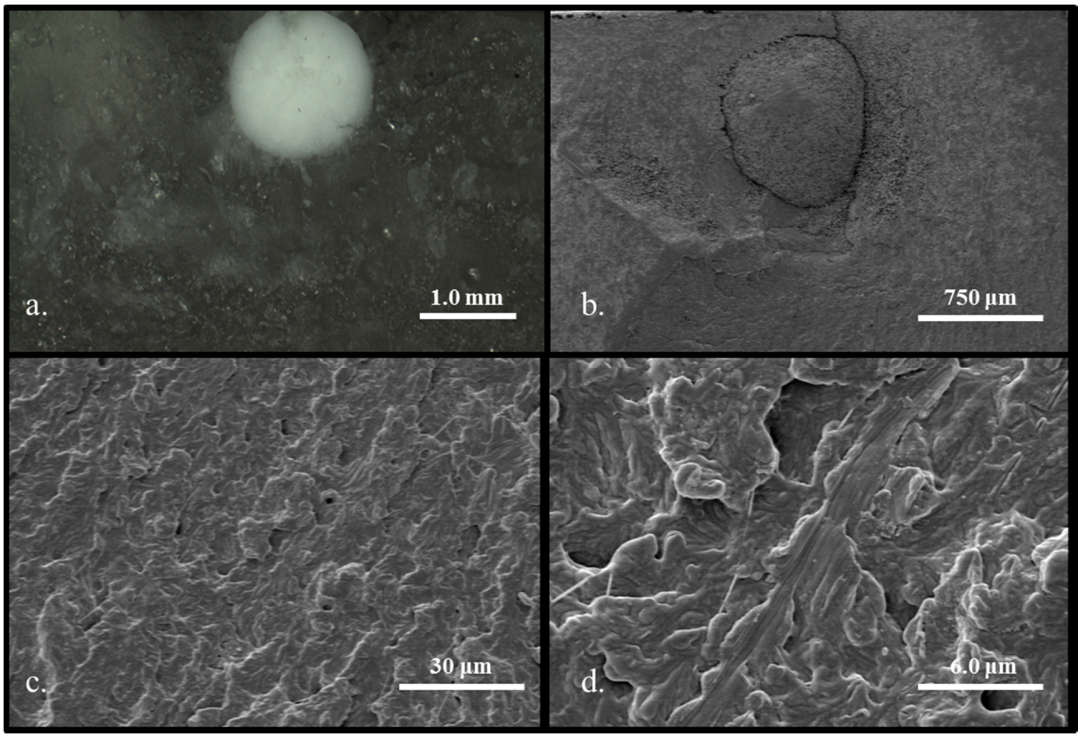

Figure 2.44 Micrographs of the fracture surface of blended polymer containing 2%w/w microbeads showing ductile deformation a) optical micrograph, b), c) and d) SEM micrographs.

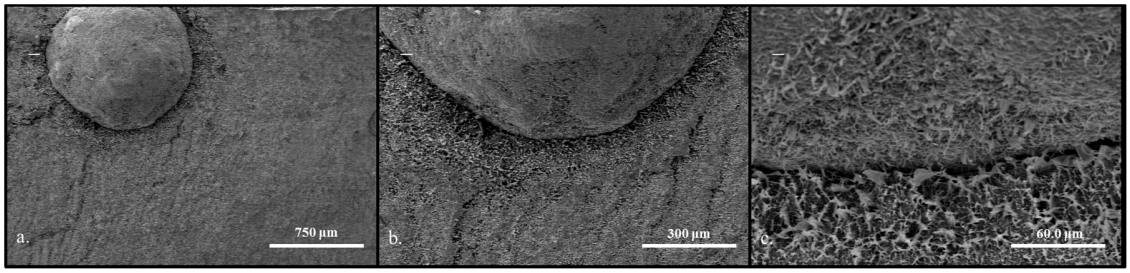

Figure 2.45 SEM micrographs of the blended polymer/microbead interface of a 5%w/w microbead containing specimen.

This is unexpected, as the fracture toughness for microbead containing groups was significantly lowered. However, one clear difference between the fracture surfaces of

PLLA and the blend stands out; the polymer interaction with the ceramic microbead. As can be seen in Figure 2.44 and more clearly in SEM images of a second beaded sample from the same microbead concentration group, Figure 2.45, there is a clear and distinct boundary between the biopolymer matrix and the microbead. This could explain the reduced fracture toughness of the material by causing larger voids more frequently in the polymer matrix.

Figure 2.46 shows an optical micrograph of the fracture surface of each of the four bead containing groups, at each volume fraction, to confirm that each microbead containing sample fractured in a similar way. The only major difference is the level of crazing which occurs, with the 11%w/w concentration sample fracturing very easily and creating a very distinct, ductile hackle pattern.

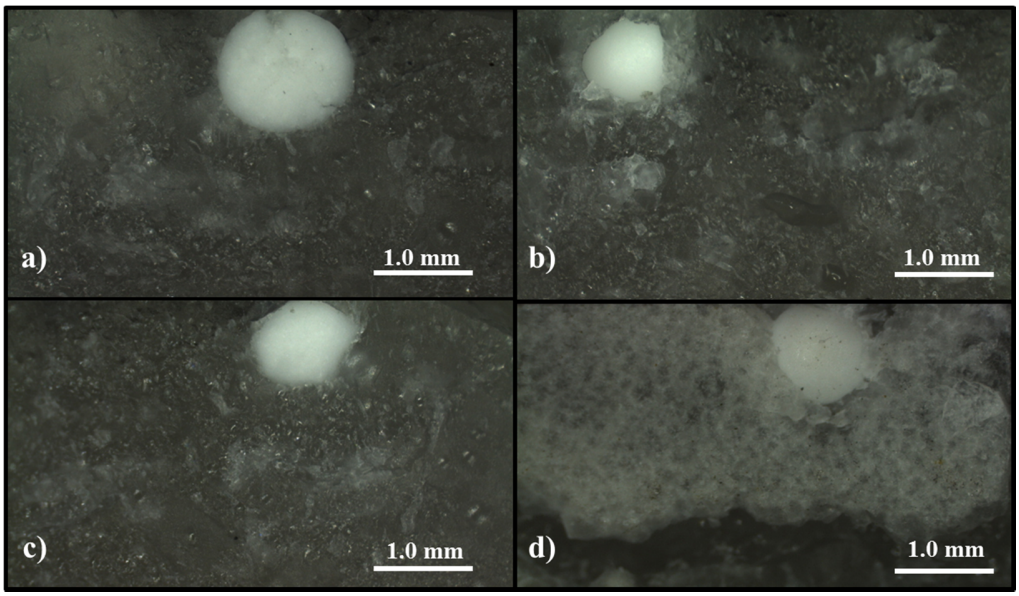

Figure 2.46 Optical micrographs of microbead containing blended polymer fracture surfaces after three point bending tests of a) 2%, b) 5%, c) 9% and d) 11% microbead volume fraction specimens.

2.4.5 Comparison of three composites

Firstly, the mechanical properties of each material can be compared, in order to see which dealt best with the inclusion of calcium phosphate microbeads. Figures 2.47, 2.48 and 2.49 show the values for E, K_{IC} and G_{in} respectively for each material. Note that the comparisons of E and G_{in} are made on logarithmic scales to include the wide range of values measured for each material.

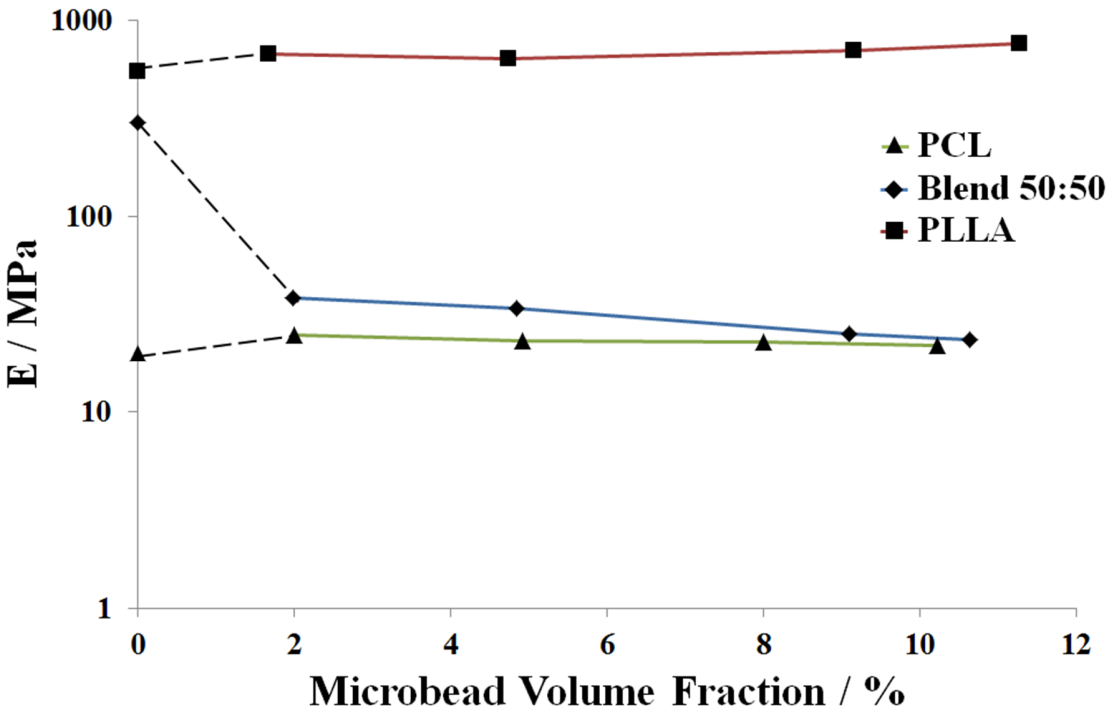

Figure 2.47 Comparison of Young's modulus for each material with varying microbead volume fraction.

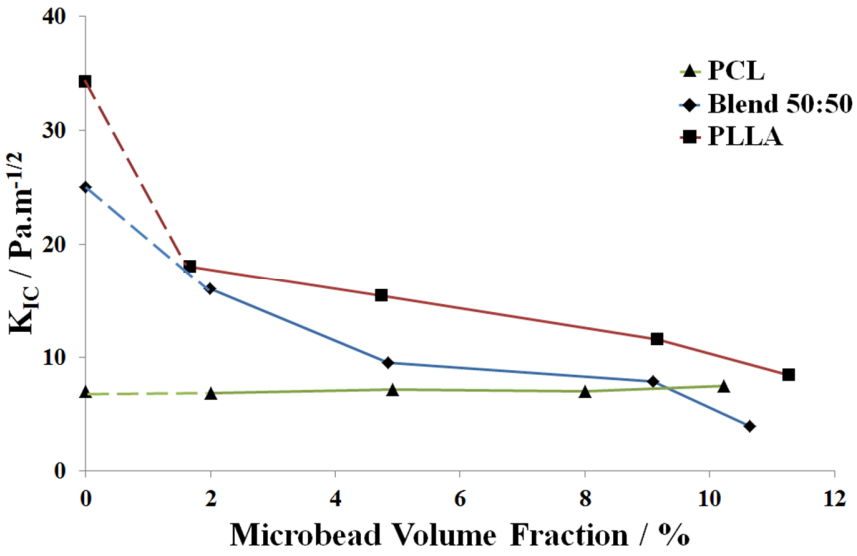

Figure 2.48 Comparison of K_{IC} as a measure of fracture toughness for each material with varying microbead volume fraction.

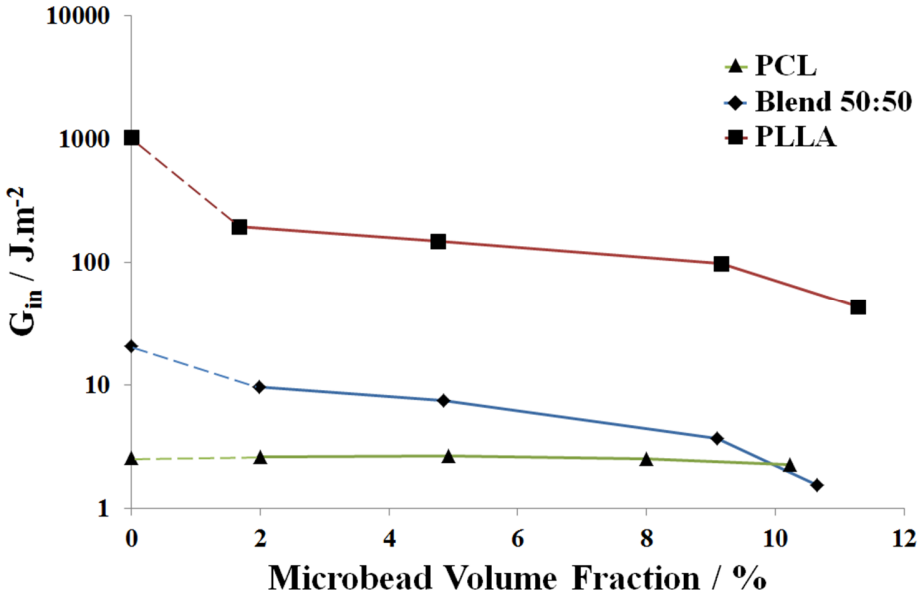

Figure 2.49 Comparison of G_{in} as a measure of fracture toughness for each material with varying microbead volume fraction.

It can be seen that PCL was the only material which successfully incorporated microbeads into its structure without any significant changes in material properties. All measured and calculated values stayed constant from 0-10%w/w microbead inclusion. PLLA and the 50:50 blended polymer by contrast saw a significant change in both measures of fracture toughness caused by the inclusion of beads. By looking at the fracture surfaces of each of the materials we can explain most of this behaviour; however the exact mechanism for why the stiffness of the PLLA/PCL blend reduced is unknown.

PLLA saw polymer intrusion into the microbeads, and so fractures cleaved the ceramics along the plane of crack propagation rather than pulling out. The fracture surfaces showed that this lead to two regions of different fracture type within the PLLA; an upper region above the bead of fast, brittle fracture, and a lower region below the bead, where the crack slowed down and caused ductile fracture. This hypothesis was confirmed using FE analysis to study SED within the material during fracture. It also helped show that the increasing concentration of microbeads increases average SED across the crack region, explaining the further decrease in fracture toughness as concentrations increased.

PCL saw microbeads pulling out of the polymer matrix rather than cleaving, indicating no intrusion or strong bonding at the polymer microbead interface. The fracture surfaces of PCL without microbeads showed the same features of ductile fracture that PCL with microbeads showed. At the smallest scales, the pulling and deforming of the PCL material into ridges and fibrils was almost identical across all groups.

The PLLA/PCL 50:50 blended polymer showed ductile deformation similar to that seen in both the lower region of the PLLA and all of the PCL samples. The blended polymer did not show the distinct separate regions of differing fracture type seen in PLLA and also did not intrude upon the microbeads, forming instead a distinct boundary layer between the material and the bead. It is uncertain how this layer affects the overall fracture toughness of the material; however the large regions of poorly bonded polymer, and the voids formed might explain the reduced fracture toughness of the blended polymer as microbead concentrations increased.

2.5 Conclusions

In conclusion, the biopolymer/bioceramic microbead composite was successfully fabricated. Bioceramic microbead production was investigated and optimized, and their inclusion into three kinds of biopolymer matrix was successfully completed. These three novel materials were then investigated and characterized with varying concentrations of microbeads in order to determine their change in material properties. Three point bending tests were performed, as they are critically important for investigating the bending properties of the materials, properties which are under-reported in the literature yet must be known for bone plate applications.

Microbead inclusion caused a slight increase in stiffness for PLLA and PCL, but instead a sharp decrease in stiffness for the blend. Fracture toughness as measured by K_{IC} slightly decreased for the PLLA and blended polymer with microbead inclusion, however for PCL the value of K_{IC} barely changed at all. Measuring fracture toughness by G_{in} showed again, that PLLA and the blended polymer were reduced, this time by a much greater proportion. For PCL again, this value barely changed.

The mechanism of fracture of each material was investigated using fracture surface analysis, load displacement curves, SEM, EPMA and finite element analysis. The mechanism of fracture was shown to have changed between materials distinctly due to the inclusion of microbeads. Without microbeads, all materials fractured in a ductile manner. Once microbeads were added, PLLA fractured by a two phase mechanism of brittle fracture followed by ductile in a manner confirmed through FE analysis of strain

energy density and fracture analysis. FE analysis also showed that the tensile stress concentration was greatly raised at the microbead/polymer interface, leading to the initial fractures always originating from this region, and expanding outwards from there. This is a key to explaining why PLLA saw such a marked reduction in fracture toughness once microbeads were added.

Intrusion into the microbead was also seen for PLLA, causing microbeads to cleave during fracture. In PCL and the blended polymer, microbeads pulled out during fracture as the polymer did not intrude upon them. Both showed only ductile fracture still after microbead inclusion; however the blended polymer formed a boundary layer between polymer and microbead, unseen in PCL.

The only existing study into spherical calcium phosphate particles in a PLLA matrix was by Todo *et al.*, as referenced in Chapter 1.2.5. This study showed similar reduced fracture toughness as measured by G_{in} and the transition from ductile to brittle facture when beads were introduced [76]. However, the effects of inclusion into PLLA and a blended polymer are unreported in the literature. As discussed, older studies focus firmly on compressive testing, such as Kane *et al.*, and newer studies whilst also focusing on compressive testing, also only investigate calcium phosphate filler materials which are suitable for 3D printing [72-75]. Materials of more bespoke geometry are under-reported, especially in the bending mode, and this is why the results of this new study are so useful and important.

Overall, this research shows that inclusion of microbeads into biopolymers is a promising avenue for research. By understanding the difference in mechanisms of

fracture caused in different materials, we can understand which might be used to improve in the future. The intrusion of PLLA into the microbeads was unexpected, and its unusual fracture profile may provide insight for improving future materials further. PCL performed remarkably well, and inclusion of calcium phosphate microbeads into existing PCL applications is a very promising way to apply this research immediately if desired.

CHAPTER 3: PLCL FIBRE / CALCIUM PHOSPHATE COMPOSITES

3.1 Overview

In order to improve the flexibility and bioactivity of a dicalcium phosphate dihydrate ceramic for use in kyphoplasty surgery, PLCL fibres are added. The average length of fibres is investigated, in order to determine the effects on material properties. Compressive strength and compressive elastic modulus were measured. Longer fibres were seen to create weaker but more flexible composites than shorter fibres at equal concentrations. The reasons for this effect were investigated using microscale computed tomography (micro-CT scans), SEM and XRD.

3.2 Materials and fabrication methods

3.2.1 Fabrication of PLCL fibres

PLCL fibres were formed using the melt-spinning method. A commercial melt-spinning machine, more commonly sold as a cotton candy making machine, is used to create the PLCL fibres. This method has been proven to be a cost effective, quick and reliable way to fabricate biopolymer fibres for biomedical applications in the past. In 2010, Chung *et al.* used a custom set up which closely resembled a cotton candy maker in order to produce fibres of the biopolymer PLCL by heating the polymer pellets to 155°C under 150rpm rotation [108]. The fibres were then successfully made into scaffolds for vascular grafts. More recently in 2018, the same results were achieved using the same PLCL polymer and for the same vascular grafting purpose by Pangesty *et al.* using a

commercial cotton candy maker [109]. It was seen that the fibre structure, cell affinity and mechanical properties achieved using the cotton candy maker were equal to those created using the custom set up. Subsequently, other studies have used this method successfully to create PLCL fibres for other applications. Tran *et al.* this year showed that the method can be used to create layers microfibrous structures, and also showed the importance on the degradation of the PLCL before spinning in order to improve performance [110].

PLCL fibres were created using this method in a four-step process. Firstly the as received PLCL pellets were degraded to lower the average molecular, as experience showed the melt spinning by commercial cotton candy maker was impossible with high M_w PLCL. To degrade the polymer it was stored at 120°C for 6 weeks, which effectively accelerated the hydrolyzation process. Once prepared, 3g of polymer pellets were inserted into the cotton candy maker heated to 180°C and rotating at 180rpm, and fibres were collected using a Teflon rod, as shown in Figure 3.1. Once collected as a dense fibre mat, the PLCL was cut from the Teflon rod. Fibres were then further processed in one of four ways, in order to create fibres of short and varying average lengths. The first group was immediately blended with water in a commercial blender, as shown in Figure 3.1b, for 30 seconds. The second group was immediately blended with water in the same commercial blender for 2 minutes. The third group was further allowed to degrade before blending, by leaving in a humid, incubated environment for 3 months before similar blending for 30 seconds. The final group was further degraded, then blended for 2 minutes. This process resulted in 4 groups of fibres, each with a different average length, $\bar{l}$, determined using SEM microscopy.

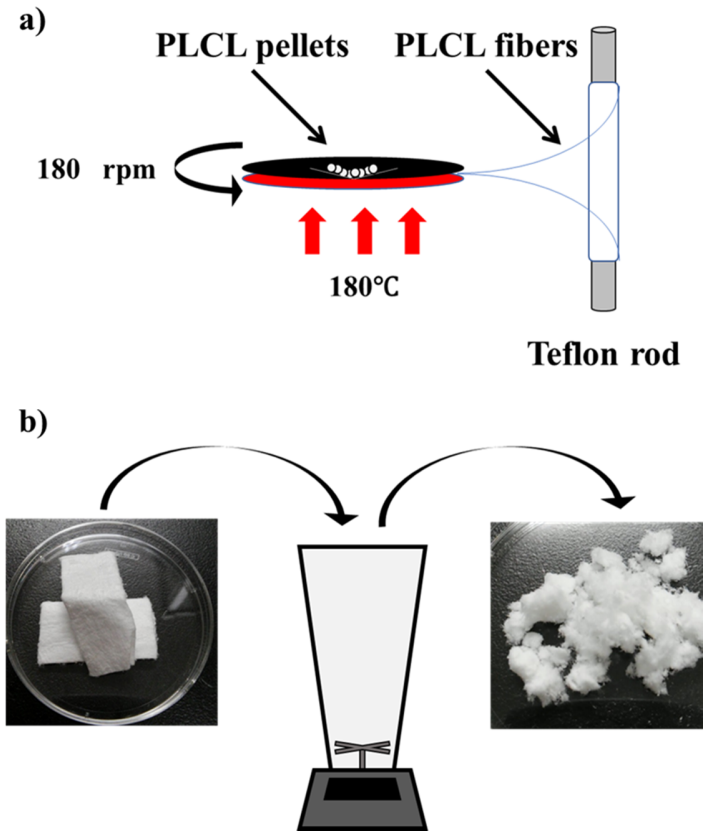

Figure 3.1 Fabrication processes of PLCL fibres using commercial cotton candy maker and blender; a) degraded PLCL pellets are spun into fibres and collected on a Teflon rod, b) fibre mats are then blended to create PLCL fibre floss, either with or without further degrading.

3.2.2 Fabrication of composite material

Monocalcium phosphate monohydrate was combined with β-tricalcium phosphate in a 1:1 molar ratio to form the dry powder as outlined by Han et al. [111]. This was in turn combined with glycerol in a solid/liquid mass ratio of 3.7, to form the anhydrous

slurry. Anhydrous cement slurries were combined with PLCL fibres at varying w/w ratios and mechanically mixed for >5 minutes. This final slurry was compressed into Teflon moulds, being firmly compacted with a Teflon rod. Samples were then incubated in phosphate buffer solution under a 5% CO_2 atmosphere at 37°C for 48 hours to simulate physiological conditions post-injection.

3.3 Characterization

3.3.1 XRD and SEM

X-ray diffractometry was performed using the method outlined in Chapter 2. Each of the five samples as well as samples of each reactant and the product of the reaction were measured. This was done in order to confirm the completion of the reaction, and determine whether the fibres present in samples prevented completion of the reaction.

SEM images of each group of fibres were used to determine average fibre lengths, $\bar{l}$, in each group. Images were also made of the composite after fabrication to investigate the fibre/ceramic interface, and determine the prevalence of voids in the material. Finally, SEM imaging was used to confirm the presence of dicalcium phosphate dihydrate in the material by looking for its distinctive, rectangular crystals. Figure 3.2 shows an example of the distinctive rectangular shape of dicalcium phosphate dihydrate crystals.

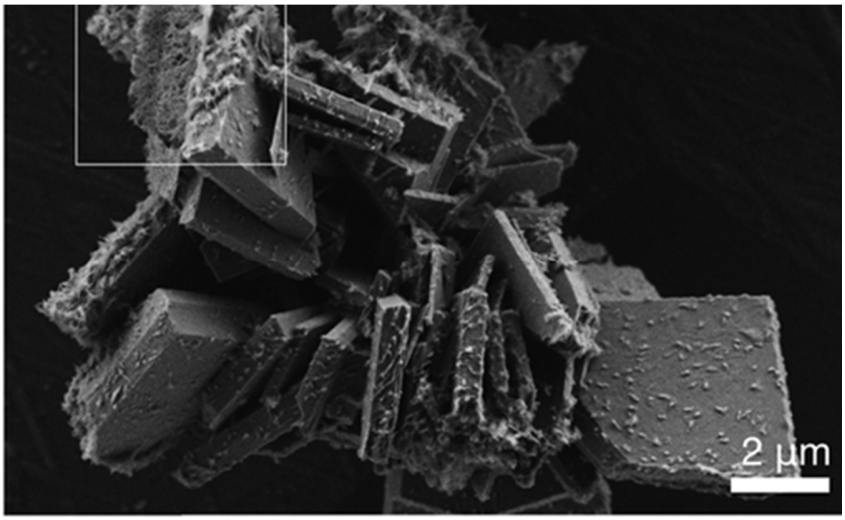

Figure 3.2 SEM micrograph of distinctly rectangular dicalcium phosphate dihydrate crystals, from literature [112].

3.3.2 Compressive testing

Compressive testing is used to measure the compressive strength and compressive Young's modulus of a material. A sample of material is cut or moulded into a known geometry; a cylinder is used in this study. The sample is placed on a flat surface under a mechanical loading head, and put under load at a constant strain. The calcium phosphate ceramic material is a brittle material, and so it can be assumed that the surface area of the material, *A*, under load is constant. A load-displacement curve is measured for the material under compression, until fracture. The peak load withstood by the material, P_{max}, divided by the cross sectional area, *A*, of the sample is the strength of the material under uniaxial compression until failure, also called the Ultimate Compressive Strength/Stress (σ_c) of the material, see Equation 3.1 below.

$$\sigma_c = \frac{P_{max}}{A} \qquad 3.1$$

It is also possible to derive a formula relating the gradient of the load-displacement curve and the compressive Young's modulus of the material, such that.

$$E_C = \frac{P}{\Delta L} \cdot \frac{L}{A} \qquad 3.2$$

Where E_C is the compressive Young's modulus of the material, P is the compressive load, ΔL is the change in length of the specimen, L is the original length of the specimen before compression, and A is the cross sectional area of the specimen. As ΔL is equal to ω, the displacement of the load head, $\Delta P/\Delta L$ is the initial gradient of the load-displacement curve. Figure 3.3 shows a typical load-displacement curve from this experiment, with relevant features discussed, as well as the typical geometry of a sample.

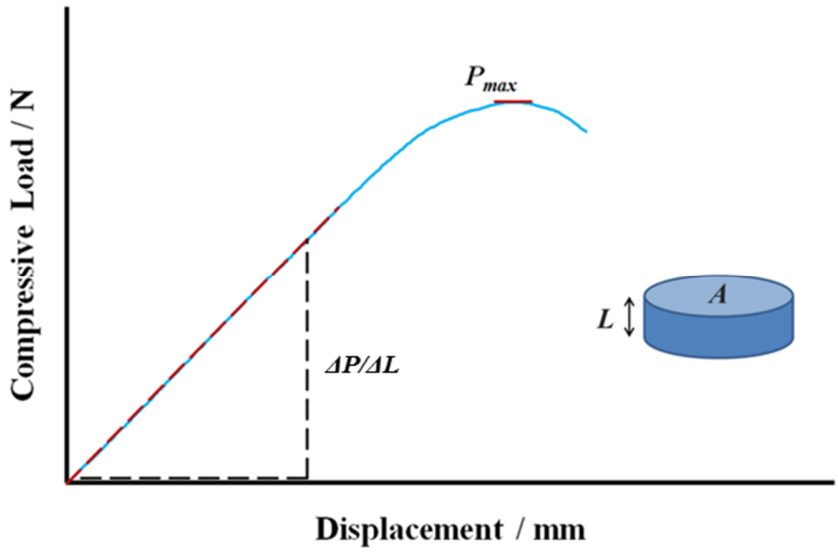

Figure 3.3 A typical load displacement curve obtained from a compressive test, showing P_{max}, $\Delta P/\Delta L$, and the geometry of samples prepared for compressive testing.

3.3.3 Micro-CT imaging and FE analysis

A Bruker SKYSCAN 1176 – High Resolution X-Ray Microtomograph was used to image samples of composite containing each fibre type, alongside a blank control. CT imaging was performed using x-rays filtered through 0.5 mm of aluminium, at 50 kV and a 500 μA current. The resulting images measured calcium density in a volume within the composite, with a voxel size of 8.8 μm per side. The software Mechanical Finder v7.0 was used to stitch individual images into three-dimensional finite element models for analysis.

In order to determine the effect of fibre length on the formation of voids within the ceramic composite, FE models were used. The total volume of the sample, V_T was determined based only on measuring the outside of the material and assuming a homogenous solid within. Then, the ceramic volume, V_C was determined by measuring the volume of all voxels in the FE model which had a high calcium density. The difference between the two gives the apparent volume of empty space within the sample. The apparent empty space is a combination of the volume of the PLCL fibres, V_F, and the volume of empty voids, V_V. If the fibres are completely meshed within the cement matrix, then the volume of truly empty voids should approach zero. If the fibres are causing voids within the cement matrix, then the value of V_V will increase. The ratio of V_V to V_T therefore provides a dimensionless parameter for ceramic/fibre integration, ρ. Equation 3.3 summarizes this calculation, and shows that as $V_C + V_F \rightarrow V_T$, $\rho \rightarrow 0$.

$$\rho = {}^{V_V}/_{V_T} = 1 - \frac{(V_C + V_F)}{V_T} \qquad 3.3$$

3.4 Results and Discussion

3.4.1 Bioceramic/ biopolymer fibre composite

The results from the FE-SEM imaging of fibres are summarized in Table 3.1, which measured the variation in $\bar{l}$ from the four processing methods. Figure 3.4 shows SEM micrographs of fibres from each group used for determining $\bar{l}$.

Table 3.1: Variation in mean fibre length for each processing method.

Group	$\bar{l}$ **/ µm**	σ **/ µm**	***n***
A	1280	350	10
B	396	107	20
C	744	238	16
D	445	127	20

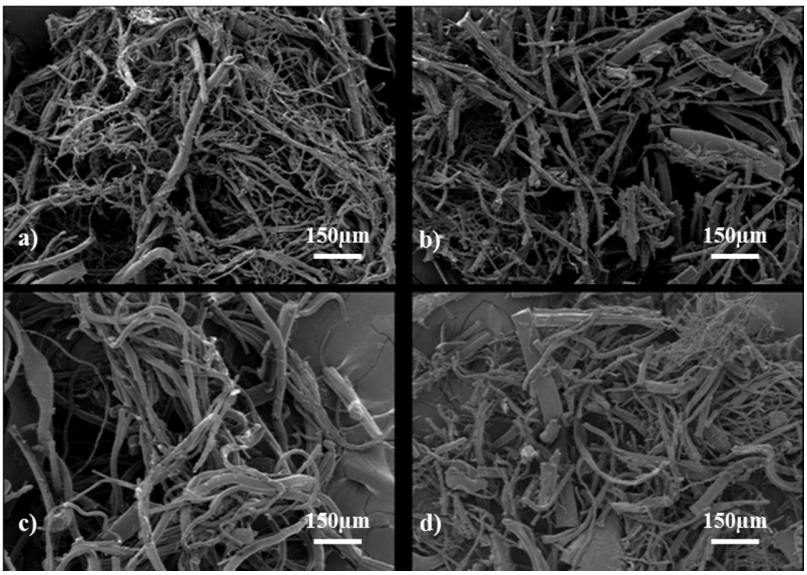

Figure 3.4 SEM micrographs of PLCL fibres from group a) A, b) B, c) C and d) D.

Fabrication of the composite was also successful. Figure 3.5 shows an example bioceramic/biopolymer composite of 25%w/w PLCL fibres of average fibre length 445μm in a dicalcium phosphate dihydrate ceramic matrix. Figure 3.6 is the XRD spectrum taken to show the conversion of monocalcium phosphate dihydrate into dicalcium phosphate dihydrate during the fabrication process. All composites showed 2θ peaks at 11.8 and 21.1, indicating dicalcium phosphate dihydrate present. All also showed no 2θ peaks at 15.2 and 46.6, indicating no significant monocalcium phosphate monohydrate present, hence a completed reaction. 2θ peaks at 27.9, 31.1 and 34.4 are attributed to excess β-tricalcium phosphate. Figure 3.7 shows an SEM image of the distinctive dicalcium phosphate dihydrate crystals present in the composite, which supports the XRD data in confirming the reaction took place.

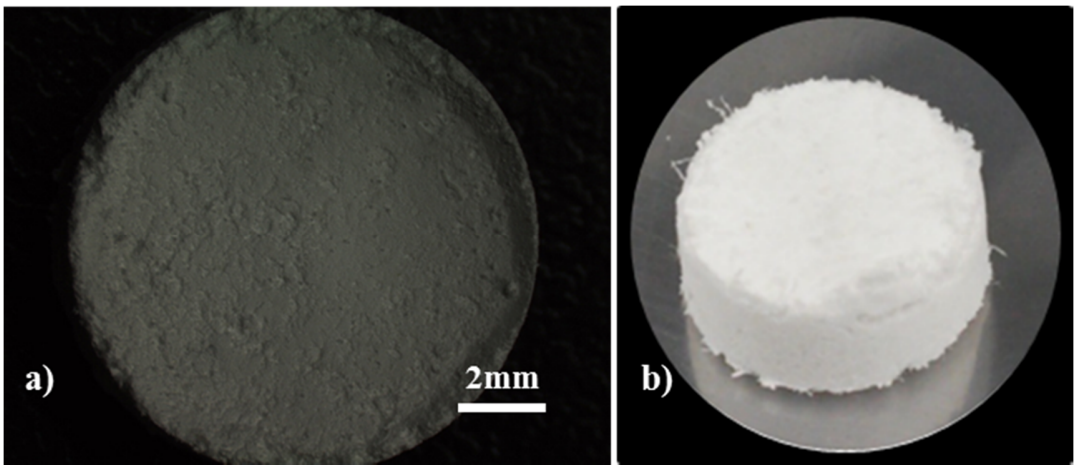

Figure 3.5 Example calcium phosphate ceramic with 25%w/w 445μm average length PLCL fibre a) optical micrograph, b) photograph.

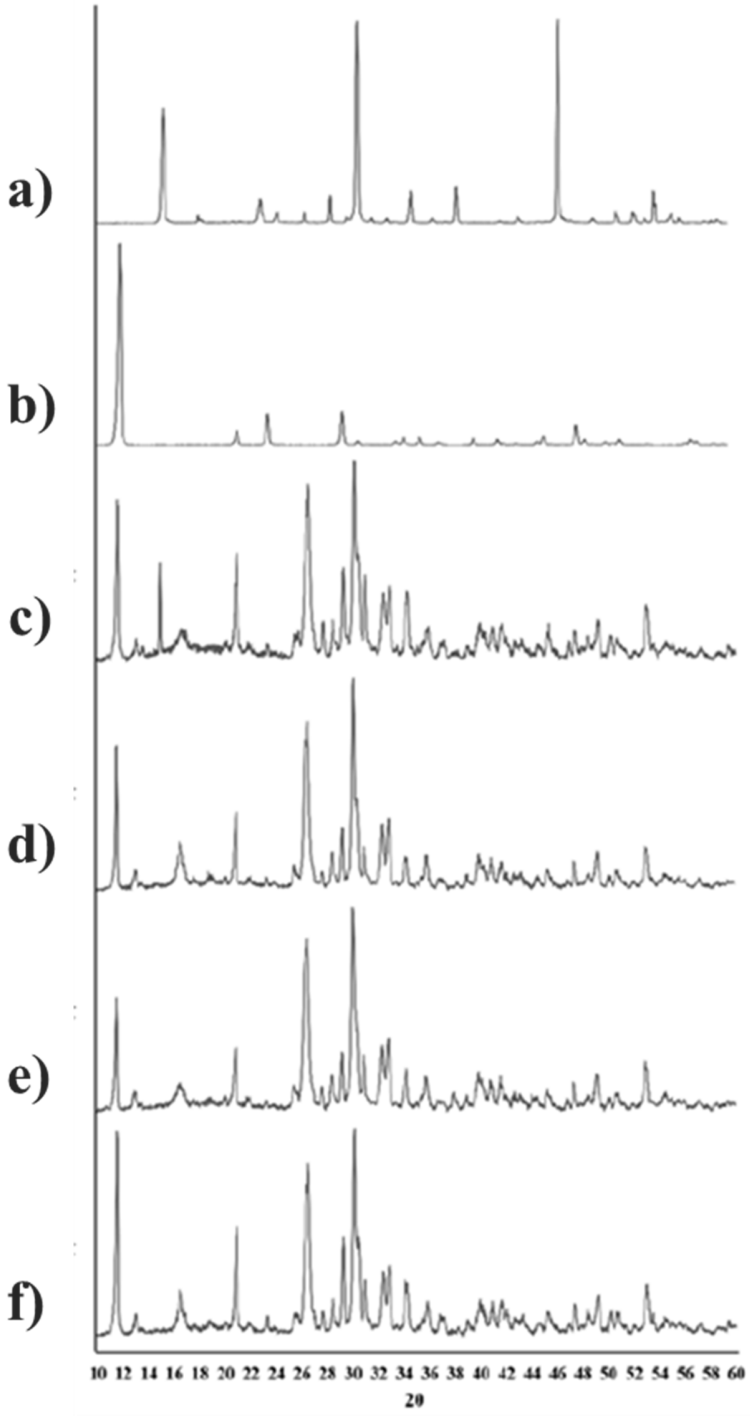

Figure 3.6 XRD spectrographs of a) monocalcium phosphate monohydrate, b) dicalcium phosphate dihydrate, c) 1280µm, d) 396µm, e) 744µm and f) 445µm average PLCL fibre length containing composite materials.

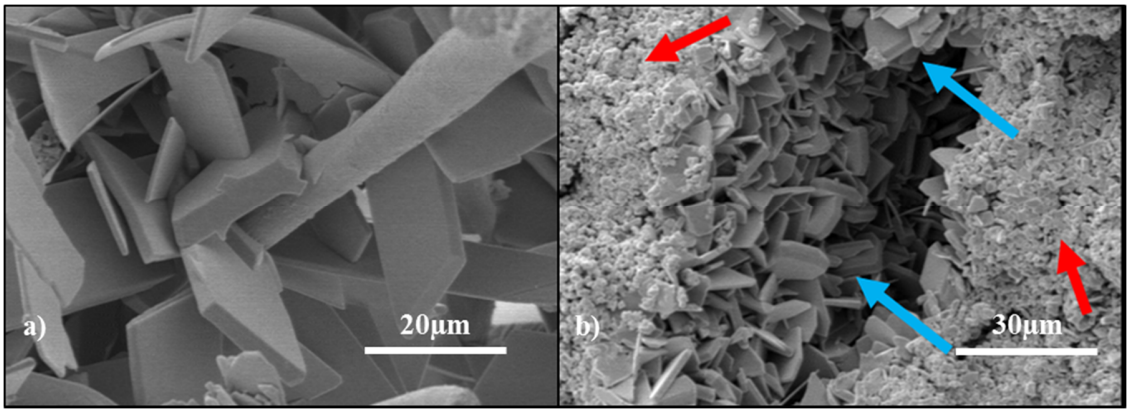

Figure 3.7 SEM micrographs showing dicalcium phosphate dihydrate crystals present in 1280µm average length PLCL fibre containing composite, b) blue arrows indicate dicalcium phosphate dihydrate crystals compared with red arrows, β-TCP crystals.

3.4.2 Micro-CT and void calculations

The total volume and ceramic volume, V_T and V_C of each sample was determined using the data gathered from micro-CT scans and the software Mechanical Finder v7.0. Figure 3.8 shows the distribution of ceramic within a central slice of the cylindrical sample for each group. Figure 3.9 shows the calculated values of ρ for each group, using the data from the micro-CT scans, and Equation 3.3. The value of V_F was calculated by weighing the mass of PLCL fibres used to fabricate each sample before inclusion into the ceramic matrix, and dividing by the known constant density of PLCL, 1.145g mL^{-1} [113].

As expected, ρ for blank dicalcium phosphate dihydrate ceramic approached zero, indicating that fibre presence was the major cause of void formation. Increasing fibre length correlated linearly to an increase in ρ. Thus, it can be concluded that ρ is an accurate parameter for fibre/cement integration.

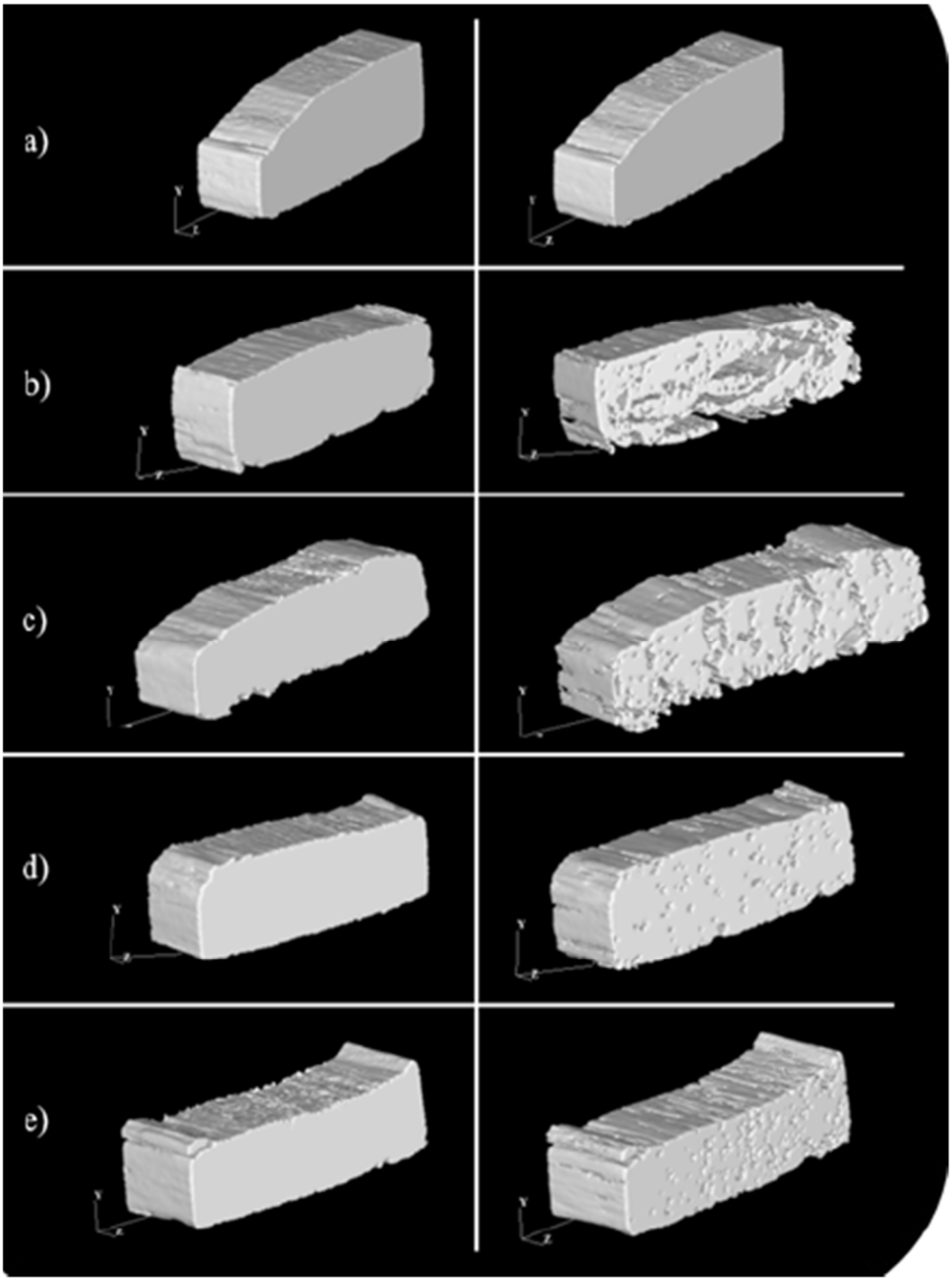

Figure 3.8 FE models built from micro-CT data showing total volume, V_T, and the ceramic volume, V_C, of a slice of each sample, a) blank ceramic, b) 1280µm, c) 744µm, d) 445µm and e) 396µm average length PLCL fibre containing composites.

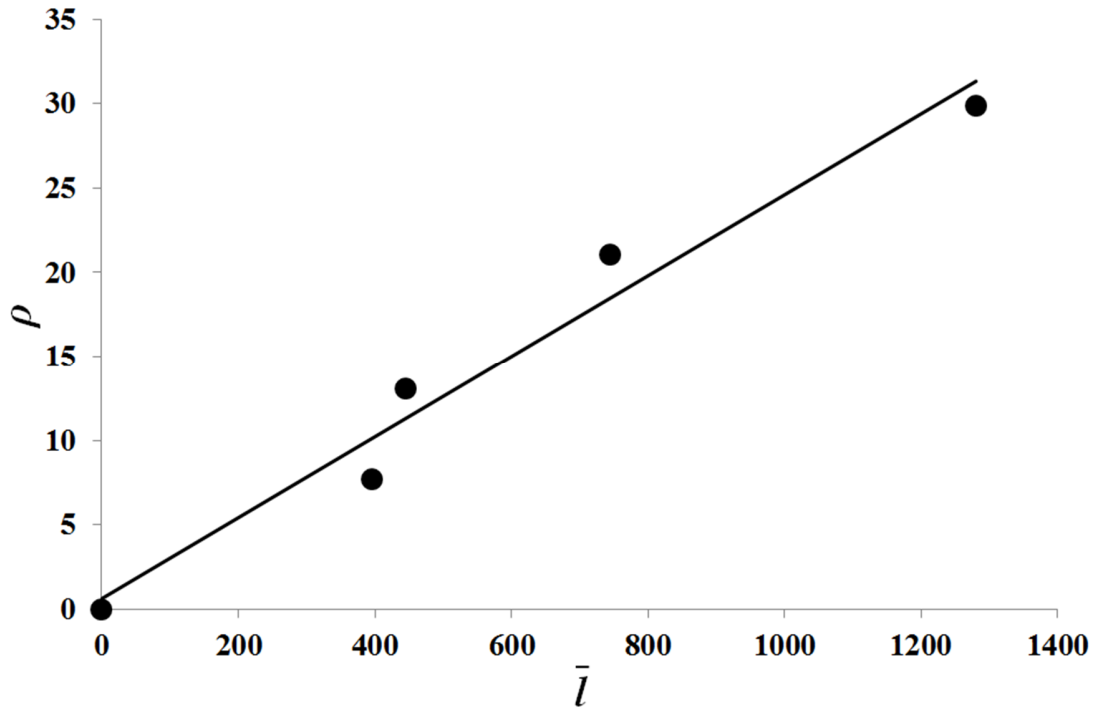

Figure 3.9 Linear correlation between packing factor, ρ, and average fibre length, $\bar{l}$.

3.4.3 Mechanical testing of bioceramic/biopolymer fibre composite

The compressive elastic modulus, *E*, of all composites was far lower than that of blank dicalcium phosphate dihydrate. The PLCL fibres of around 700μm length reduced the compressive elastic modulus of the dicalcium phosphate ceramic most drastically, from 1.3 ± 0.2 GPa to 0.27 ± 0.07 GPa. Figure 3.10 shows the change in *E* as a variable of both ρ and $\bar{l}$. It seems that the presence of any PLCL fibre reduces the elastic modulus of the composite drastically, levelling out between 0.27 and 0.6 GPa. This is an excellent result, as Table 1.2 tells us that cancellous bone has a compressive elastic modulus, *E*, of 0.1-1GPa. This means that the PLCL fibre has reduced the elastic modulus of dicalcium

phosphate dihydrate down to match that of bone, an essential requirement to designing a kyphoplasty filler biomaterial which will not cause stress shielding *in vivo*.

Figure 3.11 shows the variation in compressive strength of the composites with varying $\bar{l}$. Ceramics containing fibres were uniformly stronger than dicalcium phosphate dihydrate alone, as the fibres bound the material together. Even though the longer fibres also created empty voids within the material (increased ρ), the effect of binding overpowered the effect of increased voids. It can be seen that fibres of average length around 400μm were the strongest, as they received the benefit of the fibres binding the material together, whilst also having the lowest value of ρ. The compressive strength of this material doubled from 16 ± 3 MPa for blank dicalcium phosphate dihydrate ceramic, to 32 ± 2 MPa. As the compressive strength of cancellous bone, as before taken from Table 1.2, is around 1-16 MPa, this increase due to the inclusion of biopolymer fibres actually ensures this material could be used in load bearing applications.

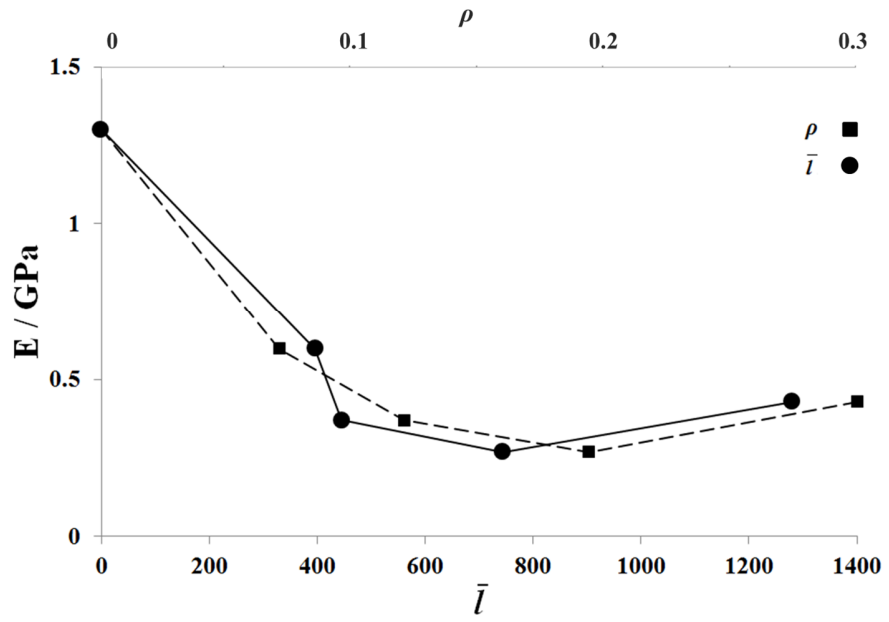

Figure 3.10 Variation in elastic modulus of PLCL fibre containing composites and blank ceramic with respect to ρ and $\bar{l}$.

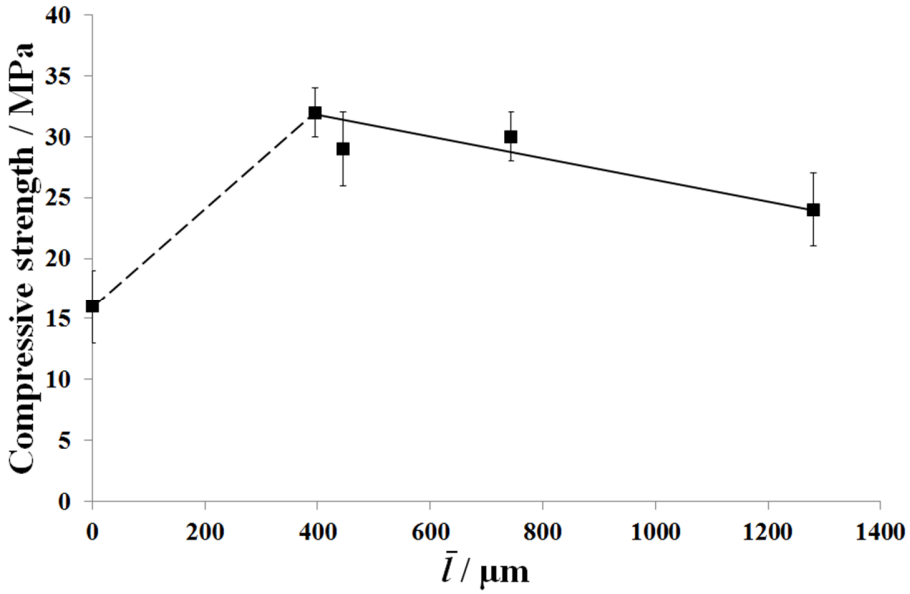

Figure 3.11 Variation in compressive strength of composite material with respect to $\bar{l}$, average PLCL fibre length.

3.5 Conclusions

The fabrication of PLCL fibres and their characterization was completed, and the methods and materials used are all suitable for low-cost and quick large scale application if required. The fibres were successfully incorporated into a bioceramic slurry of two precursor calcium phosphates, and under aqueous, physiological conditions the correct dicalcium phosphate dihydrate composite was formed. This was confirmed through SEM imaging and XRD spectroscopy. The packing of the fibres of different lengths within the composite was analyzed using computed micro-CT data and FE modelling, and a packing parameter, ρ, was established. ρ was seen to increase linearly with average fibre length $\bar{l}$.

The improvement in flexibility and compressive strength shown by the shorter fibre groups, around 400μm length, is remarkable, and has brought the biomaterial into the range where it is useful for biomedical applications. By reducing the compressive elastic modulus to within the range of cancellous bone, and doubling the compressive strength of the material, many of the problems faced by ordinary dicalcium phosphate dihydrate have been overcome.

CHAPTER 4: GENERAL CONCLUSIONS

In this study, two types of biomaterial composites were successfully fabricated and mechanically tested; a biopolymer matrix containing calcium phosphate bioceramic microbeads for use as bone plates, and a calcium phosphate injectable ceramic containing biopolymer fibres for kyphoplasty surgery. The results of this research can be summarized as follows:

1. In Chapter 2, the method for producing bioceramic microbeads was investigated and optimized. The optimized beads were then included in three types of biopolymer matrix; PLLA, PCL and a 50:50 blend of the two. The effects of adding microbeads on the mechanical properties of the materials varied greatly by material, due to differences in their elastic moduli and their interactions with the microbead surface. Close analysis of the fracture surfaces showed that PLLA permeated into the microbeads, causing the beads to cleave during fracture, and creating regions of high strain energy density in the surrounding polymer, which lead to brittle fracture and reduced fracture toughness. In the blended polymer, no polymer inclusion into the microbeads was seen, instead the polymer formed a boundary layer around each bead, creating voids and also reducing fracture toughness and causing beads to pull out during fracture. In PCL, the material wetted the surface of the microbeads, but did not permeate the calcium phosphate surface, leading to beads also pulling out during fracture, but no corresponding reduction in fracture toughness. Overall, PCL maintained its mechanical properties best, providing

an interesting composite material for future research. The investigation into fracture mechanisms was important to understand why these different effects occurred, and gives information when designing future materials.

2. In Chapter 3, PLCL fibres of four different average lengths were produced, and successfully incorporated into a dicalcium phosphate dihydrate matrix through the reaction of monocalcium phosphate monohydrate and β-tricalcium phosphate under physiological conditions. This showed that the material composite could be suitable for use in kyphoplasty surgery. The effect of fibre length on compressive strength of the bioceramic and compressive elastic modulus of the bioceramic was investigated, as well as the packing of the fibres within the material. A parameter, ρ, was established to represent fibre packing within the material. Micro-CT scans and FE modelling were used to correlate ρ with fibre length. It was shown that by including PLCL fibres of average length 400μm into the bioceramic, the compressive strength of the material doubled. The fibres also had the effect of reducing the compressive elastic modulus drastically, making the material as flexible as cancellous bone. This is another excellent result, as the high stiffness of materials used for kyphoplasty has previously been blamed for many complications after surgery.

APPENDIX

A.1 XRD peak data from microbead analysis, Figure 2.10.

CuK-α: 30kV: 15mA.α-tricalcium_phosphate

No.	2-theta(deg)	d(ang.)	Height(cps)
1	12.225(17)	7.234(10)	24(4)
2	14.140(14)	6.258(6)	16(4)
3	15.266(17)	5.799(6)	11(3)
4	17.21(3)	5.148(9)	23(4)
5	22.283(19)	3.986(3)	38(6)
6	22.955(14)	3.871(2)	124(10)
7	24.249(18)	3.667(3)	71(8)
8	26.77(7)	3.327(8)	12(3)
9	29.787(11)	2.9969(11)	50(6)
10	30.777(8)	2.9028(7)	332(17)
11	31.350(16)	2.8510(14)	74(8)
12	31.876(8)	2.8051(7)	20(4)
13	32.29(4)	2.770(3)	34(5)
14	34.372(11)	2.6070(8)	162(12)
15	40.05(13)	2.250(7)	14(3)
16	41.76(3)	2.1610(14)	55(7)
17	42.34(4)	2.1330(19)	28(5)
18	44.39(7)	2.039(3)	26(5)
19	46.810(14)	1.9391(6)	112(10)
20	47.85(2)	1.8994(9)	31(5)
21	50.080(12)	1.8199(4)	32(5)
22	50.64(6)	1.801(2)	19(4)
23	52.15(2)	1.7525(8)	28(5)
24	52.91(10)	1.729(3)	14(3)
25	55.05(9)	1.667(3)	19(4)
26	59.66(11)	1.549(3)	19(4)
27	62.98(15)	1.475(3)	9(3)

CuK-α: 30kV: 15mA. hydroxyapatite

No.	2-theta(deg)	d(ang.)	Height(cps)
1	10.82(5)	8.17(4)	14(3)
2	16.91(4)	5.237(12)	7(2)
3	21.88(5)	4.058(10)	10(3)
4	22.99(4)	3.865(6)	11(3)
5	25.930(13)	3.4333(17)	117(10)
6	28.18(3)	3.164(3)	24(4)
7	29.02(3)	3.075(3)	29(5)
8	31.86(2)	2.8065(18)	114(10)
9	32.19(3)	2.778(2)	202(13)
10	32.980(17)	2.7137(13)	143(11)
11	34.171(19)	2.6218(14)	62(7)
12	39.98(3)	2.2533(17)	50(6)
13	42.03(7)	2.148(4)	15(4)
14	43.92(6)	2.060(3)	17(4)
15	46.76(3)	1.9411(11)	76(8)
16	48.19(5)	1.8869(19)	28(5)
17	49.508(17)	1.8396(6)	98(9)
18	50.58(4)	1.8030(12)	39(6)
19	51.43(6)	1.7753(18)	26(5)
20	52.15(4)	1.7525(12)	34(5)
21	53.21(2)	1.7200(7)	57(7)
22	55.92(8)	1.643(2)	15(4)
23	57.15(9)	1.610(2)	12(3)
24	61.65(6)	1.5032(13)	20(4)
25	63.04(7)	1.4734(15)	20(4)
26	64.05(5)	1.4526(9)	39(6)
27	65.19(7)	1.4298(13)	22(4)

CuK-α: 30kV: 15mA. sintered_microbead

No.	2-theta(deg)	d(ang.)	Height(cps)
1	10.99(3)	8.04(2)	15(4)
2	12.17(3)	7.266(18)	15(4)
3	13.71(3)	6.453(13)	22(4)
4	14.13(5)	6.26(2)	9(3)
5	17.093(18)	5.183(6)	40(6)
6	20.29(4)	4.373(8)	13(3)
7	21.95(3)	4.047(5)	30(5)
8	22.27(4)	3.989(8)	20(4)
9	22.933(17)	3.875(3)	60(7)
10	24.23(3)	3.670(4)	32(5)
11	25.92(2)	3.435(3)	85(8)
12	26.61(2)	3.347(3)	26(5)
13	27.905(14)	3.1946(16)	176(12)
14	29.75(3)	3.001(3)	63(7)
15	30.87(2)	2.895(2)	138(11)
16	31.097(13)	2.8736(11)	357(17)
17	31.784(17)	2.8131(15)	116(10)
18	32.27(4)	2.772(3)	68(8)
19	32.54(3)	2.749(2)	65(7)
20	32.93(2)	2.7174(19)	80(8)
21	34.461(12)	2.6004(9)	266(15)
22	35.14(4)	2.552(3)	32(5)
23	35.62(4)	2.518(3)	35(5)
24	37.44(3)	2.4001(18)	41(6)
25	37.88(4)	2.373(2)	30(5)
26	39.207(17)	2.2958(10)	11(3)
27	39.85(3)	2.2602(14)	61(7)
28	41.13(4)	2.1927(18)	42(6)
29	41.77(3)	2.1606(16)	49(6)
30	43.63(4)	2.0728(18)	32(5)
31	43.97(3)	2.0577(13)	23(4)
32	44.62(6)	2.029(2)	28(5)
33	45.36(4)	1.9977(18)	32(5)
34	46.89(3)	1.9362(10)	101(9)
35	48.06(4)	1.8915(13)	76(8)
36	48.42(3)	1.8784(10)	62(7)
37	50.53(3)	1.8048(12)	23(4)
38	51.36(11)	1.777(3)	21(4)
39	53.04(3)	1.7251(8)	116(10)
40	53.68(6)	1.7061(17)	32(5)
41	55.077(17)	1.6660(5)	22(4)
42	57.43(9)	1.603(2)	15(4)
43	59.58(2)	1.5505(6)	60(7)

A.2 Fracture element data from FE simulations in Chapter 2.4.2.4.

Model	Youngs / MPa	Crosshead Distance / mm	Sum fracture total
Double Bead 6mm	5000	0	0
		0.2	0
		0.4	0
		0.6	9
		0.8	398
		1	1743
	7500	0	0
		0.2	0
		0.4	0
		0.6	9
		0.8	411
		1	1805
	10000	0	0
		0.2	0
		0.4	0
		0.6	9
		0.8	426
		1	1907
	12500	0	0
		0.2	0
		0.4	0
		0.6	9
		0.8	426
		1	1964
	15000	0	0
		0.2	0
		0.4	0
		0.6	9
		0.8	427
		1	1990
	50000	0	0
		0.2	0
		0.4	0
		0.6	9
		0.8	474
		1	2072
Single Bead	5000	0	0
		0.2	0

		0.4	0
		0.6	107
		0.8	499
		1	1171
	7500	0	0
		0.2	0
		0.4	0
		0.6	106
		0.8	497
		1	1204
	10000	0	0
		0.2	0
		0.4	0
		0.6	106
		0.8	495
		1	1241
	12500	0	0
		0.2	0
		0.4	0
		0.6	106
		0.8	499
		1	1251
	15000	0	0
		0.2	0
		0.4	0
		0.6	106
		0.8	509
		1	1320
	50000	0	0
		0.2	0
		0.4	0
		0.6	115
		0.8	547
		1	1366
Blank PLLA		0	0
		0.2	0
		0.4	0
		0.6	0
		0.8	0
		1	0

REFERENCES

[1] H. Ellis, A History of Surgery, Greenwich Medical Media Ltd., London, 2001.

[2] B. Browner, Skeletal Trauma: Basic Science, Management and Reconstruction Volume 2, Saunders Elsevier, Philadelphia, 2009.

[3] A. Swanson, S. Jaeger, D. la Rochelle, Comminuted fractures of the radial head. The role of silicone-implant replacement arthroplasty, J. Bone Joint Surg. Am. 63 (1981) 1039-1049. PMID: 7276041

[4] M. Haseeb, M. Butt, T. Altaf, K. Muzaffar, A. Gupta, A. Jallu, Indications of implant removal: A study of 83 cases, Int. J. Health. Sci. 11 (2017) 1-7. PMID: 28293156

[5] F. Kovar, E. Strasser, M. Jaindl, G. Endler, G. Oberleitner, Complications following implant removal in patients with proximal femur fractures – An observational study over 16 years, Orthop. Traumatol. Sur. 101 (2015) 785-789. DOI: 10.1016/j.otsr.2015.07.021

[6] C. Wong, M. McGirt, Vertebral compression fractures: a review of current management and multimodal therapy, J. Multidiscip. Healthc. 6 (2013) 205-214. DOI: 10.2147/JMDH.S31659

[7] V. Denaro, U. Longo, N. Maffulli, L. Denaro, Vertebroplasty and

kyphoplasty, Clin. Cases Miner. Bone Metab. 6 (2009) 125-130. PMCID: PMC2781232

[8] S. Bonnick, Osteoporosis in men and woman, Clin. Cornerstone 8 (2006) 28-39. DOI: 10.1016/s1098-3597(06)80063-3

[9] C. David, C. Confavreux, N. Mehsen, J. Paccou, A. Leboime, E. Legrand, Severity of osteoporosis: What is the impact of co-morbidities?, Joint. Bone Spine 77 (2010) 103-106. DOI: 10.1016/S1297-319X(10)70003-8

[10] E. Dennison, C. Cooper, Epidemiology of osteoporotic fractures, Horm. Res. 54 (2000) 58-63. DOI: 10.1159/000063449

[11] A. Rapado, General management of vertebral fractures, Bone 18 (1996) 191-196. DOI: 10.1016/8756-3282(95)00501-3

[12] S. Garfin, H. Yuan, M. Reiley, New technologies in spine: Kyphoplasty and vertebroplasty for the treatment of painful osteoporotic compression fractures, Spine 26 (2001) 1511-1515. DOI: 10.1097/00007632-200107150-00002

[13] H. Chen, H. Yang, P. Jia, L. Bao, H. Tang, Effectiveness of kyphoplasty in the treatment of osteoporotic vertebral compression fracture patients with chronic kidney disease, J. Orthoped. Sci. 21 (2016) 571-578. DOI: 10.1016/j.jos.2016.05.004

[14] C. Xu, H. Liu, H. Xu, Analysis of related factors on the deformity correction

of balloon kyphoplasty, Am. J. Neuroradiol. 35 (2013) 202-206. DOI: 10.3174/ajnr.a3617

[15] M. Bozkurt, G. Kahilogullari, M. Ozdemir, O. Ozgural, A. Attar, S. Caglar, C. Ates, Comparative analysis of vertebroplasty and kyphoplasty for osteoporotic vertebral compression fractures, Asian Spine J. 8 (2014) 27-34. PMCID: PMC3939366

[16] A. Mudano, J. Bian, J. Cope, J. Curtis, T. Gross, J. Allison, Y. Kim, D. Briggs, M. Melton, J. Xi, K. Saag, Vertebroplasty and kyphoplasty are associated with an increased risk of secondary vertebral compression fractures: A population-based cohort study, Osteoporosis Int. 20 (2009) 819-826. DOI: 10.1007/s00198-008-0745-5

[17] J. Wu, Y. Guan, S. Fan, Analysis of risk factors of secondary adjacent vertebral fracture after percutaneous kyphoplasty, Biomed. Res. 28 (2017) 1956-1961.

[18] M. Liebschner, W. Rosenberg, T. Keaveny, Effects of bone cement volume and distribution on vertebral stiffness after vertebroplasty, Spine 26 (2001) 1547-1554. DOI: 10.1097/00007632-200107150-00009

[19] B. Dickey, M. Tyndyk, D. Doman, D. Boyd, In silico evaluation of stress distribution after vertebral body augmentation with conventional acrylics, composites and glass polyalkenoate cements, J. Mech. Behav. Biomed. Mater. 5 (2012) 283-290. DOI: 10.1016/j.jmbbm.2011.08.007

[20] A. Polikeit, P. Nolte, S. Ferguson, The effect of cement augmentation on the load transfer in an osteoporotic functional spinal unit: Finite-element analysis, Spine 28 (2003) 991-996. DOI: 10.1097/01.BRS.0000061987.71624.17

[21] P. Alexander, T. Fathima, R. Jeniffa, P. Praseetha, Scaffolds used for bone tissue regeneration: Review, Res. J. Pharm. Biol. Chem. Sci. 7 (2016) 1624-1636.

[22] U. Sampath, Y. Ching, C. Chuah, J. Sabariah, P. Lin, Fabrication of porous materials from natural/synthetic biopolymers and their composites, Materials 9 (2016) 991, DOI: 10.3390/ma9120991

[23] K. Burg, S. Porter, J. Kellam, Biomaterial developments for bone tissue engineering, Biomaterials 21 (2000) 2347-2359. DOI: 10.1016/s0142-9612(00)00102-2

[24] J. Fernandez, A. Etxeberria, J. Sarasua, Synthesis, structure and properties of poly(L-lactide-co-ε-caprolactone) statistical copolymers, J. Mech. Behav. Biomed. Mater. 9 (2012) 100-112. DOI: 10.1016/j.jmbbm.2012.01.003

[25] C. Harper, Modern Plastics Handbook, McGraw-Hill, New York, 1999.

[26] A. Sodergard, M. Stolt, Properties of lactic acid based polymers and their correlation with composition, Prog. Polym. Sci. 27 (2002) 1123-1163. DOI: 10.1016/S0079-6700(02)00012-6

[27] C. Chu, Materials for absorbable and nonabsorbable surgical sutures. In: Biotextiles as Medical Implants, Woodhead Publishing Ltd., Cambridge, 2013.

[28] J. Middleton, A. Tipton, Synthetic biodegradable polymers as orthopedic devices, Biomaterials 21 (2000) 2335-2346. DOI: 10.1016/s0142-9612(00)00101-0

[29] D. Rosa, I. Neto, M. Cail, A. Pedroso, C. Fonseca, S. Neves, Evaluation of the thermal and mechanical properties of poly(epsilon-caprolactone), low-density polyethylene, and their blends, J. Appl. Polym. Sci. 91 (2004) 3909-3914. DOI: 10.1002/app.13596

[30] J. Fernandez, A. Etxeberria, J. Sarasua, Synthesis, structure and properties of poly(L-lactide-co-ε-caprolactone) statistical copolymers, J. Mech. Behav. Biomed 9 (2012) 100-112. DOI: 10.1016/j.jmbbm.2012.01.003

[31] J. Fernandez, A. Larranaga, A. Etxeberria, W. Wang, J. Sarasusa, A new generation of poly(lactide/ε-caprolactone) polymeric materials for application in the medical field, J. Biomed. Mater. Res. A, 102 (2013) 3573-3584. DOI: 10.1002/jbm.a.35036

[32] J. Pan, N. Liu, H. Sun, F. Xu, Preparation and characterization of electrospun PLCL/poloxamer nanofibers and dextran/gelatin hydrogels for skin tissue engineering, PLoS ONE 9 (2014) e112885. DOI:

10.1371/journal.pone.0112885

[33] W. Habraken, P. Habibovic, M. Epple, M. Bohner, Calcium phosphates in biomedical applications: Materials for the future?, Mater. Today 19 (2016) 69-87. DOI: 10.1016/j.mattod.2015.10.008

[34] M. Hu, P. Lee, W. Chen, J. Hu, Incorporation of collagen in calcium phosphate cements for controlling osseointegration, Materials 10 (2017) E910. DOI: 10.3390/ma10080910

[35] C. Klein, K. de Groot, A. Drissen, H. van der Lubbe, Interaction of biodegradable β-whitlockite ceramics with bone tissue: an in vivo study, Biomaterials 6 (1985) 189-192. DOI: 10.1016/0142-9612(85)90008-0

[36] K. Jeong, S. Kim, S. Moon, J. Oh, J. Jo, H. Lim, J. Kim, S. Lim, M. Jeong, Experimental study of osseointegration and stability of intentionally exposed hydroxyapatite coating implants, J. Korean Assoc. Maxillofac. Plast. Reconstr. Surg. 34 (2012) 12-16.

[37] G. Krishnamurithy, A review on hydroxyapatite-based scaffolds as a potential bone graft substitute for bone tissue engineering applications, J. Univ. Malaya Med. Cent. 16 (2013) 1-6. DOI: 10.22452/jummec.vol16no2.4

[38] H. Yi, F. Rehman, C. Zhao, B. Liu, N. He, Recent advances in nano scaffolds for bone repair, Bone Res. 4 (2016) 16050. DOI: 10.1038/boneres.2016.50

[39] J. Zhang, W. Liu, V. Schnitzler, F. Trancet, J. Bouler, Calcium phosphate

cements for bone substitution: chemistry, handling and mechanical properties, Acta Biomater. 10 (2014) 1035-1049. DOI: 10.1016/j.actbio.2013.11.001

[40] A. Amir, J. Lemaitre, Calcium phosphate cements: study of the β-tricalcium phosphate – monocalcium phosphate system, Biomaterials 10 (1989) 475-480. DOI: 10.1016/0142-9612(89)90089

[41] E. Charriere, S. Terrazzoni, C. Pittet, P. Mordasini, M. Dutoit, Mechanical characterization of brushite and hydroxyapatite cements, Biomaterials 22 (2001) 2937-2945. DOI: 10.1016/S0142-9612(01)00041-2

[42] M. Ginebra, Calcium Phosphate Bone Cements, Woodhead Publishing Ltd., Cambridge, 2008.

[43] D. Carter, W. Hayes, The compressive behaviour of bone as a two phase structure, J. Bone Joint Surg. Am. 59 (1977) 954-962. PMID: 561786

[44] A. Burstein, D. Reilly, M. Martens, Aging of bone tissue: Mechanical properties, J. Bone Joint Surg. 58 (1976) 82-86. PMID: 1249116

[45] C. Misch, Z. Qu, M. Bidez, Mechanical properties of trabecular bone in the human mandible: Implications for dental implant treatment planning and surgery placement, J. Oral Maxillofac. Surg. 57 (1999) 700-706. DOI: 10.1016/S0278-2391(99)90438-X

[46] P. Gao, H. Zhang, Y. Liu, B. Fan, X. Li, X. Xiao, P. Lan, M. Li, L. Geng, D.

Liu, Y. Yuan, Q. Lian, J. Lu, Z. Guo, Z. Wang, Beta-tricalcium phosphate granules improve osteogenesis in vitro and establish innovative osteo-regenerators for bone tissue engineering in vivo, Sci. Rep. 6 (2016) 23367. DOI: 10.1038/srep23367

[47] R. Carrodeguas, S. de Aza, α-tricalcium phosphate: Synthesis, properties and biomedical applications, Acta Biomater. 7 (2011) 3536-3546. DOI: 10.1016/j.actbio.2011.06.019

[48] M. Bohner, Design of ceramic-based cements and putties for bone graft substitution, Eur. Cells Mater. 20 (2010) 1-12. DOI: 10.22203/ecm.v020a01

[49] M. Vallet-Regi, L. Rodriguez-Lorenzo, A. Salinas, Synthesis and characterisation of calcium deficient apatite, Solid State Ion. 101 (1997) 1279-1285. DOI: 10.1016/S0167-2738(97)00213-0

[50] R. Harrison, Z. Criss, L. Feller, S. Modi, J. Hardy, C. Schmidt, L. Suggs, M. Murphy, Mechanical properties of tricalcium phosphate based bone cements incorporating regenerative biomaterials for filling bone defects exposed to low mechanical loads, J. Biomed. Mater. Res. B Appl. Biomater. 104 (2016) 149-157. DOI:10.1002/jbm.b.33362

[51] C. Hernandez, G. Beaupre, T. Keller, D. Carter, The influence of bone volume fraction and ash fraction on bone strength and modulus, Bone 29 (2001) 74-78. DOI: 10.1016/s8756-3282(01)00467-7

[52] T. Keaveny, E. Morgan, G. Niebur, O. Yeh, Biomechanics of trabecular bone. Annu. Rev. Biomed. Eng. 3 (2001) 307-333. DOI: 10.1146/annurev.bioeng.3.1.307

[53] European Chemicals Agency, Pentacalcium hydroxide tris(orthophosphate), REACH Registered Substance Factsheets (2020) echa.europa.eu/registration-dossier/-/registered-dossier/15208

[54] European Chemicals Agency, Tricalcium bis(orthophosphate), REACH Registered Substance Factsheets (2020) echa.europa.eu/registration-dossier/-/registered-dossier/13654/1

[55] European Chemicals Agency, Calcium bis(dihydrogenorthophosphate), REACH Registered Substance Factsheets (2020) echa.europa.eu/registration-dossier/-/registered-dossier/15399/4/9

[56] European Chemicals Agency, Calcium hydrogenorthophosphate, REACH Registered Substance Factsheets (2020) echa.europa.eu/registration-dossier/-/registered-dossier/15458/4/9

[57] R. Rebelo, M. Fernandes, R. Fangueiro, Biopolymers in medical implants: A brief review, Procedia Eng. 200 (2017) 236-243. DOI:10.1016/j.proeng.2017.07.034

[58] K. Masutani, Y. Kimura, Chapter 1: PLA synthesis from the monomer to polymer. In: Poly(lactic acid) science and technology: Processing, properties,

additives and applications (2014) 1-36. DOI: 10.1039/9781782624806-00001

[59] A. Majola, S. Vainionpaa, P. Rokkanen, H. Mikkola, P. Tormala, Absorbable self-reinforced polylactide (SR-PLA) composite rods for fracture fixation-strength and strength retention in the bone and subcutaneous tissue of rabbits, J. Mater. Sci. mater. Med. 3 (1992) 43-47. DOI: 10.1007/BF00702943

[60] J. Middleton, A. Tipton, Synthetic biodegradable polymers as orthopedic devices, Biomaterials 21 (2000) 2335-2346. DOI: 10.1016/s0142-9612(00)00101-0

[61] M. Simion, U. Misitiano, L. Gionso, A. Salvato, Treatment of dehiscences and fenestrations around dental implants using resorbable and nonresorbable membranes associated with bone autografts: A comparative clinical study, Int. J. Oral Maxillofac. Implants 12 (1997) 159-167. PMID: 9109265

[62] K. Tappa, U. Jammalamadaka, J. Weisman, D. Ballard, D. Wolford, C. Pascual-Garrido, L. Wolford, P. Woodard, D. Mills, 3D printed custom bioactive and absorbable surgical crews, pins, and bone plates for localized drug delivery, J. Func. Biomater. 10 (2019) 2. DOI:10.3390/jfb10020017

[63] G. Giammona, E. Craparo, Polymer-based systems for controlled release and targeting of drugs, Polymers 11 (2019) 2066-2069. DOI:10.3390/polym11122066

[64] M. Benmassaoud, C. Kohama, T. Kim, J. Kadlowec, B. Foltiny, T. Mercurio,

S. Ranganathan, Efficacy of eluted antibiotics through 3D printed femoral implants, Miomed. Microdevices 21 (2019) 51. DOI: 10.1007/s10544-019-0395-8

[65] B. Shafer, P. Simonian, Broken poly-L-lactic acid screw after ligament reconstruction, J. Arthrosc. Relat. Surg. 18 (2002) E35. DOI: 10.1053/jars.2002.32197

[66] M. Kosaka, F. Uemura, S. Tomemori, H. Kamiishi, Scanning electron microscope observations of 'fractured' biodegradable plates and screws, J. Craniomaxillofac. Surg. 31 (2003) 10-14. DOI: 10.1016/s1010-5182(02)00166-x

[67] Z. Wang, Y. Wang, Y. Ito, P. Zhang, X. Chen, A comparative study on the in vivo degradation of poly(L-lactide) based composite implants for bone fracture fixation, Sci. Rep. 6 (2016) 20770. DOI: 10.1038/srep20770

[68] Medtronic Plc, Wound Closure Catalogue (2019) 4-93.

[69] Y. Kim, K. Lee, S. Kim, Y. Jang, J. Kim, M. Lee, Improvement of osteogenesis by a uniform PCL coating on a magnesium screw for biodegradable applications, Sci. Rep. 8 (2018) 13264. DOI:10.1038/s41598-018-31359-9

[70] D. Milovac, T. Gamboa-Martinez, M. Ivankovic, G. Ferrer, H. Ivankovic, PCL-coated hydroxyapatite scaffold derived from cuttlefish bone: *In vitro*

cell culture studies, Mater. Sci. Eng. C 42 (2014) 264-272. DOI:10.1016/j.msec.2014.05.034

[71] S. Gomes, G. Rodrigues, G. Martins, M. Roberto, M. Mafra, C. Henriques, J. Silva, In vitro and in vivo evaluation of electrospun nanofibers of PCL, chitosan and gelatin: A comparative study, Mater. Sci. Eng. C 46 (2015) 348-358. DOI: 10.1016/j.msec.2014.10.051

[72] A. Pangesty, M. Todo, Development of cylindrical microfibrous scaffold using melt-spinning method for vascular engineering, Mater. Lett. 228 (2018) 334-338. DOI:10.1016/j.matlet.2018.06.046

[73] D. Marcellin-Little, B. Sutherland, O. Harrysson, E. Lee, In vitro evaluation of free-form biodegradable bone plates for fixation of distal femoral physeal fractures in dogs, Am. J. Vet. Res. 71 (2010) 1508-15. DOI: 10.2460/ajvr.71.12.1508

[74] P. Lin, H. Fang, T. Tseng, W. Lee, Effects of hydroxyapatite dosage on mechanical and biological behaviors of polylactic acid composite materials, Mater. Lett. 61 (2007) 3009-3013. DOI: 10.1016/j.matlet.2006.10.064

[75] S. Mondal, T. Nguyen, V. Pham, G. Hoang, P. Manivasagan, M. Kim, S. Nam, J. Oh, Hydroxyapatite nano bio-ceramics optimized 3D printed poly lactic acid scaffold for bone tissue engineering application, Ceram. Int. 46 (2020) 3443-3455. DOI: 10.1016/j.ceramint.2019.10.057

[76] N. Ranjan, R. Singh, I. Ahuja, Development of PLA-HAp-CS-based biocompatible functional prototype: A case study, J/ Thermoplast. Compos. 33 (2020) 305-323. DOI: 10.1177/0892705718805531

[77] E. Backes, L. Pires, C. Beatrice, L. Costa, F. Passador, L. Pessan, Fabrication of biocompatible composites of poly(lactic acid)/ hydroxyapatite envisioning medical applications, Polym. Eng. Sci. 60 (2020) 636-644. DOI: 10.1002/pen.25322

[78] J. Kane, H. Weiss-Bilka, M. Meagher, Y. Liu, J. Gargac, G. Niebur, D. Wagner, R. Roeder, Hydroxyapatite reinforced collagen scaffolds with improved architecture and mechanical properties, Acta Biomater. 17 (2015) 16-25. DOI: 10.1016/j.actbio.2015.01.031

[79] M. Todo, S. Park, K. Arakawa, Y. Takenoshita, Relationship between microstructure and fracture behavior of bioabsorbable HA/PLLA composites, Compos. Pat. A Appl. Sci. 37 (2006) 2221-2225. DOI: 10.1016/j.compositesa.2005.10.001

[80] B. Rai, J. Lin, Z. Lim, R. Guldberg, D. Hutmacher, S. Cool, Differences between in vitro viability and differentiation and in vivo bone-forming efficacy of human mesenchymal stem cells cultured on PCL-TCP scaffolds, Biomat. 31 (2010) 7960-7970. DOI:10.1016/j.biomaterials.2010.07.001

[81] E. Gonçalves, F. Oliviera, R. Silva, M. Neto, M. Fernandes, M. Amaral, M.

Vallet-Regi, M. Vila, Three-dimensional printed hydroxyapatite scaffolds filled with CNTs for bone cell growth simulation, J. Biomed. Mater. Res. B 104 (2019) 6. DOI: 10.1002/jbm.b.33432

[82] A. Bruyas, F. Lou, A. Stahl, M. Gardner, W. Maloney, S. Goodman, Y. Yang, Systematic characterization of 3D-printed PCL/β-TCP scaffolds for biomedical devices and bone tissue engineering: Influence of composition and porosity, J. Mater. Res. 33 (2018) 1948-1959. DOI: 10.1557/jmr.2018.112

[83] W. Bonfield, M. Wang, C. Au, P. Lai, Tensile and compressive behaviours and properties of a bone analogue biomaterial, Key Eng. Mater. 284-286 (2005) 693-696. DOI: 10.4028/www.scientific.net/KEM.284-286.693

[84] X. Fan, L. Guo, T. Liu, Preparation and mechanical properties of PLGA/β-TCP composites, Polym. Plas. Technol. Eng. 52 (2013) 621-625. DOI: 10.1080/03602559.2012.762661

[85] M. Todo, S. Park, T. Takayama, K. Arakawa, Fracture mechanisms of bioabsorbable PLLA/PCL polymer blends, Eng. Fract. Mech. 74 (2006) 1872-1883. DOI: 10.1016/j.engfracmech.2006.05.021

[86] M. Wang, Y. Liu, C. Au, P. Lai, L. Leung, B. Chua, Deformation and fracture of bone analogue materials having different polymer matrices, Open J. Adv. Mater. Res. 47-50 (2008) 1391-1394. DOI: 10.4028/www.scientific.net/AMR.47-50.1391

[87] Y. Liu, M. Wang, Fabrication and characteristics of hydroxyapatite reinforced polypropylene as a bone analogue biomaterial, J. Appl. Polym. Sci. 106 (2007) 2780-2790. DOI: 10.1002/app.26917

[88] P. Kazimierczak, A. Benko, K. Palka, C. Canal, D. Kolodynska, A. Przekora, Novel synthesis method combining a foaming agent with freeze-drying to obtain hybrid highly macroporous bone scaffolds, J. Mater. Sci. Technol. 43 (2020) 52-63. DOI: 10.1016/j.jmst.2020.01.006

[89] R. Ma, L. Fang, Z. Luo, L. Weng, S. Song, R. Zheng, H. Sun, H. Fu, Mechanical performance and in vivo bioactivity of functionally graded PEEK-HA biocomposite materials, J. Sol Gel Sci. Technol. 70 (2014) 339-345. DOI: 10.1007/s10971-014-3287-7

[90] R. De Silva, P. Pasbakhsh, A. Qureshi, A. Gibson, K. Goh, Stress transfer and fracture in nanostructured particulate-reinforced chitosan biopolymer composites: influence of interfacial shear stress and particle slenderness, Compos. Interfaces 21 (2014) 807-818. DOI: 10.1080/15685543.2014.960334

[91] M. Abadi, I Ghasemi, A. Khavandi, M. Shokrgozar, M. Farokhi, S. Homaeigohar, A. Eslamifar, Synthesis of nano β-TCP and the effects on the mechanical and biological properties of β-TCP/HDPE/UHMWPE nanocomposites, Polym. Compos. 31 (2010) 1745-1753. DOI: 10.1002/pc.20965

[92] G. Perumal, B. Ramasamy, A. Nandkumar, M. Doble, Influence of magnesium particles and pluronic F127 on compressive strength and cytocompatability of nanocomposite injectable and boldable beads for bone regeneration, J. Mech. Behav. Biomed. 88 (2018) 453-462. DOI: 10.1016/j.jmbbm.2018.08.002

[93] G. Converse, W. Yue, R. Roeder, Processing and tensile properties of hydroxyapatite-whisker-reinforced polyetheretherketone, Biomaterials 28 (2007) 927-935. DOI: 10.1016/j.biomaterials.2006.10.031

[94] H. Wu, D. Pang, C. Ma, Q. Li, C. Xiong, Composites of hydrosyapatite whiskers/poly(L-lactide-co-glycolide) with high tensile plasticity, J. Macromol. Sci. B 51 (2012) 1242-1255. DOI: 10.1080/00222348.2011.627824

[95] A. Teo, A. Mishra, I. Park, Y. Kim, W. Park, Y. Yoon, Polymeric biomaterials for medical implants and devices, ACS Biomater. Sci. Eng. 2 (2016) 454-472. DOI: 10.1021/acsbiomaterials.5b00429

[96] C. Wallace, C. Tsao, F. Wei, Mandibular reconstruction. In: Plastic and Reconstructive Surgery: Approaches and Techniques, John Wiley & Sons Ltd., Chichester UK, 2015.

[97] J. Jones, Chapter 9: Hierarchical Porous Scaffolds for Bone Regeneration. In: New Materials and Technologies for Healthcare, Imperial College Press,

London, 2012.

[98] P. Patil, D. Chavanke, M. Wagh, A review on ionotropic gelation method: Novel approach for controlled gastroretentive gelispheres, Int. J. Pharm. 4 (2012) 27-32.

[99] T. Giri, Alginate containing nanoarchitectonics for improved cancer therapy. In: Nanoarchitectonics for Smart Delivery and Drug Targeting, William Andrew Applied Science Publishers, Oxford, 2016.

[100] S. Pedroso-Santana, N. Fleitas-Salazar, Ionotropic gelation method in the synthesis of nanoparticles/microparticles for biomedical purposes, Polym. Int. 69 (2020) 443-447. DOI: 10.1002/pi.5970

[101] ASTM Standard E399-17, Standard test method for linear elastic plane-strain fracture toughness KIC of metallic materials, ASTM International, West Conshohocken, PA, 2017.

[102] Mechanical Finder v7.0, Research Centre of Computational Mechanics Inc., 2019

[103] SketchUp Pro 3D Modeling Software, Trimble Inc., 2020.

[104] S. Sakka, J. Bouaziz, F. Ben Ayed, Mechanical properties of biomaterials based on calcium phosphates and bioinert oxides for applications in biomedicine. In: Advances in biomaterials science and biomedical applications, IntechOpen, Rijeka, 2013.

[105] S. Laasri, M. Taha, A. Hajjaji, A. Laghzizil, E. Hlil, Mechanical properties of calcium phosphate biomaterials, Mol. Cryst. Liq. Cryst. 628 (2016) 198-203. DOI: 10.1080/15421406.2015.1137270

[106] S. Farah, D. Anderson, R. Langer, Physical and mechanical properties of PLA and their functions in widespread applications – a comprehensive review, Adv. Drug Deliv. Rev. 107 (2016) 367-392. DOI: 10.1016/j.addr.2016.06.012

[107] D. Metsger, M. Rieger, D. Foreman, Mechanical properties of sintered hydroxyapatite and tricalcium phosphate ceramic, J. Mater. Sci. Mater. Med. 10 (1999) 9-17. DOI: 10.1023/a:1008883809160

[108] S. Chung, N. Ingle, G. Montero, S. Kim, M. King, Bioresorbable elastomeric vascular tissue engineering scaffolds via melt spinning and electrospinning, Acta Biomaterialia 6 (2010) 1958-1967. DOI: 10.1016/j.actbio.2009.12.007

[109] A. Pangesty, M. Todo, Development of cylindrical microfibrous scaffold using melt-spinning method for vascular tissue engineering, Mater. Lett. 228 (2018) 334-338. DOI: 10.1016/j.matlet.2018.06.046

[110] T. Tran, Z. Hamid, N. Lai, K. Cheong, M. Todo, Development and mechanical characterization of bilayer tubular scaffolds for vascular tissue engineering applications, J. Mater. Sci. 55 (2020) 2516-2529. DOI: 10.1007/s10853-019-04159-3

[111] B. Han, P. Ma, L. Zhang, Y. Yin, K. Tao, F. Zhang, Y. Zhang, X. Li, W. Nie, β-TCP/MCPM-based premixed calcium phosphate cements, Acta Biomater. 5 (2009) 3165-3177. DOI: 10.1016/j.actbio.2009.04.024

[112] W. He, Y. Fu, M. Andersson, Morphological control of calcium phosphate nanostructures using lyotropic liquid crystals, J. Mater. Chem. B 2 (2014) 3214. DOI: 10.1039/c4tb00095a

[113] B. Saad, U. Suter, Biodegradable polymeric materials. In: Encyclopedia of Materials: Science and Technology, Elsevier Science Ltd., Pergamon USA, 2001.